Development of a method for measuring surface area concentration of ultrafine particles

Von der Fakultät für Ingenieurwissenschaften der
Universität Duisburg-Essen

zur Erlangung des akademischen Grads eines
Doktors der Ingenieurwissenschaften
genehmigte Dissertation

von

Jianming, Wei

aus

Nanjing, V. R. China

Referent:	PD Dr. -Ing. F. Einar Kruis
Korreferent:	Prof. Dr. -Ing. A. Schmidt-Ott
Tag der mündlichen Prüfung:	17. Januar 2007

Danksagung

Die vorliegende Dissertation entstand während meiner Mitarbeit im Fachgebiet Prozess- und Aerosolmesstechnik (AMT) der Universität Duisburg-Essen.

Mein persönlicher Dank gilt meinem Doktorvater Herrn PD Dr. -Ing. F. E. Kruis für sein besonderes Engagement und die Arbeit und Mühe die er für das Referat aufgebracht hat. Mein Dank gilt ebenso Herrn Prof. Dr. -Ing. A. Schmidt-Ott für die Übernahme des Korreferates.

Weiterhin danke ich Herrn Prof. H. Fissan, für die wertvollen Anregungen, die zum Gelingen dieser Arbeit geführt haben.

Den anderen Professoren der Prüfungskommission, Herrn Prof. F. J. Tegude, Herrn Prof. H. Brakelmann, danke ich für ihr Interesse und ihre Mühe.

Speziell danke ich Andreas Trampe für die täglichen wissenschaftlichen und persönlichen Gespräche. Ich danke auch Siegfried Neumann für tatkräftige Unterstützung bei den Messungen.

Weiterhin möchte ich allen meinen Kollegen und Freunden danken, die mich während meiner Promotionszeit durch ihre Hilfe und mit wertvollen Ratschlägen unterstützt haben und somit einen Beitrag zum Gelingen dieser Arbeit geleistet haben.

Zudem danke ich meiner Familie, insbesondere meiner Frau X. R. Cai, für ihr Verständnis, die damit die Anfertigung dieser Dissertation erst ermöglichte.

Contents

List of Figures

List of Tables

List of Symbols

Symbol	Dimension	Meaning
A_i	-	Cunningham fit parameters
A_{Peek}	$\mathtt{V} \cdot \mathtt{m}^{-1}$	Peek's constant
B	$\mathtt{s} \cdot \mathtt{kg}^{-1}$	particle mechanical mobility
B_{Peek}	$\mathtt{m}$	Peek's constant
C_c	-	Cunningham correction factor
$\vec{D}$	$\mathtt{m}^{-2} \cdot \mathtt{s} \cdot \mathtt{A}$	electric displacement field
D_p	$\mathtt{m}^2 \cdot \mathtt{s}^{-1}$	particle diffusion coefficient
D_{Pb}	$\mathtt{m}^2 \cdot \mathtt{s}^{-1}$	diffusion coefficient of Pb atom
$\bar{d}_a$	$\mathtt{m}$	particle arithmetic mean diameter
d_c	$\mathtt{m}$	characteristic dimension of nozzle plate
d_g	$\mathtt{m}$	particle geometric mean diameter
d_p	$\mathtt{m}$	particle diameter
E	$\mathtt{m} \cdot \mathtt{kg} \cdot \mathtt{s}^{-3} \cdot \mathtt{A}^{-1}$	local electric field strength
E_r	$\mathtt{m} \cdot \mathtt{kg} \cdot \mathtt{s}^{-3} \cdot \mathtt{A}^{-1}$	r-component of electric field strength
E_z	$\mathtt{m} \cdot \mathtt{kg} \cdot \mathtt{s}^{-3} \cdot \mathtt{A}^{-1}$	z-component of electric field strength
$\mathtt{e}$	$\mathtt{A} \cdot \mathtt{s}$	elementary electronic charge
F	$\mathtt{m} \cdot \mathtt{kg} \cdot \mathtt{s}^{-2}$	external force
F_{Br}	$\mathtt{m} \cdot \mathtt{kg} \cdot \mathtt{s}^{-2}$	Brownian force in r-axis
F_{Bz}	$\mathtt{m} \cdot \mathtt{kg} \cdot \mathtt{s}^{-2}$	Brownian force in z-axis
F_D	$\mathtt{m} \cdot \mathtt{kg} \cdot \mathtt{s}^{-2}$	Stokes drag force
F_E	$\mathtt{m} \cdot \mathtt{kg} \cdot \mathtt{s}^{-2}$	electrostatic force
g	$\mathtt{m} \cdot \mathtt{s}^{-2}$	gravitational acceleration
G_r	-	Gaussian random number for r-axis
G_z	-	Gaussian random number for z-axis
I	$\mathtt{A}$	signal current
i_c	$\mathtt{A}$	transient image current

$\bar{i}_c$	A	mean transient image current
J	$\mathrm{m}^{-2} \cdot \mathrm{s}^{-1}$	particle flux
K	$\mathrm{kg} \cdot \mathrm{m}^{-2} \cdot \mathrm{s}^{-1}$	mass transfer coefficient
K_n	-	Knudsen number
L_p	m	total particle length
l_r	m	length of central rod of ESP
m_i	kg	mass of ion
m_p	kg	mass of particle
N	m^{-3}	particle number concentration
n_p	-	particle charge number
P	Pa	actual pressure of gas in charging zone
P_0	Pa	standard pressure
p	Pa	fluid pressure
Q	$\mathrm{m}^3 \cdot \mathrm{s}^{-1}$	total flow rate
Q_a	$\mathrm{m}^3 \cdot \mathrm{s}^{-1}$	aerosol flow
Q_{ex}	$\mathrm{m}^3 \cdot \mathrm{s}^{-1}$	excess flow
Q_s	$\mathrm{m}^3 \cdot \mathrm{s}^{-1}$	sheath flow
Q_{sa}	$\mathrm{m}^3 \cdot \mathrm{s}^{-1}$	sample flow
q_i	$\mathrm{A} \cdot \mathrm{s}$	image charge
q_p	$\mathrm{A} \cdot \mathrm{s}$	particle charge
q_s	$\mathrm{A} \cdot \mathrm{s}$	saturation charge
$q^\star$	$\mathrm{A} \cdot \mathrm{s}$	charge constant
R_w	m	radius of corona needle
r_1	m	radius of the central rod of ESP
r_2	m	inner radius of the outer wall of ESP
r_{imp}	m	entrance radius of the electrical impactor
r_p	m	particle radius
S_{cont}	m^2	Fuchs surface in continuum regime
S_{fm}	m^2	Fuchs surface in free-molecule regime
S_G	m^2	Single particle surface area

S_p	$\mathtt{m}^2$	total particle surface area
S_{tr}	$\mathtt{m}^2$	Fuchs surface in transition regime
T	$\mathtt{K}$	absolute temperature
T_0	$\mathtt{K}$	standard temperature
t	$\mathtt{s}$	time
t_r	$\mathtt{s}$	traveling time in radial direction
t_a	$\mathtt{s}$	traveling time in axial direction
U	$\mathtt{m}^2 \cdot \mathtt{kg} \cdot \mathtt{s}^{-3} \cdot \mathtt{A}^{-1}$	electrode voltage
U_c	$\mathtt{m}^2 \cdot \mathtt{kg} \cdot \mathtt{s}^{-3} \cdot \mathtt{A}^{-1}$	corona voltage
U_d	$\mathtt{m}^2 \cdot \mathtt{kg} \cdot \mathtt{s}^{-3} \cdot \mathtt{A}^{-1}$	deposition voltage
U_{ip}	$\mathtt{m}^2 \cdot \mathtt{kg} \cdot \mathtt{s}^{-3} \cdot \mathtt{A}^{-1}$	voltage for ion precipitator
u_a	$\mathtt{m} \cdot \mathtt{s}^{-1}$	axial gas velocity
u_{ia}	$\mathtt{m} \cdot \mathtt{s}^{-1}$	axial ion velocity
u_{ir}	$\mathtt{m} \cdot \mathtt{s}^{-1}$	radial ion velocity
u_{pa}	$\mathtt{m} \cdot \mathtt{s}^{-1}$	axial particle velocity
u_{pr}	$\mathtt{m} \cdot \mathtt{s}^{-1}$	r-component of particle velocity
u_r	$\mathtt{m} \cdot \mathtt{s}^{-1}$	r-component of gas velocity
u_z	$\mathtt{m} \cdot \mathtt{s}^{-1}$	z-component of gas velocity
V_d	$\mathtt{m} \cdot \mathtt{s}^{-1}$	drift velocity
V_i	$\mathtt{m}^3$	specific volume
V_p	$\mathtt{m}^3$	total particle volume
V_{TE}	$\mathtt{m} \cdot \mathtt{s}^{-1}$	terminal electrostatic velocity
v_m	$\mathtt{m} \cdot \mathtt{s}^{-1}$	average velocity of gas molecules
$\bar{v}_{rms}$	$\mathtt{m} \cdot \mathtt{s}^{-1}$	ion RMS velocity
$\bar{x}$	$\mathtt{m}$	Brownian displacement
Z_i	$\mathtt{m}^2 \cdot \mathtt{V}^{-1} \cdot \mathtt{s}^{-1}$	ion mobility
Z_p	$\mathtt{m}^2 \cdot \mathtt{V}^{-1} \cdot \mathtt{s}^{-1}$	particle mobility
α_i	-	fitted parameters
β_i	-	fitted parameters
δ	-	relative density of the gas

ϵ_0	$\mathtt{m}^{-3} \cdot \mathtt{kg}^{-1} \cdot \mathtt{s}^{4} \cdot \mathtt{A}^{2}$	permittivity of free space
ϵ_r	-	particle dielectric constant
η_c	-	particle charging efficiency
η_d	-	particle depositing efficiency
η_{dc}	-	calculated depositing efficiency
η_l	-	particle loss rate
κ	$\mathtt{kg} \cdot \mathtt{m}^{2} \cdot \mathtt{s}^{-2} \cdot \mathtt{K}^{-1}$	Boltzmann's constant
λ_i	$\mathtt{m}$	mean free path of ion
λ_{Pb}	$\mathtt{m}$	mean free path of Pb atom
μ	$\mathtt{kg} \cdot \mathtt{m}^{-1} \cdot \mathtt{s}^{-1}$	gas viscosity
ρ	$\mathtt{kg} \cdot \mathtt{m}^{-3}$	fluid mass density
ρ_i	$\mathtt{s} \cdot \mathtt{A} \cdot \mathtt{m}^{-3}$	ion density
σ_g	$\mathtt{m}$	geometric standard deviation
τ_d	$\mathtt{s}$	diffusion charging time constant
τ_f	$\mathtt{s}$	field charging time constant
ξ_x	-	uniform random numbers between 0 and 1 for r-axis
ξ_y	-	uniform random numbers between 0 and 1 for z-axis
Δp	$\mathtt{Pa}$	dynamic pressure

Abbreviations

ACR:	Aerosol to Clean Air Ratio
CAG:	Combution Aerosol Generator
CFD:	Computational Fluid Dynamics.
CPC:	Condensation Particle Counter
CNC:	Condensation Nucleus Counter
CV:	Coefficient of Variation
DCE:	Diffusion Charging Electrometer
DMA:	Differential Mobility Analyzer
EAD:	Electrical Aerosol Detectors
EPI:	Epiphaniometer
ESP:	Electrostatic Precipitator
FMD:	Field Modified Diffusion model
SMPS:	Scanning Mobility Particle Sizer
SNR:	Signal-to-Noise Ratio
UCPC:	Ultra-fine Condensation Particle Counter
UDF:	User Defined Function
UFP:	Ultrafine Particle

Chapter 1

Introduction

1.1 Ultrafine particles

Aerosols are dilute suspension of microscopic particles in a gas. Small particles play a very significant role in many aspects of industrial processes and daily life, for example:

- atmospheric chemistry — Ozone destruction reactions can occur heterogeneously on the aerosol of ice crystals present in the upper atmosphere. Aerosols in the atmosphere absorb, scatter, and reflect sunlight, playing an important role in the earth's energy balance and, therefore, in global warming and climate change [47],
- materials synthesis — carbon black, fumed silica, optical fiber blanks, and many pigments are examples of materials that are commercially prepared in large quantities as aerosols,
- medicine — many drugs can be delivered effectively to the lungs, but this requires a well-designed inhaler that can disperse the drug into droplets of the size necessary to deposit the drug deep in the lungs,
- public health — the majority studies had been done in the past several

decades throughout the world have established quite firmly relationship between certain health endpoints (such as respiratory and cardiovascular diseases) and particulate pollution. These studies have shown that exposures to particulate matter could induce some acute or chronic health effects [5, 9, 16, 20, 50, 54],

- Society and economy — due to adverse impacts of PM on public health, costs for public health are increased[36, 39, 46].

In terms of the size range, aerosol particles can be roughly classified as coarse, fine, ultrafine and nanoparticles. Among them ultrafine particles (diameter less than 100nm) have several remarkable properties which distinguish them from those larger particles. First, they weigh almost nothing, so they can stay airborne for a long time and easily move from one area to another, based on small pressure differences between two spaces. Second, they have very large number per unit mass. For instance, their outside background levels of number concentration is in the range 5000-10,000 particles per cm^3, this number is even as high as 3,000,0000 particles per cm^3 during pollution episodes [53]. In addition, their indoor concentration level is also relatively high in some occasions. For instance, it is notable that vacuum cleaning has been reported to generate more than 290 particles per cm^3 [29]. Activities such as cooking also generate considerable numbers of ultrafine particles, especially in poorly ventilated environments [10]. Third, they have generally huge surface area per unit mass. For example, on very coarse powders the specific surface might be as low as a few square centimeters per gram, while on finer powders it might be a few hundreds square meters per gram.

The small size and huge surface area of ultrafine particles prompt concerns about their effects on human health. A number of toxicological studies have confirmed that ultrafine particles are able to penetrate deep into the lung where they have high deposition efficiency (50%) [2], thus they can cause more inflammation than larger respirable particles made from the same ma-

terial when delivered at the same mass dose [13, 14, 15, 34]. Although the exact biological mechanisms are not entirely clear, both mass and number of ultrafine particles have been shown to correlate with acute health effects and measurable functional changes in the cardiovascular and respiratory system [41, 42, 43]. Recent epidemiological studies have shown that adverse health effects associated to airborne particles may be better correlated with metrics such as particle number or particle surface area than particle mass [13, 31]. For example, for health risk assessment of fibrous particles such as asbestos, gravimetric measurements are no longer in use, because the importance of fibre surface area and number has been established [33, 52]. In addition, particle surface area is also of great importance in other areas. For example, specific surface area is often correlated with rates of dissolution and other rate-related phenomena such as catalyst activity, electrostatic properties of powders, light scattering, opacity, sintering properties, glazing, moisture retention and many other properties which can influence the processing and behavior of materials such as powders and porous solids. Therefore, surface area concentration measurement is very important in many applications.

1.2 Focus of this dissertation

The present dissertation was affected by the above discussions and concentrated on following aspects:

- propose a method for measuring surface area concentration of ultrafine particles (present diameter between 20nm and 100nm). This method is based on a three-step approach: particle diffusion charging, ion precipitation and charged particle deposition. The information associated with particle surface area concentration is expected to be inferred from the signal current generated the deposited charged particles.

- design and build an experimental prototype, which is consisting of a

unipolar diffusion charger, an ion precipitator and an electrical precipitator. The prototype should yield a signal which is directly proportional to the total surface area concentration of particles.

- carry out experiments to verify the proposed method for measuring the surface area concentration of ultrafine particles by means of the designed prototype. The present experiments focus on studying the several important processes, especially the particle diffusion charging process and the deposition process.

1.3 Synopsis of this dissertation

Chapter 2 introduces some concepts of particle size distribution, particle surface area concentration as well as available measurement techniques. This chapter will also include an introduction to the basic principle of our method for measuring the surface area concentration of particles.

Chapter 3 describes the theories associated with the prototype design. The relevant theories includes the particle diffusion charging theory, the ion precipitation theory and the particle deposition theory.

Chapter 4 gives a detailed description of the designing of the three main components of the prototype, which includes a corona diffusion charger, an ion precipitator and an electrical precipitator.

Chapter 5 introduces the experiments carried out to validate the prototype. The present experiments focus primarily on the measurements of particle charging efficiency, particle charge level and particle deposition efficiency. Based on the experimental results, it shows that the deposited charged particles will deliver a signal current which is proportional to their total surface area concentration.

Chapter 6 concludes the dissertation.

Chapter 2

Background

This chapter provides some background knowledge pertinent to the measurement of the particle surface area concentration. Section 2.1 presents a brief introduction to particle size distribution (PSD). Section 2.2 explains why surface area concentration is significant for ultrafine particles. Section 2.3 introduces available techniques for measuring different kinds of particle surface area concentration. Section 2.4 gives a brief introduction to the basic work principle of our prototype for measuring the particle surface area concentration.

2.1 Particle size distribution

Particle size is one of the most important properties of an aerosol. A particle group whose diameter are all nearly uniform is said to have a "monodisperse" size distribution. Conversely, a particle group whose diameter vary significantly is said to have a "polydisperse" size distribution. Most naturally occurring aerosols are polydisperse, i.e. they are composed of particles varying over a broad range of sizes. In order to adequately characterize an aerosol size distribution, a number of descriptive parameters must be used.

Measurements of the size distribution are obtained in a series of bins rep-

resenting discrete ranges of particle diameter. The resulting size distribution is commonly referred to as a size probability distribution function (or a frequency function), which is either weight- or number-based, depending on the measurement method. For number-based distribution function, n_{pi} is the number of particles in size bin $[d_i,\ d_{i+1}]$. Assuming that the average particle diameter in ith bin is d_{pi} (i.e., there are n_{p1} particles having the diameter d_{p1}, n_{p2} particles having the diameter d_{p2}, and so on) and the width of ith bin is Δd_{pi} ($\Delta d_{pi} = d_{i+1} - d_i$), the arithmetic mean diameter $\bar{d}_a$ can be calculated as:

$$\bar{d}_a = \frac{\sum_{i=1}^{M} n_{pi} d_{pi} \Delta d_{pi}}{\sum_{i=1}^{M} n_{pi} \Delta d_{pi}} = \frac{1}{N} \sum_{i=1}^{M} n_{pi} \cdot d_{pi} \tag{2.1}$$

where M is the number of bins. In above equation, $N = \sum n_{pi}$ and the second equality applies when all Δd_{pi} are the same.

The geometric mean diameter d_g of above particle distribution, in the definition of statistics, is the Nth root of the product of the N values of the diameters:

$$d_g = \left(d_{p1}^{n_{p1}} d_{p2}^{n_{p2}} \cdots d_{pM}^{n_{pM}}\right)^{\frac{1}{N}} \tag{2.2}$$

Above equation can be also expressed, in terms of the logarithms, as:

$$\ln\left(d_g\right) = \frac{1}{N} \sum_{i=1}^{M} n_{pi} \ln\left(d_{pi}\right) \tag{2.3}$$

Equation (2.3) has the analogy of equation (2.1) except now the calculation is based on the logarithm of the data. It is often used when the data are arranged logarithmically. Obviously these two types of statistics give different results because they are based on differently "scaled " information. It can

be proved that the arithmetic mean is always larger than its corresponding geometric mean for any polydisperse system [61].

With the known arithmetic and geometric mean diameter $\bar{d}_a$ and d_g, the variance (which is a measure of distribution width) can be defined as, for arithmetic and geometric, respectively:

$$\sigma^2 = \frac{\sum_{i=1}^{M} n_{pi} \left(d_{pi} - \bar{d}_a\right)^2}{N-1} \tag{2.4}$$

$$\sigma_g^2 = \exp\left[\frac{\sum_{i=1}^{M} n_{pi} \left(d_{pi} - d_g\right)^2}{N-1}\right] \tag{2.5}$$

For the convenience of later discussion, several important quantities should be introduced, i.e., total particle number, total particle length L_p, total particle surface area $S_p$and total particle volume V_p. Total particle number has been already mentioned above, and it is the only quantity that is independent upon the particle diameter:

$$N = \sum_{i=1}^{M} n_{pi} = \sum_{i=1}^{M} n_{pi} \cdot d_{pi}^0 \tag{2.6}$$

Total particle length can be estimated as:

$$L_p = \sum_{i=1}^{M} n_{pi} \cdot d_{pi}^1 \tag{2.7}$$

Total particle surface area can be calculated as:

$$S_p = \sum_{i=1}^{M} n_{pi} \cdot \pi d_{pi}^2 \tag{2.8}$$

Total particle volume can be expressed as:

$$V_p = \sum_{i=1}^{M} n_{pi} \cdot \frac{\pi}{6} d_{pi}^3 \tag{2.9}$$

In practice, it is more common to express above quantities in a certain volume. Therefore, unless otherwise indicated, N, L_p and S_p will denote the total particle number concentration, total length concentration and total surface area concentration in the rest of this dissertation.

2.2 Surface area concentration of ultrafine particles

Ultrafine particles constitute a small part of the overall particulate mass of the aerosol but present in very high numbers and contribute a significant part of the surface area concentration of the aerosol. This can be briefly illustrated by means of the following examples:

Imagine a 1 mg cube of material, which has the same density as water (1 gram per cubic centimeter). This cube would measure a 1 mm on a side (i.e. its side-length $L = 1000\mu$m). It would have a surface area of $S = 6L \times L$ or $S = 0.06\text{cm}^2$. Breaking it evenly into cubes of L would produce 1000 particles with the surface area of 0.0006cm^2 each, a total surface area of $S = 0.6\text{cm}^2$. The next such division of the length by 10 would produces 1 million $L_2 = L/10 = 10\mu$m particle with $S = 6\text{cm}^2$. The next subdivision produce 1 billion 1μm particles with total surface $S = 60\text{cm}^2$. Yet another such division would produce 1 trillion 0.1μm particles with $S = 600\text{cm}^2$. Now one can see that the 0.1μm would now have a total surface area 10,000 times that of the original 1 mg cube, without any increase in the mass.

Table 2.1 compares particle number concentration and surface area concentration for different particle sizes under the same mass concentration [35].

Table 2.1: Number and surface area concentration of particles of unit density of different sizes at a mass concentration of $10\mu g/m^3$.

Particle diameter (μm)	Number concentration (#/cm^3)	Surface area concentration (μm^2/cm^3)
0.02	2,400,000	3,016
0.1	19,100	600
0.5	153	120
1.0	19	60
2.5	1.2	24

Above Table clearly shows that particle surface area concentration could be quite different for particles of different sizes, and particle surface area concentration increases with the decreasing of particle size provided that particle mass concentration is identical. In particular, very small particles in general tend to have much larger surface area concentration as well as much higher number concentration than large particles despite the same mass concentration. These facts shows that in general very small particles tend to have very high number concentration and to make a significant contribution to particle surface area concentration. As indicated in the previous chapter, particle surface area concentration, especially the surface area concentration of ultrafine particles, are very significant in many areas and applications, it would be very important to measure it. Section 1.3 will introduce several available instruments used for measuring the particle surface area concentration.

2.3 Measurement of particle surface area concentration

This section introduces several available instruments to measure surface area concentration related properties of particles. These instruments are Scanning Mobility Particle Sizer (SMPS), Epiphaniometer (EPI) and Diffusion Charging Electrometer (DCE). Their basic work principles will be introduced in

the following sections.

2.3.1 Measuring geometric particle surface area concentration by using SMPS

The SMPS system is a commonly used tool in the aerosol particle size distribution measurements. Basically, the SMPS system consists of two different parts, namely a particle size classifier (the differential mobility analyzer (DMA)) and a condensation particle counter (CPC). The basic structure of SMPS is schematically shown in Figure 2.1.

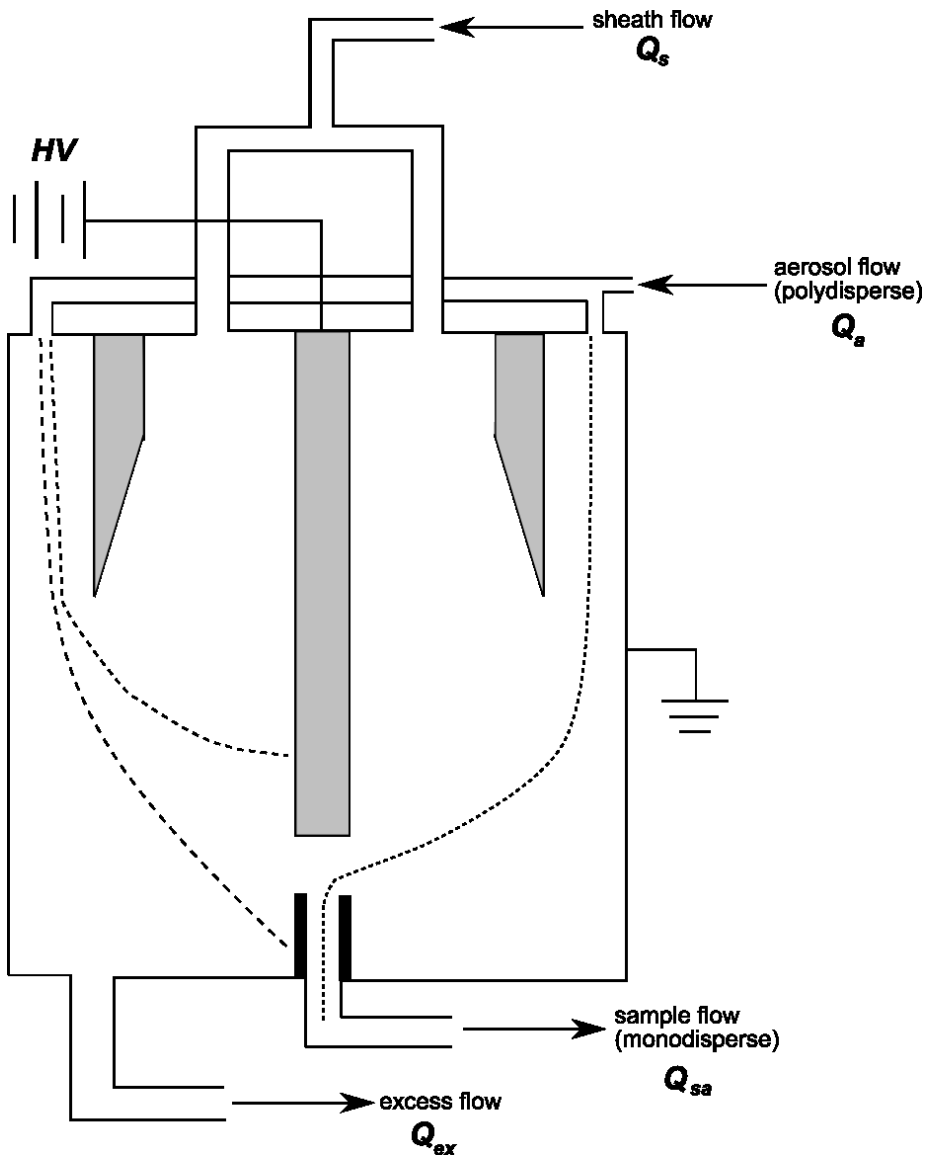

Figure 2.1: Schematic diagram of the DMA.

Before entering the DMA stage, the aerosol flow Q_a is introduced into the charger where the aerosol particles carried by the flow Q_a are charged with a predictable charge distribution. After the charging process, the flow Q_a is introduced into the laminar particle-free sheath air flow Q_s which flows

between the cylindrical electrodes. The by-pass size range of the DMA is basically adjusted by applying a voltage U between these electrodes. Due to the voltage U, the negatively charged particles drift toward the central electrode. The probability that particle is by-passed into the sample flow Q_{sa} through the slit in the central electrode depends on the voltage U and the electrical mobility of the particle. Usually particles from a quite narrow mobility range have non-zero probability to be passed through the slit.

In the secondary stage of the SMPS system a specific volume V_i from the sample flow Q_{sa} is extracted into the particle counter which then counts the number of aerosol particles in V_i. The whole mobility of interest can be measured by varying the electrode voltage U. Since the relationship between particle size and electrical mobility is known, mobilities are converted to particle diameters which are needed in the estimation of particle size distribution function. The particles that do not enter the slit are flushed out of the classifier by the excess flow Q_{ex}.

The measurement of particle surface area concentration by means of SMPS is straightforward. The particle size distribution can be obtained from the DMA and the particle number concentration is derived from the CPC. Assuming that particles are spherical, the surface area S_G of a single particle can be expressed by:

$$S_G\left(d_p\right) = \pi d_p^2 \tag{2.10}$$

where d_p is the particle diameter.

The total surface area concentration can be calculated as:

$$S_p = \sum_{i=1}^{M} S_G\left(d_{pi}\right) \cdot N\left(d_{pi}\right) \tag{2.11}$$

where M is the number of particle size bins, d_{pi} is the average particle diameter in ith size bin and $N\left(d_{pi}\right)$ is the average particle number concen-

tration in ith size bin. Clearly the total surface area concentration measured by SMPS is the general surface area concentration, which should be distinguished from another concept of surface area concentration, namely the active surface area concentration, which will be introduced in subsection 2.3.2.

2.3.2 Measuring active surface area concentration of particles by using EPI

The EPI is an instrument for measuring the active surface area concentration of particles[18, 38]. Schematic diagram 2.2 illustrates the basic structure of an EPI.

The work principle of EPI depends on measuring the attachment rate of neutral ^{211}Pb atoms onto the surface of the aerosol particles. The ^{211}Pb atoms are produced at a constant rate by the decay of a short-lived radon isotope (^{219}Rn) emanating from a long-lived artificial actinium source (^{227}Ac) that has been placed in the attachment chamber of the EPI. The ^{211}Pb atoms attached to aerosol particles are transported to a filter through a capillary. The attachment rate is determined by α-spectroscopy via the decay of attached ^{211}Pb atoms (half-life of 36.1 min.). The activity is proportional to the total number of atoms attached to the particle surface.

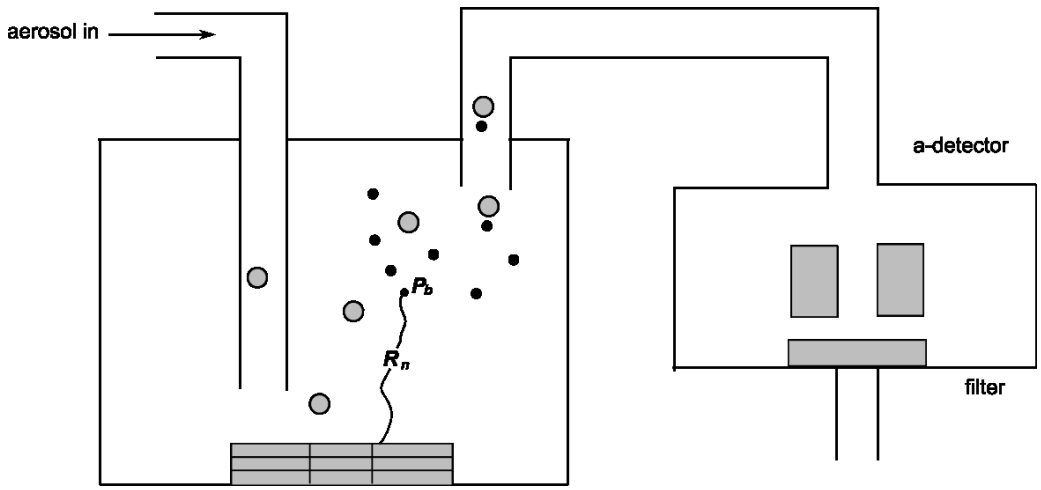

Figure 2.2: Schematic diagram of the Epiphaniometer.

The EPI was calibrated by Matter Engineering using NaCl monodisperse aerosol of 38nm, 91nm and 137nm. Calibration experiments [18, 45] have shown that the attachment coefficient of the lead atoms can be described by the Fuchs coagulation theory. According to this theory, the attachment coefficient $K(d_p)$ can be expressed by [44]:

$$K(d_p) = \frac{\pi v_{Pb} d_p^2 (\lambda_{Pb} + 0.5 d_p) D_{Pb}}{4 D_{Pb} (\lambda_{Pb} + 0.5 d_p) + 0.25 v_{Pb} d_p^2} \tag{2.12}$$

where v_{Pb} is the average velocity of Pb atoms, D_{Pb} is the diffusion coefficient of Pb atoms and λ_{Pb} is the mean free path of Pb atoms, which can be calculated by means of following expression:

$$\lambda_{Pb} = \frac{\kappa T}{\sqrt{2} \pi d_{Pb}^2 p} \tag{2.13}$$

where κ is Boltzmann's constant, T is the temperature, p is the pressure and d_{Pb} is the diameter of Pb atom.

For particles in free molecular regime, i.e., $d_p \ll \lambda_{Pb}$, equation (2.12) can be simplified as:

$$K\left(d_p\right) = \frac{\pi}{4} \cdot v_{Pb} \cdot d_p^2 \tag{2.14}$$

this expression shows that the EPI signal is proportional to the square of particle diameter.

For particles in hydrodynamic regime, i.e., $d_p \gg \lambda_{Pb}$, $K\left(d_p\right)$ can be approximated by:

$$K\left(d_p\right) = 2\pi D_{Pb} \cdot d_p \tag{2.15}$$

which indicates that EPI signal is proportional to the particle diameter.

In the intermediate (transition) regime, i.e., $d_p \approx \lambda_{Pb}$, $K\left(d_p\right)$ and d_p have the following relation:

$$K\left(d_p\right) \propto d_p^x \tag{2.16}$$

with x between 1 and 2. The power x here is a function of particle diameter, namely:

$$x\left(d_p\right) = \frac{\ln K\left(d_p\right) - \ln K\left(d_0\right)}{\ln\left(d_p\right) - \ln\left(d_0\right)} \tag{2.17}$$

where d_0 is 1μm by definition.

Actually, there are already measurement methods available for measuring the response that weight the particle number concentration N by the particle diameter d_p to the power of above x (e.g. $x = 1.5$). A more in-depth discussion on these methods and power x can be found in references [48, 49].

As can be seen, the EPI signal is closely related with the particle sizes because the attachment coefficient is strongly dependent on the particle size. The EPI does not measure the geometric surface area (although this is true for small particles) but a specific surface area of particles, called the active surface area (occasionally called Fuchs surface area), which has the following definition [18]:

$$S_{active} = \frac{2\pi d_p \lambda_{Pb} \left(A_1 + A_2\right)}{C_c} \tag{2.18}$$

with C_c the Cunningham slip correction factor [8]:

$$C_c = 1 + \frac{2\lambda_{Pb}}{d_p}\left(A_1 + A_2 \exp\left(-\frac{A_3 d_p}{2\lambda_{Pb}}\right)\right) \tag{2.19}$$

where A_1, A_2 and A_3 are Cunningham fit parameters, which are listed in Table 2.2.

Table 2.2: Cunningham fit parameters.

Parameters	Fuchs/Millikan	Hinds
A_1	1.246	1.170
A_2	0.42	0.525
A_3	0.87	0.78

Active surface area is an important particle metric. It represents the area accessible for interactions between the aerosol particles and atoms or molecules of the surrounding gas. This part of the area is active in exchanging energy and momentum from the particle to the gas. As a consequence, the active surface area has a significance in some aerosol processes such as heterogeneous chemistry or interaction with biological systems.

It is easy to see from equation (2.18) that the active surface area is closely correlated with the particle size. In terms of different particle regimes, namely the free molecular regime ($d_p \ll \lambda_{Pb}$), the continuum regime ($d_p \gg \lambda_{Pb}$) and the transition regime ($d_p \approx \lambda_{Pb}$), equation (2.18) can be in turn simplified as follows:

$$S_{fm} = \pi \cdot d_p^2 \tag{2.20}$$

$$S_{cont} = 2\pi\lambda \left(A_1 + A_2\right) d_p \tag{2.21}$$

$$S_{tr} = \frac{S_{cont}}{C_c} \tag{2.22}$$

where S_{fm}, S_{cont} and S_{tr} stand for the particle active surface in the free molecule, the continuum and the transition regime, respectively.

It can be seen from equation (2.18) and (2.12) that both the active surface are and the attachment coefficient are piece-wisely defined in terms of different size regimes. Intuitively, it is possible to establish a connection between them, thus one can estimate the active surface area of particles by means of measuring the attachment coefficient.

The major drawback of the EPI is that it is not well suited to widespread use in the workplace, because of the inclusion of a radioactive source and the lack of effective temporal resolution.

2.3.3 Measuring active surface area concentration of particles by using DCE

The diffusion charging electrometer (DCE) LQ1-DC (Matter Engineering AG) is another instrument to measure the active surface area concentration of particles. A great advantage of the DCE lies in its simplicity associated with a low price [49]. The principle of LQ1-DC is shown in schematic diagram below.

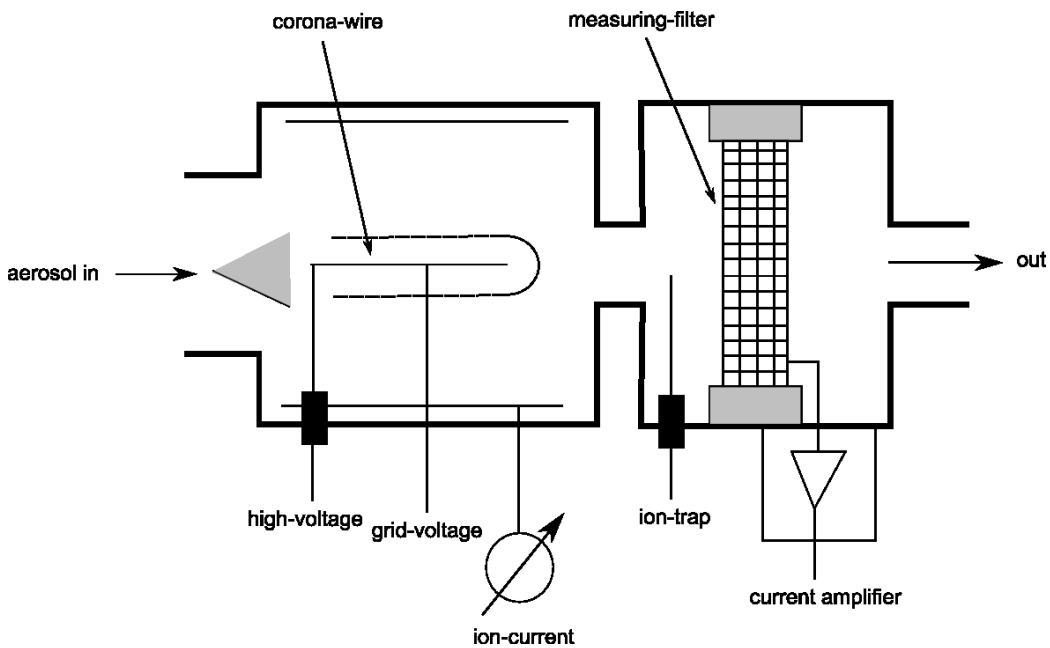

Figure 2.3: Schematic diagram of the DCE.

LQ1-DC works based on corona discharge. A corona discharge is an electrical discharge brought on by the ionization of a fluid surrounding a conductor, which occurs when the applied voltage on the conductor exceeds the corona on-set voltage. For LQ1-DC, the positive ions are produced by a corona discharge formed in the neighborhood of a thin corona-wire. Being repelled from the wire locating at positive potential, these ions then travel to the space containing the particles. Within this process, the ions have a probability of attaching to the particles, and the particle being hit would carry one or more charges. The charged particle stream then passes through a filter where the generated current flowing from the filter to the ground potential is measured by a sensitive electrometer. The current has been calibrated with particle mechanical mobility B, which can be expressed by:

$$B = \frac{C_c}{3\pi\mu d_p} \tag{2.23}$$

where μ is the gas viscosity.

It can be seen from equation (2.18) that:

$$\frac{C_c}{d_p} = \frac{2\pi\lambda\left(A_1 + A_2\right)}{S_{active}} \tag{2.24}$$

Note that the symbol of mean free path used in above equation is not λ_{Pb} but λ , which indicates that the diffusing species in the carrier gas is not necessary to be Pb atom. Substituting above equation into equation (2.23), it is readily to get:

$$B \cdot S_{active} = \frac{2\lambda\left(A_1 + A_2\right)}{3\eta} \tag{2.25}$$

This equation shows that the product of mechanical mobility and active surface area is constant. Therefore, active surface area concentration of particles can be obtained by means of above equation, once the mechanical mobility is known from its relationship calibrated with the signal current.

2.3.4 Nanoparticle surface area concentration monitor

Nanoparticle surface area monitor (TSI, Model 3550) measures the surface area concentration of particle deposited in tracheobronchial (TB) and alveolar (A) regions of the lung. The model 3550 is based on the Electrical Aerosol Detectors (TSI Model 3070A), which is an instrument designed for measuring total the particle length. The schematic diagram of EAD is shown in Figure 2.5.

As shown in the figure, an aerosol sample is drawn into the instruments continuously at a constant rate of 2.5L/min. The flow is then split, with 1l/min passing through a filter and ionizer, and the remaining 1.5l/min making up the aerosol flow. The flows are reunited in a mixing chamber where particles in the aerosol flow mix with the ions carried by the filtered clean air. The charged aerosol then passes through an ion trap to remove ex-

cess ions and moves on to a highly sensitive aerosol electrometer for charge measurement that responds to total particle length.

As shown by Wilson *et al.* [60], however, the current signal of the EAD produced after diffusion charging correlates well with the calculated amount of surface area concentration deposited in the lung.

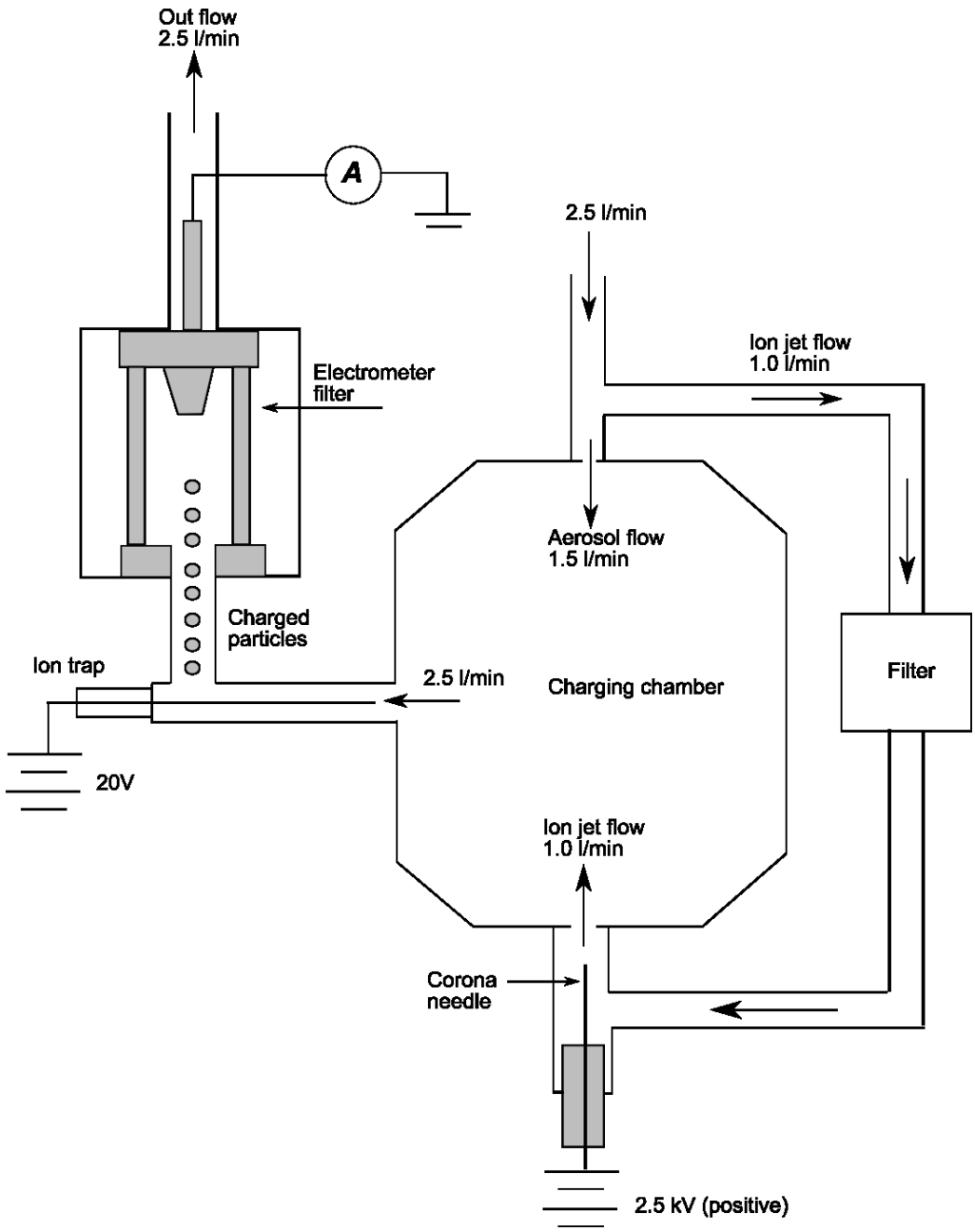

Figure 2.4: Schematic diagram of EAD.

2.4 A novel method for measuring particle surface area concentration

Based on the above discussions, this paper proposes and explores a novel method to measure the particle surface area concentration, with the basic idea being shown in Figure 2.5.

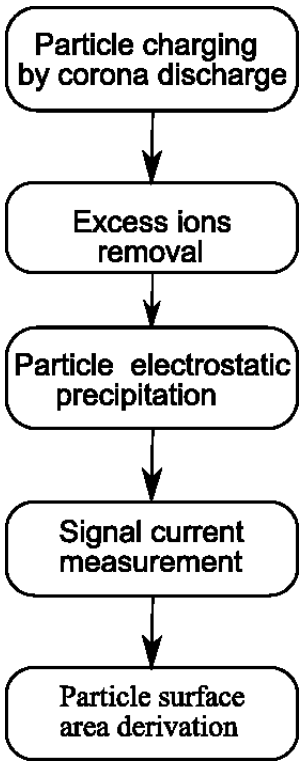

Figure 2.5: The work principle of our prototype to measure the particle surface area concentration.

Figure 2.5 shows that the following several steps are involved in measuring the particle surface area concentration. First, aerosol particles are charged through diffusion charging, which is a simple, low cost, efficient and reliable method to impose a certain charge level to particles. The excess ions mixed with the charged particles should be removed by using an ion precipitator,

otherwise they will be deposited together with the charged particles and bring adverse effects on the signal current to be measured. Then, the charged particles will be collected on a substrate within an electrical precipitator, and the current induced by the charged particles during the depositing process will be measured. Finally, the total particle surface area concentration will be inferred from the measured current. This method adopts an electrical precipitator to collect charged particles, which distinguishes it from other methods used in commercial instruments such as EAD, where a filter is used to accomplish the same task. As can be shown later (chapter 5), the great advantages of using electrical precipitator is that, once the relation between the signal current induced by the charged particles and the exponential function of particle diameter is established, the power of this function can be adjusted by changing the depositing voltage, and the particle surface area concentration can be expected by adjusting the value of the power to 2 at a specified depositing voltage; correspondingly, the total particle surface area concentration can be estimated by the signal current measured at this voltage.

In summary, the particle diffusion charging process, ion precipitating process and deposition process are three key processes in our method, and each of them should be carefully studied. Chapter 3 will give a detailed introduction to the theories associated with these processes.

Chapter 3

Theory

This chapter introduces the theories associated with the design of the prototype. The prototype consists of three main components, including a unipolar diffusion charger, an ion precipitator and an electrical precipitator, therefore, the corresponding theories associated with these components will be first introduced. This chapter is divided into following several sections: particle charging theory is introduced in section 3.1; theory on ion precipitator is described in section 3.2; theories for describing the carrier gas flow and the particle flow are given in section 3.3; theory relevant to particle deposition is presented in section 3.4; estimation of current signal, which is induced by the deposited charged particles, is discussed in section 3.5.

3.1 Diffusion charging theory

In general, particle charging can be divided into two types in terms of different charging mechanism, namely field charging and diffusion charge. As diffusion charging is relevant to the present project, theory on diffusion charging is presented in this section. For the sake of a better understanding of diffusion charging, a brief introduction on corona discharge theory is first presented in subsection 3.1.1. Next an introduction about diffusion charging theory as

well as several typical charging models are presented in subsection 3.1.2.

3.1.1 Microscopic phenomena of corona discharge

The microscopic processes involved in electrical corona are varied and complex, and lead to an array of distinct regimes of discharge behavior. The discharge behavior in a given situation depends on parameters such as the applied voltage and the resultant electric field, the molecular species present in the gas, and the number density of neutral molecules from which the ionic space charge is produced.

Fundamental models of corona based on plasma physics can be assembled from a few electron-molecule or photon-molecule interactions: impact ionization, electron attachment, two- and three-body recombination and photoionization. These interactions are impact ionization, electron attachment, two-body recombination, three-body recombination and photoionization.

$$\texttt{impactionization}: \quad \mathtt{e}^- + n \rightarrow 2\mathtt{e}^- + n^+ \tag{3.1}$$

$$\texttt{electronattachment}: \quad \mathtt{e}^- + n \rightarrow n^- \tag{3.2}$$

$$\texttt{two-bodyrecomb.}: \mathtt{e}^- + n^+ \rightarrow n + \hbar\nu \tag{3.3}$$

$$\texttt{three-bodyrecomb.}: \mathtt{e}^- + n^+ + n \rightarrow 2n + \hbar\nu \tag{3.4}$$

$$\texttt{photoionization}: \quad n + \hbar\nu \rightarrow n^+ + \mathtt{e}^- \tag{3.5}$$

where $\mathtt{e}$ is an electron, n is a neutral molecule and $\hbar\nu$ stands for a photon of frequency $f = \nu/2\pi$.

The process of ionization of a molecule in the gas occurs by electron-molecule collision leading to an "avalanche" of electrons, or by photo-ionization of the molecule by a high energy photon. In the first case, the electron avalanche begins near the wire, where the electric field is the highest, with a seed electron. This seed electron may have arisen by photo-emission of

an electron from the wire caused by a previous avalanche event, by positive ion bombardment of a cathode, by detachment of an electron from a negative ion, or by collision of a metastable molecule with the electrode releasing sufficient energy to eject an electron.

The seed electron is accelerated to a high velocity by the electric field and may undergo a collision with a neutral molecule or pre-existing ions. An electron (with kinetic energy 10eV) colliding with a neutral molecule usually interacts with the electrons orbiting the nuclei of the molecule, rather than the nuclei themselves, since the nuclei occupy a very small fraction of the molecular volume. If the incoming electron collides with electron bound to the molecule, each electron can be left with sufficient energy to escape the molecule's potential well. The net effect of the collision is to produce a positive ion and a secondary electron in addition to the ionizing electron as in equation (3.1). Both electrons are available to produce further ionizing events. In the absence of any counteracting mechanism, an electron avalanche results, and the number of electrons and ions grows exponentially in the wake of the discharge.

There are two major counteracting mechanisms that prevent the electron avalanche from growing indefinitely. One mechanism is "electron attachment", and the other is "recombination" between electron and ion. Attachment is where a free electron becomes bound to a neutral molecule to form a negative ion, and may occur by the interaction of two ("two body attachment", equation (3.3)) or three bodies ("three body attachment", equation (3.4)).

Recombination is where a free electron recombines with a pre-existing positive ion.

The interactions in time and space of these basic physical phenomena can become very complex. The complexity arises from the diverse range of charge mobilities gas properties, feedback mechanisms as suggested by

equations (3.1)-(3.5).

3.1.2 Diffusion charging

Diffusion charging is actually based on the diffusive ion flux (produced in the corona discharge) onto the surface of the particle due to the ion's random thermal motion. In diffusion charging ionic motion is driven by thermal kinetic effects. This thermal motion gives rise to diffusion of ions in directions determined by their density gradient. Thus, particles acquire charge as diffusing ions collide and attach to the particles. Under the assumption that the ionic number density is much lower than the gas number density, which implies that the ions behave the same kinetically as the gas molecules, the diffusion charging depends primarily on the thermal energy of the ions and the exposure time in the electric field.

White analyzed the charging of a dielectric particle by the diffusion charging process under the following assumptions:

1. the particle is spherical.
2. the inter-particle spacing is large compared to the particle diameter.
3. the ion concentration is invariant in the vicinity of the particle.

For a spherical particle of diameter d_p and dielectric constant ϵ_r, White produced the following formula for the charging rate [57]:

$$\frac{\mathrm{d}q_p}{\mathrm{d}t} = \frac{\pi}{4} d_p^2 \bar{v}_{rms} \rho_i \exp\left(\frac{-q_p \mathsf{e}}{2\pi\epsilon_0 d_p \kappa T}\right) \tag{3.6}$$

where q_p is the absolute amount of charges on the particle, κ is Boltzmann's constant, T the absolute temperature, ϵ_0 the permittivity of free space, e is elementary electronic charge, $\bar{v}_{rms}$ is the mean square velocity of

ion and can be calculated as:

$$\bar{v}_{rms} = \sqrt{\frac{3\kappa T}{m_i}} \tag{3.7}$$

where m_i is the ion mass. For the case of constant ion density ρ_i, integrating of equation (3.6) yields:

$$q_p(t) = q^\star \ln\left(1 + \frac{t}{\tau_d}\right) \tag{3.8}$$

where $q^\star = 2\pi\epsilon_0 d_p \kappa T/\mathsf{e}$ is known as the charge constant, and $\tau_d = 8\epsilon_0\kappa T/(d_p\bar{v}_{rms}\rho_i\mathsf{e})$ is the diffusion charging time constant [32]. Note the relation between ion number concentration n_i and ion density ρ_i, $\rho_i = n_i \cdot \mathsf{e}$, above equation can be rewritten as [22, 17]:

$$q_p(t) = \frac{2\pi\epsilon_0\kappa T}{\mathsf{e}} \ln\left(1 + \frac{d_p\bar{v}_{rms}\mathsf{e}^2}{8\epsilon_0\kappa T} \cdot n_i t\right) \tag{3.9}$$

Above equation has no theoretical limit as $t \to \infty$, but the charging rate drops exponentially with particle charge according to (3.6). The charge attained on a particle by diffusion charging is a function of the particle diameter and the ambient temperature, and is independent of the external electric field. Diffusion charging becomes the dominant charging mechanism for particles less than about 0.5μm in diameter.

Field Modified Diffusion (FMD) model

White's derivation has been criticized for neglecting the external electric field, considering only the local field due to the particle charge itself. Recently, a Field Modified Diffusion (FMD) model has been proposed ([28]). The FMD model is quite physical and practicable. This model considers both the field and diffusion charging, and it distinguishes two cases:

- Field charging is considered according to White's Field charging theory [25], while diffusion charging is assumed to be of a constant rate.

This holds approximately as long as electrical field strength E points outward and ions are accelerated toward the particle. In field charging, ions incident upon the particle surface may adhere to the surface by creating image charges within the particle volume, or may be neutralized by transferring their charge to the particle. Either way, the flux of ions transfers charge to the particle. The particle develops its own field due to the attached ionic charge. The field of the particle distorts the surrounding electrostatic field that produces the ion flux, until at the particle surface the normal component of the field completely cancels the normal component of the background field, so that no more ions are incident upon the particle. At this point the particle charge by field charging has reached a limiting value. This maximum charge obtained due to field charging is called saturation charge, denoted by q_s. q_s can be expressed by:

$$q_s = 3\pi\epsilon_0 E d_p^2 \cdot \frac{\epsilon_r}{\epsilon_r + 2} \tag{3.10}$$

where ϵ_r is the particle dielectric constant.
FMD model describes the charging rate as:

$$\frac{\mathrm{d}q_p}{\mathrm{d}t} = \frac{q_s}{4\tau_f}\left(1 - \frac{q_p}{q_s}\right)^2 + const. \tag{3.11}$$

where the second term of the right-hand side of above equation represents the contribution from diffusion charging. τ_f is the particle field charging time constant, which indicates the time taken to reach 50% of saturation charge and is expressed by:

$$\tau_f = \frac{4\epsilon_0}{\rho_i Z_i} \tag{3.12}$$

- For $q_p > q_s$, diffusion charging is the only applied mechanism. Considering the already gathered charge on the particle, FMD model writes the charging rate as:

$$\frac{\mathrm{d}q_p}{\mathrm{d}t} = \frac{1}{\tau_q} \cdot \frac{q_p - q_s}{\exp\left\{\frac{(q_p - q_s)\,\mathrm{e}}{2\pi\epsilon_0\kappa T d_p}\right\} - 1} \tag{3.13}$$

The differential equations of this model are of ordinary type, and can be solved quickly for a large amount of particles.

3.2 Ion precipitator theory

There will be some excess ions mixing with the charged particles after diffusion charging process. These ions will enter precipitator and be precipitated together with the charged particles, if they were not removed. If that is the case, they will make undesirable contributions to the signal current to be measured. To prevent this from happening, an ion precipitator is needed to separate the superfluous ions from the charged particles. In the present experiment, an electrostatic precipitator (ESP) is used to work as an ion precipitator. It is well known that ESPs are widely used for removing particles from gas streams in various industrial processes and room air-conditioning systems[58, 19]. Figure 4.2 shows the basic configuration of a typical ESP [4].

As can be seen in the Figure, at regular intervals along the middle of the flat plates (collection electrodes) are placed a series of conducting wires (discharge electrode), to which a high electrical voltage is applied. The high voltage produces an electric field and a flow of electric charges (ions) from wire to the collection electrode. Then a particulate-laden gas flow, required to be cleaned, passes through the ESP. When the ionic charge contacts a particle, the charge remains on the particle, thus the particles themselves become electrically charged over a short period of time. The charge which sticks to the particles interacts with the electric field to produce a force on the particles. This force has the same direction as the motion of the ions and will push the particles to the collection electrode. In this way the outgoing

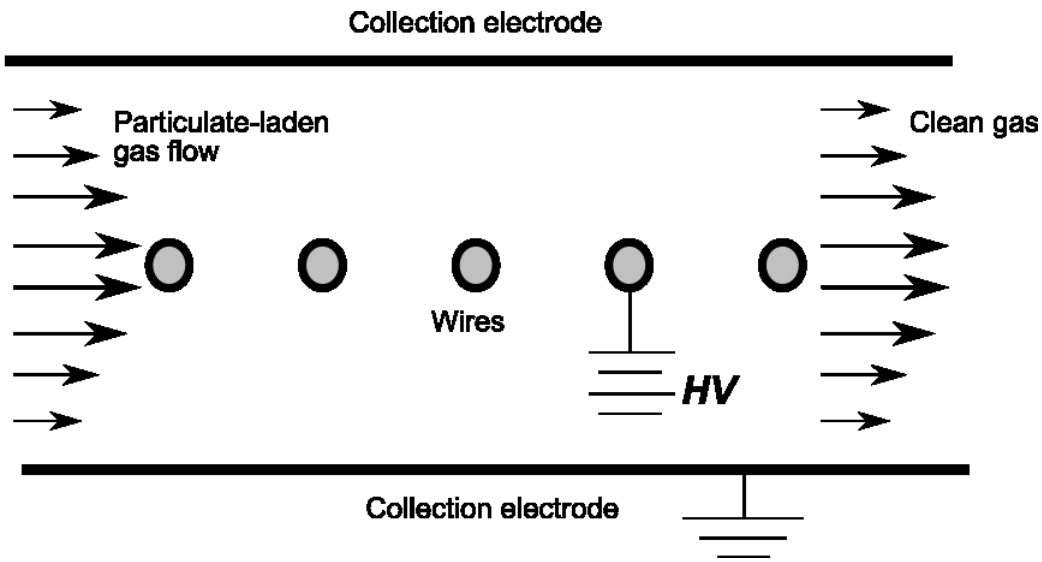

Figure 3.1: Schematic diagram of an ESP used in industry to remove particles from a gas.

gas flow would become particle-free.

Although ESPs are initially designed to precipitate particles, they are also proper for depositing ions under certain conditions. This is because ions are, just like the charged particles, carrying charges, so they can be precipitated within an electric field. The key to changing an ESP into an ion precepitator lies in applying a proper voltage to the ESP, such that only ions are precipitated while charged particles can pass through smoothly. In the present experiment, based on the following considerations, an ESP with a simple geometry is used:

- due to the fact that particles are already charged before entering the ESP, it is unnecessary to charge those particles again, thus no high voltage source is required.
- ions and charged particles have quite different electrical mobility in magnitude, electrical mobility of ions is in general much higher than

that of particles, therefore, a weak electrostatic field may be strong enough to deposit the ions.

- on the contrary, higher voltage applied to ESP will bring stronger electric field and larger electrostatic force, thus it may lead to larger particle loss, i.e. more charged particles might be precipitated. Therefore, the applied voltage has to be determined properly.

A schematic diagram of the ion precipitator is shown in Figure 3.2.

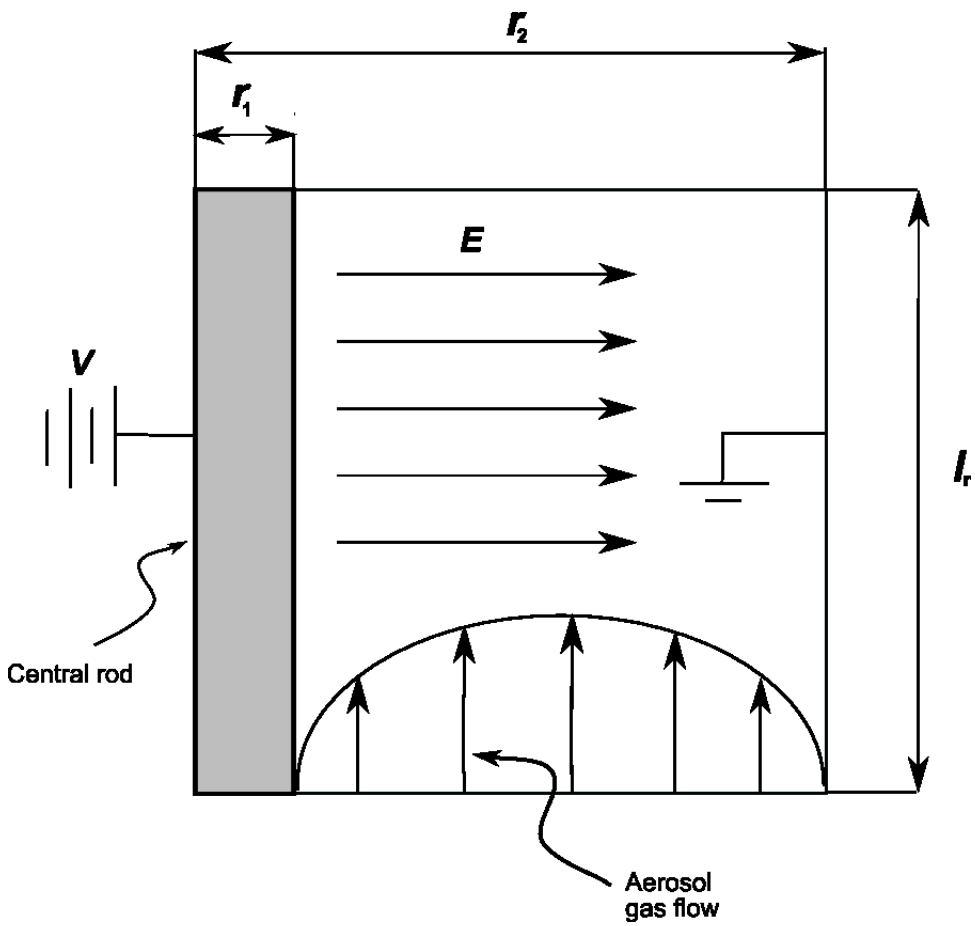

Figure 3.2: Schematic diagram of ion precipitator.

It is clear from the figure that the ion precipitator consists of two important components, namely the central rod and the outer-wall. The outer-wall is grounded, while the central rod is connected to a low voltage source by a needle with its tip touching the surface of the rod. An electrostatic field would be established in-between the central rod and the outer-wall, provided that a voltage was applied to the central rod. The radial electric field strength E_r is given by:

$$E_r = \frac{U_{ip}}{r \cdot \ln\left(\frac{r_2}{r_1}\right)} \quad r_1 \leq r \leq r_2 \tag{3.14}$$

where r is the radial location and U_{ip} is the voltage applied between the central rod and the out-wall.

As mentioned above, the most significant issue while operating the ion precipitator is the selection of a proper precipitating voltage U_{ip}. This voltage would ensure that all undesirable ions can be deposited, while most charged particles can pass through smoothly. The calculations below gives a brief instruction on the determination of the voltage U_{ip}.

First, the average flow velocity in axial direction $\bar{u}_a$ can be calculated as:

$$\bar{u}_a = \frac{Q}{\pi\left(r_2^2 - r_1^2\right)} \tag{3.15}$$

Assuming the flow velocities on the surfaces of the central rod and the outer wall are zero (i.e. $u_a(r_1) = 0$ and $u_a(r_2) = 0$), and its profile is parabolic, then the flow velocity at the inlet of the electrical precipitator can be expressed by:

$$u_a = 2\bar{u}_a \cdot \left(1 - \left(\frac{2r - r_2 - r_1}{r_2 - r_1}\right)^2\right) \quad r_1 \leq r \leq r_2 \tag{3.16}$$

The particle axial velocity u_{pa} and ion axial velocity u_{ia} are assumed to be the same as the flow velocity, i.e.:

$$u_{pa} = u_{ia} = u_a \tag{3.17}$$

On the other hand, the ion axial velocity u_{ia} and radial velocity u_{ir} can be expressed by:

$$u_{ia} = \frac{\mathtt{d}x}{\mathtt{d}t} \tag{3.18}$$

and

$$u_{ir} = \frac{\mathtt{d}r}{\mathtt{d}t} = Z_i \cdot E_r = \frac{Z_i U_{ip}}{r \ln\left(\frac{r_2}{r_1}\right)} \tag{3.19}$$

respectively. Above Z_i is the ion electrical mobility, which is a complicated function of the gas number density, electric field strength, and the constituent species of the gas [55]. The mobilities for different ions in their parent gas are different. The ions in the present work, unless otherwise indicated, are assumed to be positive ions with the electrical mobilities $1.4 \times 10^{-4}\mathtt{m}^2/\mathtt{Vs}$.

Combining equations (3.18) and (3.19) can yield:

$$\mathtt{d}x = \frac{u_{ia} \ln\left(\frac{r_2}{r_1}\right)}{Z_i U_{ip}} \cdot r\mathtt{d}r \tag{3.20}$$

Substituting the expression of u_{ia} into above equation and integrating both sides of the equation will produce:

$$x(r) = \frac{2\bar{u}_a \ln\left(\frac{r_2}{r_1}\right)}{Z_i U_{ip}} \left(\frac{\left(r^2 - r_1^2\right)}{2} - \frac{\left(r^4 - r_1^4\right) - \frac{4}{3}\left(r^3 - r_1^3\right)(r_2 + r_1) + \frac{1}{2}\left(r^2 - r_1^2\right)(r_2 + r_1)^2}{(r_2 - r_1)^2} \right) \tag{3.21}$$

If ions are completely deposited within the precipitator, then the inequality below holds:

$$x\left(r_2\right) \leq l_r \tag{3.22}$$

Furthermore, the following inequality about U_{ip} can be obtained by combining equation (3.21) and inequality (3.22):

$$U_{ip} \geq \frac{2\bar{u}_a \ln\left(\frac{r_2}{r_1}\right)}{l_r \cdot Z_i} \cdot \left(\frac{\left(r^2 - r_1^2\right)}{2} - \frac{\left(r^4 - r_1^4\right) - \frac{4}{3}\left(r^3 - r_1^3\right)\left(r_2 + r_1\right) + \frac{1}{2}\left(r^2 - r_1^2\right)\left(r_2 + r_1\right)^2}{\left(r_2 - r_1\right)^2} \right) \tag{3.23}$$

This expression shows that the lower limit of the voltage U_{ip} can be determined by flow rate Q (which influence $\bar{u}_a$) and geometry parameters (r_1, r_2, l_r) of the ion precipitator. A simply analysis shows that the minimum value of U_{ip} is attained when $r = r_2$, and it can be written as:

$$U_{ip}^{min} = \frac{2\bar{u}_a \cdot \ln\left(\frac{r_2}{r_1}\right)}{l_r \cdot Z_i} \left(\frac{\left(r_2^2 - r_1^2\right)}{2} - \frac{\left(r_2^4 - r_1^4\right) - \frac{4}{3}\left(r_2^3 - r_1^3\right)\left(r_2 + r_1\right) + \frac{1}{2}\left(r_2^2 - r_1^2\right)\left(r_2 + r_1\right)^2}{\left(r_2 - r_1\right)^2} \right) \tag{3.24}$$

Section 4.2 will present the results on the estimation of the minimum deposition voltage as well as the calculation of ion and particle trajectory based on the above conclusions.

3.3 Flow theory

In this section, the flow theories pertinent to description of the carrier gas flow as well as the interaction between particle and gas flow are presented. These theories are particularly important for understanding the behavior of particles in the electrical precipitator. This section is outlined as follows: subsection 3.3.1 presents the governing equations for describing the gas flow in the precipitator, subsection 3.3.2 introduces the general particle transport

theory and subsection 3.3.3 establishes the governing equations of particle motion within the electrical precipitator.

3.3.1 Navier-Stokes equations

The Navier-Stokes equations are used to describe the fluid motion of the flow within the depositing section. Navier-Stokes equations consist of two basic governing equations which are derived from the laws of mass conservation and momentum conservation respectively. The derivations of these equations will not be given here, as they can be found in most textbooks of fluid dynamic [3, 30, 51].

Conservation of mass

In the present study the flow was assumed to be two-dimensional, axis-symmetric and no flow in the azimuthal direction. Therefore, the conservation of mass equation for a fluid in cylindrical polar coordinates can be expressed as:

$$\frac{\partial \rho}{\partial t} + \rho \frac{\partial \left(r u_r \right)}{r \partial r} + \rho \frac{\partial \left(u_z \right)}{\partial z} = 0 \tag{3.25}$$

where ρ is the gas density, u_r is the r-component of the gas velocity, u_z is the z-component of the gas velocity. Within the electrical precipitator, the flow rate is very low (i.e., the flow has a very low Mach number) then the dynamic pressure Δp when a fluid increases its velocity from zero to $\sqrt{u_r^2 + u_z^2}$ is given by (in the absence of friction):

$$\Delta p = \frac{1}{2} \rho \left(u_r^2 + u_z^2 \right) \tag{3.26}$$

Therefore, the change of the fluid pressure can be neglected when the fluid velocity is very small, correspondingly, one can assume that the fluid has a constant density. Under these assumptions, above equation can be simplified as:

$$\frac{\partial\left(ru_r\right)}{r\partial r}+\frac{\partial\left(u_z\right)}{\partial z}=0 \tag{3.27}$$

Conservation of momentum

The conservation of momentum equations for a two-dimensional fluid in cylindrical polar coordinates are given by:

$$\rho\left[\frac{\partial u_r}{\partial t}+u_r\frac{\partial u_r}{\partial r}+u_z\frac{\partial u_r}{\partial z}\right]=-\frac{\partial p}{\partial r}+\mu\left[\frac{\partial^2 u_r}{\partial r^2}+\frac{1}{r}\frac{\partial u_r}{\partial r}-\frac{u_r}{r^2}+\frac{\partial^2 u_r}{\partial z^2}\right]+f_r \tag{3.28}$$

$$\rho\left[\frac{\partial u_z}{\partial t}+u_r\frac{\partial u_z}{\partial r}+u_z\frac{\partial u_z}{\partial z}\right]=-\frac{\partial p}{\partial z}+\mu\left[\frac{\partial^2 u_z}{\partial r^2}+\frac{1}{r}\frac{\partial u_z}{\partial r}+\frac{\partial^2 u_z}{\partial z^2}\right]+f_z \tag{3.29}$$

where p is the gas pressure, f_r and f_z are r- and z-component force acting on particle. Essentially, above equations (3.28) and (3.29) are simply expressions of Newton's second law of motion, that is, the net forces (right hand side of equations) equate with the time rate of change of momentum (left hand side of equations). The terms on the right hand of above equations could be:

- pressure gradient force,
- molecular viscous force, caused in gases by diffusion of momentum by random thermal motion,
- other momentum sources, such as gravity, electric force, etc.

Equations (3.27), coupled with equations (3.28) and (3.29), give a complete description of incompressible, isothermal Newtonian flow within the electrical precipitator.

3.3.2 Description of particle transport

The governing equations of aerosol flow in the precipitator have been introduced in the previous subsection. This subsection will continue the discussions on the relative motion of individual particles with respect to the fluid where they suspended. Understanding of the relative particle motion in the carrier gas is the key to establishing the governing equations of particle motion, which will be discussed in subsection 3.3.3.

3.3.2.1 Laminar convective transport

When an aerosol particle moves with a net velocity u_p with respect to the carrier gas in which it is suspended, the particle is subject to an aerodynamic drag force, F_D, which can be given by Stokes's law [37]:

$$F_D = 3\pi\mu u_p d_p \tag{3.30}$$

Stokes's law is a specific solution of the Navier-Stokes equations of the flow around particle, with the assumptions that inertial forces are small when compared with viscous forces, motion is constant, the particle is a rigid sphere with no walls or other particles nearby, the fluid is incompressible, and the fluid velocity is zero at the particle surface. Considering the size of particles and flow conditions in the present study, all of above assumptions are valid, except for the assumption of zero fluid velocity at the particle surface. As particle size approaches the gas mean free path, the particles begin to experience 'slip' at their surfaces (i.e. the velocity of the surrounding fluid at the particle surface is not zero). In order to account for this surface slip, Stokes's law must be modified by adding a term of Cunningham slip correction factor C_c:

$$F_D = \frac{3\pi\mu u_p d_p}{C_c} \tag{3.31}$$

The terminal setting velocity, V_{TS}, of a particle suspended in a still gas can be determined by equating the Stokes drag force to the gravitational force, i.e. $F_D = F_G$, and can be written as:

$$V_{TS} = \frac{\rho_p d_p^2 g C_c}{18\mu} \tag{3.32}$$

where ρ_p is the particle density and g is gravitational acceleration. Settling velocity is not significant for particles less than 1μm in diameter.

Finally, another useful quantity in associated with particle dynamics is the particle mobility, B, which is defined as the ratio of the particle velocity (with respect to carrier gas) to the drag force exerted on the particle:

$$B = \frac{u_p}{F_D} = \frac{C_c}{3\pi\mu d_p} \tag{3.33}$$

3.3.2.2 Electrostatically induced particle motion

Many aerosol particles carry a net electrostatic charge. In the presence of an electric field E, a charged particle will experience a net electrostatic force, F_E:

$$F_E = n_p \cdot \mathsf{e} \cdot E \tag{3.34}$$

where n_p is the net number of elementary charges on the particle.

In the absence of any other external forces, the electrostatic force will be balanced by the Stokes drag force, F_D, resulting in a terminal electrostatic velocity V_{TE}:

$$V_{TE} = \frac{n_p \mathsf{e} E C_c}{3\pi\mu d_p} = Z_p E \tag{3.35}$$

The tendency of a charged particle to move in the presence of an electric field is referred to as the electrical mobility, Z_p, which is directly related to

the particle mechanical mobility B:

$$Z_p = \frac{V_{TE}}{E} = n_p \mathsf{e} B = \frac{n_p \mathsf{e} C_c}{3\pi\mu d_p} \tag{3.36}$$

3.3.2.3 Diffusive Brownian transport

On a microscopic scale, the apparently continuous medium which we refer to as a gas is actually composed of individual gas molecules, each of which moves with a random thermal motion, constantly colliding with its surroundings. Any particle which is suspended within this gas will be involved in a number of collisions with the gas molecules surrounding it. For large particles, the number of collisions is very large, and collisions on one side of the particle are balanced by collisions on the opposite side of the particle. Consequently, the net momentum transferred from the gas molecules to the particle is negligible.

However, as the particle size becomes small compared to the mean free path of the gas, the particle may be struck by only a few gas molecules during any given period of time. As a result, the collisions on one side of the particle may not be balanced by collisions on the opposite side, and the particle will receive a net momentum transfer from the gas molecules. This change in the momentum of the particle due to collisions with gas molecules is referred to as *Brownian motion*. Although the net change in momentum for any given particle will be random, the net effect on the aerosol is to move particles from areas of high particle concentration to low particle concentration. This net motion away from areas of high concentration is known as Brownian diffusion and is described by Fick's first law of diffusion:

$$J = -D_p \cdot \frac{\mathsf{d}n}{\mathsf{d}x} \tag{3.37}$$

where J is the particles flux, $\mathsf{d}n/\mathsf{d}x$ is the particle concentration gradient, and D_p is the particle diffusion coefficient which is given by the Stokes-Einstein equation:

$$D_p = \kappa TB = \frac{\kappa TC_c}{3\pi\mu d_p} \tag{3.38}$$

Thus, as particle diameter decreases, the Brownian diffusional flux will tend to increase. For instance, according to above equation, a 100 nm particle under ambient conditions will have a mean diffusional velocity of 14 cm/sec, while a 10nm particle under the same conditions will have a mean diffusional velocity of 440 cm/sec.

Diffusion motion is a potential cause of concern in the electrical precipitator where particles are electrostatically deflected through a given trajectory. Brownian displacement introduces a random net displacement which is superimposed upon the original trajectory due to electrostatic motion. The net result of this superimposed Brownian displacement may influence the trajectory of the particle. The root mean square Brownian displacement $\bar{x}$ during a time period t is given by:

$$\bar{x} = \sqrt{2D_p t} \tag{3.39}$$

3.3.3 Particle motion within the electrical precipitator

Based on above knowledge, the governing equations of aerosol particles within the electrical precipitator can be established. The equations to describe particle motion in the deposition section can be written, by integrating the Stokes drag force, the electrostatic force, the gravity force as well as the Brownian force, as follows:

$$m_p \cdot \frac{\mathrm{d}u_{pr}}{\mathrm{d}t} = \frac{3\pi\mu d_p}{C_c} \cdot (u_r - u_{pr}) + q_p \cdot E_r + F_{Br} \tag{3.40}$$

$$m_p \cdot \frac{\mathrm{d}u_{pz}}{\mathrm{d}t} = \frac{3\pi\mu d_p}{C_c} \cdot (u_z - u_{pz}) + q_p \cdot E_z + F_{Bz} + m_p \cdot g \tag{3.41}$$

where u_{pr} and u_{pz} are particle velocities in r- and z-axis, m_p is the particle mass, E_r and E_z are components of electrical field strength in r- and z-axis,

F_{Br} and F_{Bz} are Brownian forces in r- and z-axis.

Particle mass can be expressed as the function of the diameter when the particle is assumed to be spherical:

$$m_p = \frac{\pi}{6} \cdot \rho_p \cdot d_p^3 \tag{3.42}$$

where ρ_p is the particle density.

The Brownian forces per unit mass in r and z direction at each time step Δt_b can be calculated as [1, 23]:

$$\frac{F_{Br}}{m_p} = G_r \cdot \sqrt{\frac{\pi \cdot S_0}{\Delta t_b}} \tag{3.43}$$

$$\frac{F_{Bz}}{m_p} = G_z \cdot \sqrt{\frac{\pi \cdot S_0}{\Delta t_b}} \tag{3.44}$$

with

$$S_0 = \frac{216 \cdot \mu \cdot \kappa \cdot T}{\pi^2 \cdot \rho \cdot d_p^5 \cdot \left(\frac{\rho_p}{\rho}\right)^2 \cdot C_c} \tag{3.45}$$

where G_r and G_z are zero-mean, unit variance independent Gaussian random numbers, which can be obtained by using the following transformations:

$$G_r = \sqrt{-2 \ln \xi_r} \cos 2\pi \xi_r \tag{3.46}$$

$$G_z = \sqrt{-2 \ln \xi_z} \cos 2\pi \xi_z \tag{3.47}$$

where ξ_r and ξ_z are uniform random numbers between 0 and 1.

Two electric field components E_r and E_z can be obtained by solving the Laplace equation:

$$\nabla \cdot E = 0 \tag{3.48}$$

Provided that flow field is known, the particle trajectories can be predicted by solving equations (3.40) and (3.41) numerically by using the following initial conditions for the interesting calculation domain:

- the particle initial location is set at the inlet of the electrical precipitator.
- the particle initial velocity is set equal to the local flow velocity at the same point of the inlet of the precipitator.

The new particle location and velocity after a small increment of time step Δt is calculated by numerical integration. The procedure is repeated until particles either deposit on the substrate or leave the precipitator.

It should be pointed out that above time step Δt is much longer than Δt_b in equations (3.43) and (3.44). This is because Brownian force arises as a result of the collisions of gas molecules with the particles and acts for the time corresponding to the time of contact during a collision, while the drag force acts over a much longer time scale.

The Computational Fluid Dynamics (CFD) software package FLUENT was used in the simulation. This software package allows to use a User Defined Function (UDF) [23], which allows an external C code to be compiled and linked to the flow field solver. In solving particle transport equations, the information of gas velocities u and v were required and they would be provided by the CFD solver. The external forces, including the electrostatic force and the Brownian force, can be defined in the UDF and further fed into the flow field solver to compute the particle trajectories.

3.4 Particle deposition theory

Basic theories associated with the particle deposition are presented in this section, which is outlined as follows: subsection 3.4.1 discusses the basic concept of particle deposition, subsection 3.4.2 introduces the basic definition of deposition efficiency and subsection 3.4.3 develops a model for estimating deposition efficiency.

3.4.1 Particle precipitation

Inertial impaction is one of the most widely used and thoroughly studied processes for collecting aerosol particles in different size fractions. Figure 3.3 is the schematic diagram of an inertial precipitator.

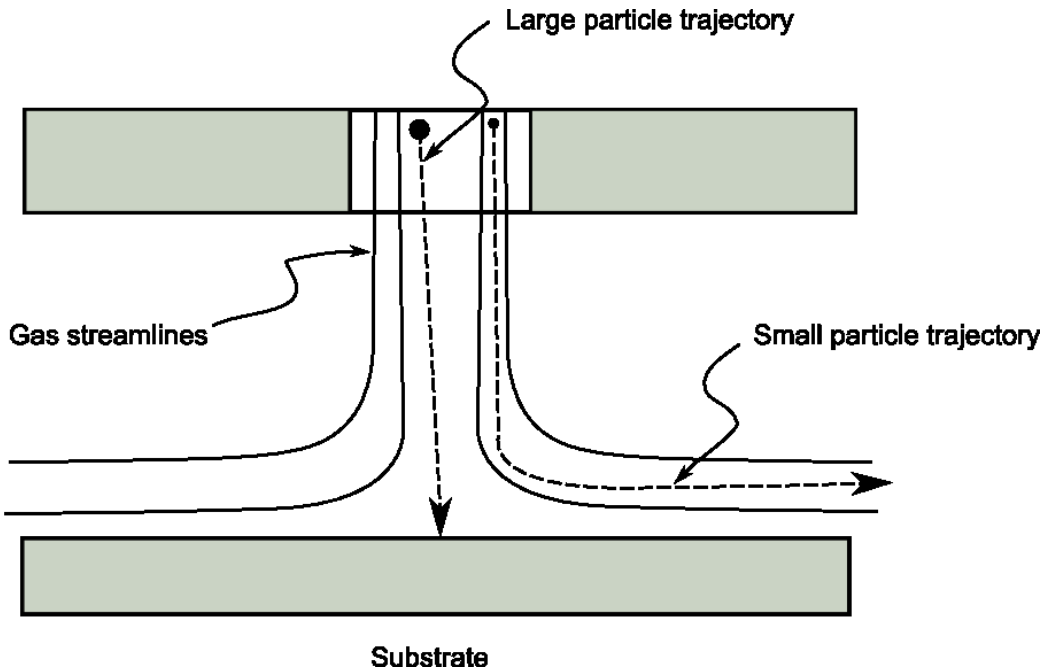

Figure 3.3: Schematic diagram of an inertial precipitator.

The basic process of inertial impaction can be described below. A jet of

aerosol is directed from a nozzle orifice onto a flat plate. When the aerosol flow is approaching the flat plate, the streamlines of the gas flow will turn sharply from being perpendicular to the plate to being parallel to it. Due to their greater momentum, however, aerosol particles will not be able to change their traveling direction as quickly as the gas. If the particle momentum is sufficiently high, particle then will be unable to follow the path of the gas flow, instead it will run across the flow streamlines and finally impact on the substrate.

Unfortunately, it is impossible to use inertial impaction directly to deposit very small particles (e.g. ultrafine particles) under normal conditions due to the fact that small particles are unable to overcome the Stokes drag force exerted by the surrounding carrier gas. In general small particles will follow the streamlines of surrounding carrier gas very well and escape from the inertial impactor. In this case, therefore, the external forces are needed to overcome the Stokes drag force in order to deposit the small particles. In the present study, the electric force is used . In particular, an electrostatic field has to be introduced within the deposition zone. Figure 3.4 schematically shows the precipitator with the presence of an electrostatic field.

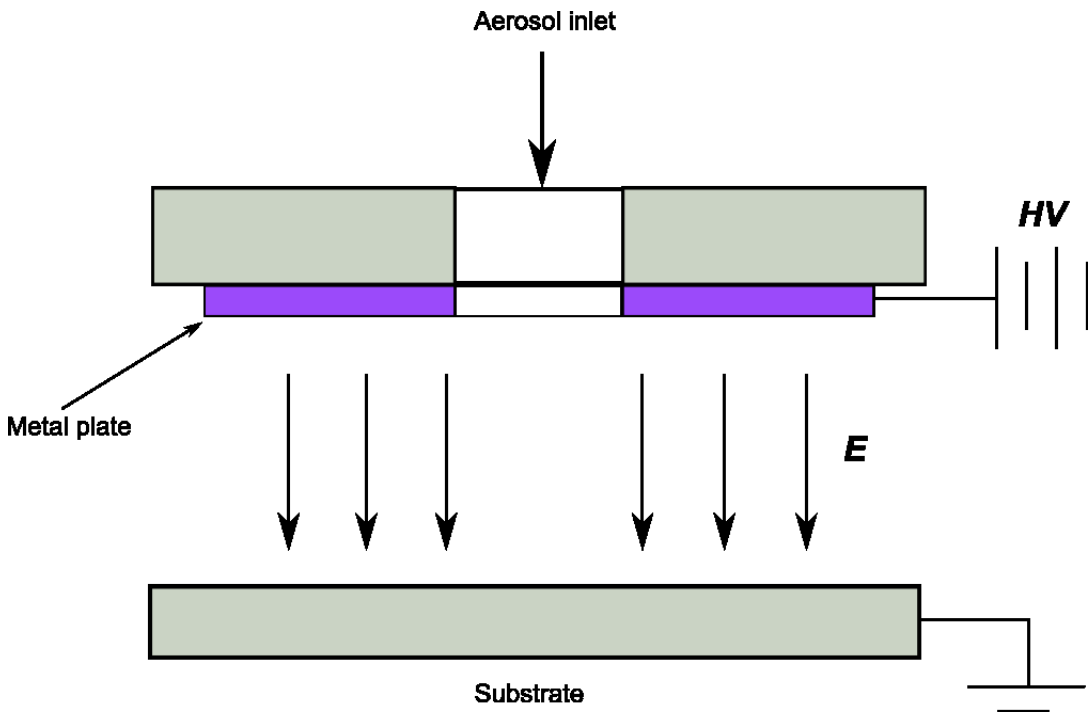

Figure 3.4: Schematic diagram of an electrical precipitator

3.4.2 Estimation of deposition efficiency from experiment

The particle deposition efficiency can be defined as:

$$\eta_d = \frac{\texttt{particles collected on the substrate}}{\texttt{particles entering the impactor}} \tag{3.49}$$

which means that particle deposition efficiency can be calculated as the ratio of the number of particles being deposited to the total number of particles entering the electrical precipitator. In practice, particle numbers can be represented by its number concentration, which can be read from an UCPC, thus particle deposition efficiency can be quickly estimated from experiments by using equation (3.49).

3.4.3 Estimation of the particle deposition efficiency

Based on CFD simulation, a numerical model has been developed to estimate the particle deposition efficiencies. This model uses following assumptions:

- particles are spherical.
- velocities of flow and particle are identical for the same locations of the precipitator inlet, i.e., $u_p(r) = u(r)$.
- velocity profile of flow at inlet is parabolic, i.e.:

$$u(r) = C\left(1 - \left(\frac{r}{r_0}\right)^2\right) \tag{3.50}$$

  where r_0 is the radius of precipitator inlet, r is the particle location measured from the center-axis, C is a constant associated with the particle average velocity.
- particles are spatially uniform distributed.
- particles will stick to the substrate once they touch it (no rebound).

It should be pointed out that the numbers of particles while passing through an arbitrary location r at one moment could be different under above assumptions despite of their uniform number concentration in space. This lie in the assumption that particle velocity profile is parabolic, implying that particle velocity at different locations is different. As a matter of fact, the numbers N of particles while passing through the precipitator through location r to $r + \mathtt{d}r$ in unit time can be estimated by:

$$\mathtt{d}N = C \cdot u(r) \cdot 2\pi r \mathtt{d}r \tag{3.51}$$

where C is a constant associated with particle number concentration.

Combining equation (3.50) and (3.51), it is easy to calculate the particle numbers $N(r_1, r_2)$ in-between location r_1 and r_2:

$$\frac{N(r_1, r_2)}{N_0} = \left(2\left(\frac{r_2}{r_0}\right)^2 - \left(\frac{r_2}{r_0}\right)^4\right) - \left(2\left(\frac{r_1}{r_0}\right)^2 - \left(\frac{r_1}{r_0}\right)^4\right) \tag{3.52}$$

where N_0 is total particle numbers emitting from the precipitator inlet, and r_1 and r_2 satisfy $0 \leq r_1 \leq r_2 \leq r_0$.

For the sake of convenience of later discussion, the distance between location r_1 and r_2 is named a size ring. In the present simulation, the radius of precipitator inlet r_0 ($r_0 = 1$ mm) is divided into ten equal-spaced size rings. At the beginning of each simulation, 1000 (i.e., $N_0 = 1000$) particles were emitting from the precipitator inlet. The distribution of particles in different size rings was determined by expression (3.52) and listed in Table 3.1. The trajectories of those particles within the precipitator were tracked and the actual numbers of particles deposited were counted. In order to increase the calculation accuracy, calculation will iterate for five times for each specific particle size and deposition voltage. The average values of five calculations will be taken as the result of deposition efficiency. By counting the numbers of deposited particles and denoting their numbers as N_{ij} (subscripts i denotes ith simulation, and j indicates jth size ring), the deposition efficiency can be expressed as follows:

$$\eta_d = \frac{\sum_{i=1}^{5}\sum_{j=1}^{10} N_{ij}}{\sum_{i=1}^{5} N_0} \times 100\% \tag{3.53}$$

For the sake of comparison, the parameters used in the simulation are chosen in agreement with that of used in the experiments. Those parameters

include the deposition voltage, the flow rate as well as the particle carried charges. In the present simulation, deposition voltages range from $1kV$ to $4kV$; aerosol flow rate is 1l/min; the actual particle charge levels (obtained from the experiments) are utilized. Chapter 5 presents the comparison between the deposition efficiencies calculated based on this model and estimated from the experiments.

Table 3.1: Particle number distribution in different size rings.

No. of size ring	Interval (mm)	Particle numbers
1	0.0–0.1	19
2	0.1–0.2	59
3	0.2–0.3	94
4	0.3–0.4	123
5	0.4–0.5	143
6	0.5–0.6	153
7	0.6–0.7	150
8	0.7–0.8	130
9	0.8–0.9	93
10	0.9–1.0	36

3.5 Induced signal current

As mentioned in section 2.4, the induced signal current will be measured for the purpose of obtaining particle surface area concentration. This signal current is strongly related to the previous processes, including the particle charging and deposition process. In particular, the following characteristic parameters of those processes are associated with the signal current:

- particle charging efficiency η_c,
- mean charge level of particle n_p, $n_p = q_p/\mathsf{e}$,
- particle deposition efficiency η_d.

The charging efficiency η_c indicates the percentage of total particles that obtain at least one electron. The mean charge level n_p represents the average number of electrons on a particle. The deposition efficiency η_d indicates the fraction of charged particles deposited out of the total particles. Noticing the physical meaning of the current, it is not difficult to express the signal current induced by the deposited monodisperse aerosol particles as the function of above parameters, i.e.:

$$I\left(d_p\right) = N_0 \cdot \eta_c\left(d_p\right) \cdot n_p\left(d_p\right) \cdot \eta_d\left(d_p\right) \cdot \mathsf{e} \cdot Q \tag{3.54}$$

where N_0 is the total particle number concentration, e is the fundamental charge on an electron, Q is the total flow rate.

In the case of polydisperse aerosol, the signal current equation (3.54) has to be rewritten as:

$$I\left(d_p\right) = \sum_{i=1}^{M} \eta_c\left(d_{pi}\right) \cdot n_p\left(d_{pi}\right) \cdot \eta_d\left(d_{pi}\right) \cdot \mathsf{e} \cdot Q \cdot N_{pi} \cdot \Delta d_{pi} \tag{3.55}$$

where M is the number of particle size bins, d_{pi} is the average particle diameter in ith bin, Δd_{pi} is the width of ith size bin and N_{pi} is the average particle number concentration in ith size bin.

The particle charging efficiency η_c, particle mean charge n_p and particle deposition efficiency η_d in above equations are all functions of particle diameter d_p. If those functions are available, i.e. their relations with particle diameter d_p are known, it is quite easy to establish a correlation between the current I and the particle diameter d_p. Furthermore, the relationship between the current I and the particle surface area concentration can be obtained as the surface area is proportional to the square of particle diameter d_p. Unfortunately, on the one hand, there lacks of sophisticated theoretical model to estimate the particle charging efficiency; on the other hand, the available

charging mode might not predict the mean charge levels accurately due to the fact that the ion concentration distribution was difficult to be measured accurately. In this situation, experiments have to be carried out. Chapter 5 will present the detailed introduction and analysis of the experiments.

Chapter 4

Prototype design

Chapter 4 presents a detailed introduction to the design of the prototype with the following outline. Section 4.1 describes the design of the unipolar diffusion charger. Section 4.2 gives an introduction to the design of the ion precipitator. Section 4.3 focuses on the design of the electrical precipitator. Section 4.4 introduces the signal current measurement.

4.1 Corona diffusion charger

The basic work principle behind the corona diffusion charger is that the incoming aerosol flow collides with ions within a closed and electric field-free zone. During the collision process, some ions would hit on the particle surface and further deposit there. On a macroscopic scale, it is concluded that particles have been charged. The main goal while designing such a unipolar diffusion charger is to ensure that it has relatively high charging efficiency.

4.1.1 Requirements

The basic requirement of the design of corona diffusion charger is that it should be efficient in charging the incoming aerosol particles. This efficient can be measured by two critical factors. The first factor lies in the actual charge level generated on each particles, while the second one in the net percentage of charged particles which are actually charged. Both charge level and net percentage would have direct impacts on the signal current induced by the deposited charged particles later. Clearly, low charge level or small percentage would lead to low current, which is not easy to be measured accurately. Correspondingly, it is necessary to collect a large number of particles in order to produce a reasonable current signal and this is not realistic under present laboratory conditions. Another critical consideration for the charging section is that whatever the produced charge distribution is, it must be highly predictable and consistent. In other words, it is expected that all charged particles of a given size should have the identical charge level in order to minimize the influence on the signal current to be measured.

4.1.2 Design description

The schematic diagram of the corona diffusion charger is shown in Figure 4.1.

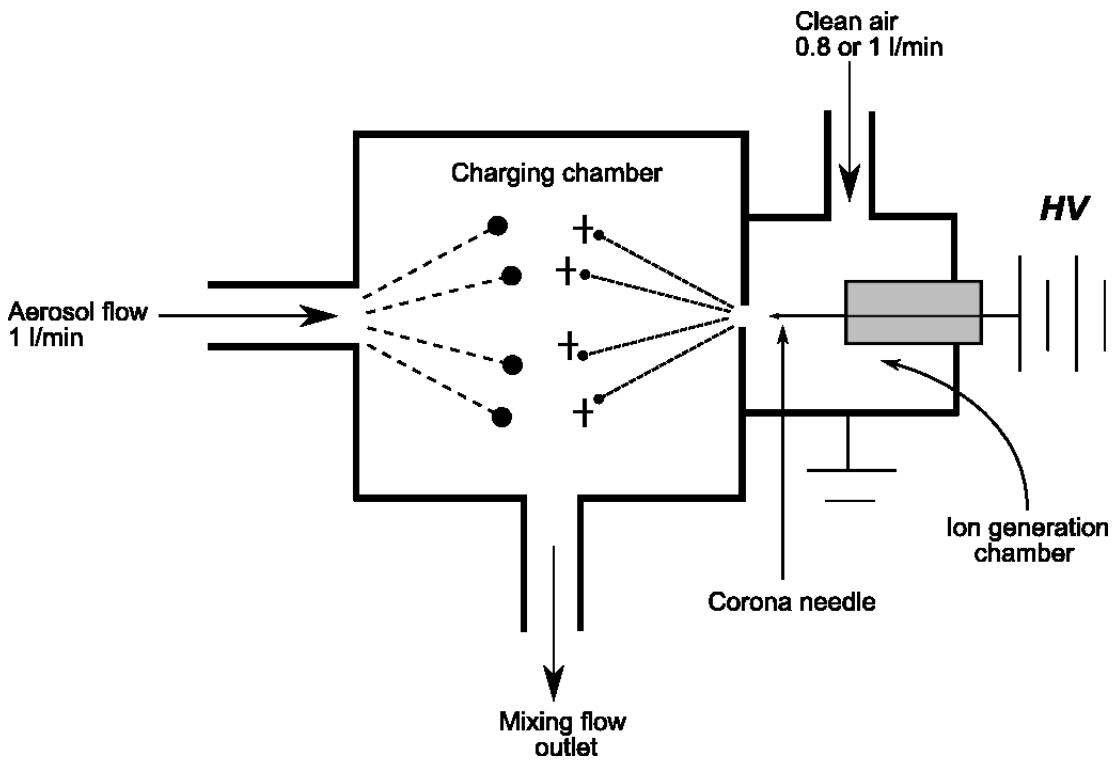

Figure 4.1: Schematic diagram of the corona diffusion charger.

It can be seen in the Figure that the diffusion charger consists primarily of two parts, namely a charging chamber and ion-generation chamber. The charging chamber has a cube space with dimension 3(cm)×2(cm)×2(cm), where the aerosol flow is mixing with ion flow. The ion-generation chamber is adjacent to charging chamber. A thin tungsten wire (25μm in diameter) is mounted on one end of the chamber to serve as the corona needle (*positive electrode*), so the wire is further connected to a high voltage source. Both charging and ion-generation chamber have the outer-walls made of non-conductive material Delrin. Additionally, the outer-wall of ion-generation chamber is grounded and can be viewed as negative electrode. The generated ion will be transported into the charging chamber through the orifice on the chamber wall by using clean air flow.

It should be pointed out that the usage of a very thin wire will ensure corona onset is occurring at a relatively low voltage. According to Peek's equation [40], the electrode surface electric field at which corona onset occurs in air for smooth, cylindrical electrodes can be described by:

$$E_{Peek} = A_{Peek} \cdot \delta \cdot \left(1 + \frac{B_{Peek}}{\sqrt{\delta \cdot R_w}}\right) \tag{4.1}$$

with

$$\delta = \frac{T_0}{T} \cdot \frac{p}{p_0} \tag{4.2}$$

where coefficient A_{Peek} is $30.1kV/\text{cm}$, B_{Peek} is 0.0301m, R_w is wire radius in meters, T_0 is standard temperature, p_0 is standard pressure. δ is the relative density of the gas compared to standard temperature and pressure (STP). It's easy to see from Peek's equation that lower corona onset voltage can be obtained by using a thinner corona wire (i.e. with smaller value of R_w).

4.2 Ion precipitator

4.2.1 Requirements

Particle flow should firstly pass through an ion precipitator before entering the electrical precipitator, otherwise these ions would be deposited together with the charged particles and contaminate the signal current to be measured. In this situation, an ion precipitator is needed to remove the excess ions which are mixing with charged particles.

4.2.2 Design description

Unlike the unipolar diffusion charger and the electrical precipitator, the ion precipitator used in the present experiment is not self-designed, but an avail-

able ESP. The cross section view of this ion precipitator (ESP) is shown in Figure 4.2.

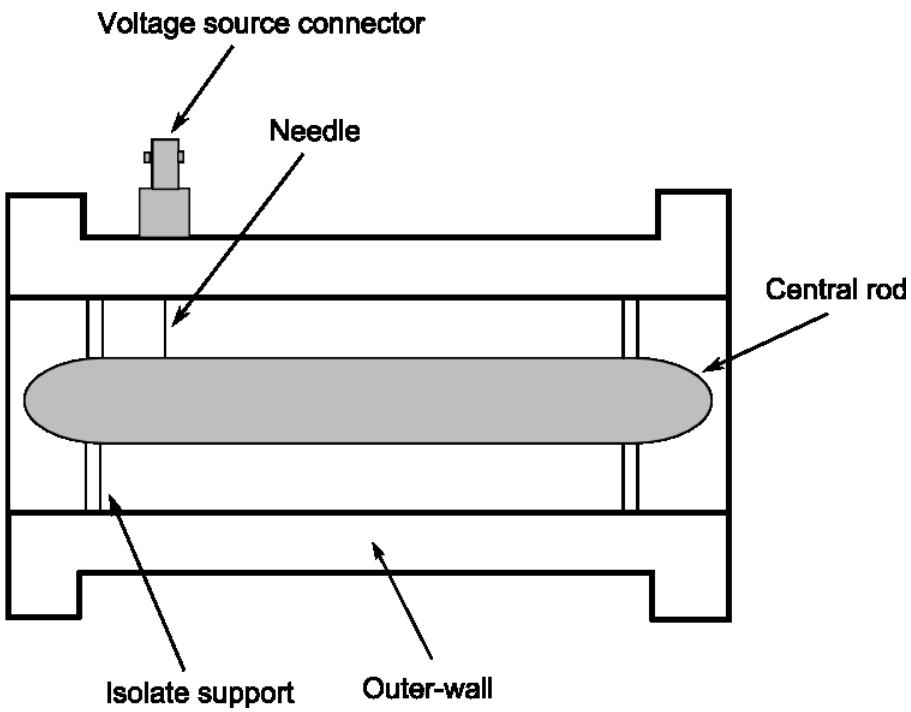

Figure 4.2: Schematic diagram of an ion precipitator.

As can be seen in the figure, the precipitator consists mainly of a central rod and outer-wall. The central rod is connected to a low-voltage source by a needle with its tip just touching the surface of the rod. The length of the central rod l_r is about 80mm, the radius of the central rod r_1 and inner radius of the outer-wall r_2 are 9.4mm and 17.2mm, respectively. The most important issue while operating the ion precipitator is setting a proper voltage to deposit the ions. This voltage will ensure that all ions can be removed but most charged particles are not influenced. Based on the theory described in section 3.2, the minimum voltages for ion precipitation under different flow rates are calculated and listed in Table 4.1. It can be seen from the Table that the required precipitating voltages are quite low.

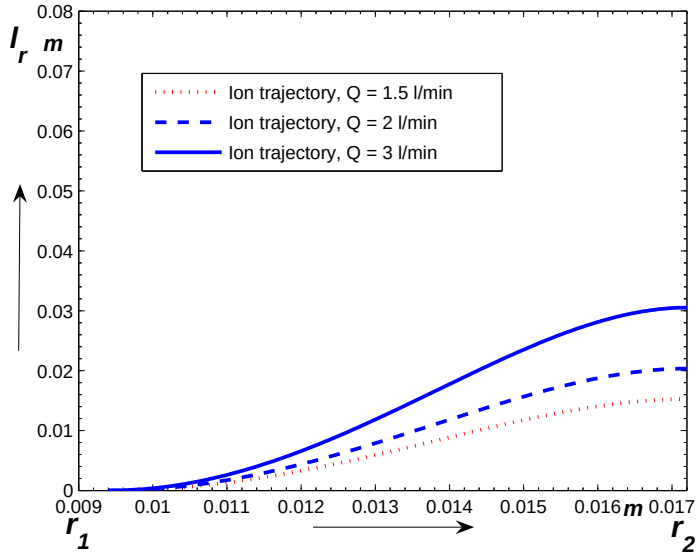

Figure 4.3: Ion trajectories starting at the central rod within the ion precipitator at U_{ip} =1.5V.

Table 4.1: Minimum precipitating voltages U_{ip}^{min} at different flow rates.

Q(l/min)	U_{ip}^{min}(V)
1.5	0.28
2	0.38
3	0.57

Figure 4.3 shows the ions trajectories within the ion precipitator at different flow Q and fixed deposition voltage U_{ip} 1.5V, which is a little bit higher than those calculated voltages U_{ip}^{min} listed in Table 4.1. It is clear from the Figure that all ions can be deposited under this voltage.

Finally, it is still necessary to prove that the chosen voltage has barely minimum influence on the charged particles. This can be easily done by calculating particle's trajectories within the ion precipitator at the identical voltage U_{ip} . In the calculation, particle's governing equations are identical to ion's governing equations (3.18) and (3.19) with the only exception of the

ion's electrical mobility Z_i in equation (3.19), which should be replaced by particle electrical mobility Z_p. Z_p can be calculated as:

$$Z_p = \frac{q_p C_c}{3\pi\mu d_p} \tag{4.3}$$

Considering an extreme case in which a particle with 20nm in diameter (the lower limit of particle size in this study) is singly charged, thus the particle tends to have the largest electrical mobility. In addition, the flow rate Q is 1.5 l/min, and U_{ip} is 1.5 V. Figure 4.4 plots the particle trajectories within the ion precipitator, starting from different initial locations (A, B, $\cdots$, G).

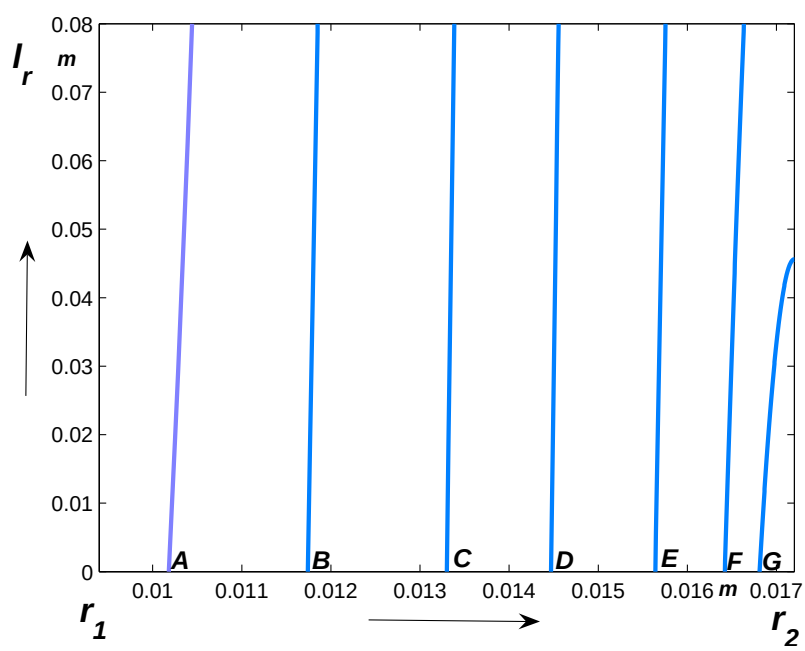

Figure 4.4: Particle trajectories within the ion precipitator.

It is easy to see that most of the particles can safely pass through the ion precipitator even at the remote location position F (the distance between

r_1 and F being 90% of that between r_1 and r_2). This indicates that most particles can pass through the ion precipitator smoothly.

4.3 Electrical precipitator

The electrical precipitator plays the role of separating the charged particles from the carrier gas and depositing them on a substrate. The separation and deposition of particles are accomplished by passing them through an electrostatic field within the electrical precipitator. This section presents a detailed description of the functional requirements and the design of the electrical precipitator.

4.3.1 Requirements

The most important functional requirements on precipitator is to collect the charged particles ranging from 20nm to 100nm. Due to their small sizes, particles falling into this interval generally tend to follow the streamlines of the carrier gas very well under the influence of Stokes drag force. Therefore, some other forces will be required to overcome the drag force in order to deposit the charged particles. In the present study, the electrostatic force has been used base on the following considerations:

- the particles entering the electrical precipitator are already charged, i.e. they carry certain amount of charges, thus they would experience electrostatic forces within the electric field in the precipitator,
- it is quite easy to establish an electrostatic field, and the simplest case is only requiring two parallel metal plates and a voltage source. In addition, the magnitude of the field strength can be easily managed by either adjusting the applied voltage or altering the distance between the two plates.

As particle deposition is accomplished through transverse transport of the particles induced by electrostatic force, it is essential that no other forces significantly affect this transverse transport of the particles. Given the size range of particles to be deposited, two modes of transport have the potential to affect transverse transport: diffusion and convection. Diffusion acts randomly to move the particles in all directions, thus may change the particle trajectories randomly. The effects of diffusion are inevitable and unavoidable, but can be minimized by limiting the amount of time which particles reside in the precipitator. Convective transport of particles is a much greater cause for concern, as any such convective motion would quite likely overwhelm the effects of the expected electrostatic transport. Therefore it is critical that the aerosol flow in the precipitator is uniform and laminar.

4.3.2 Design description

A simplified schematic diagram of the electrical precipitator is shown in Figure 4.3.2.

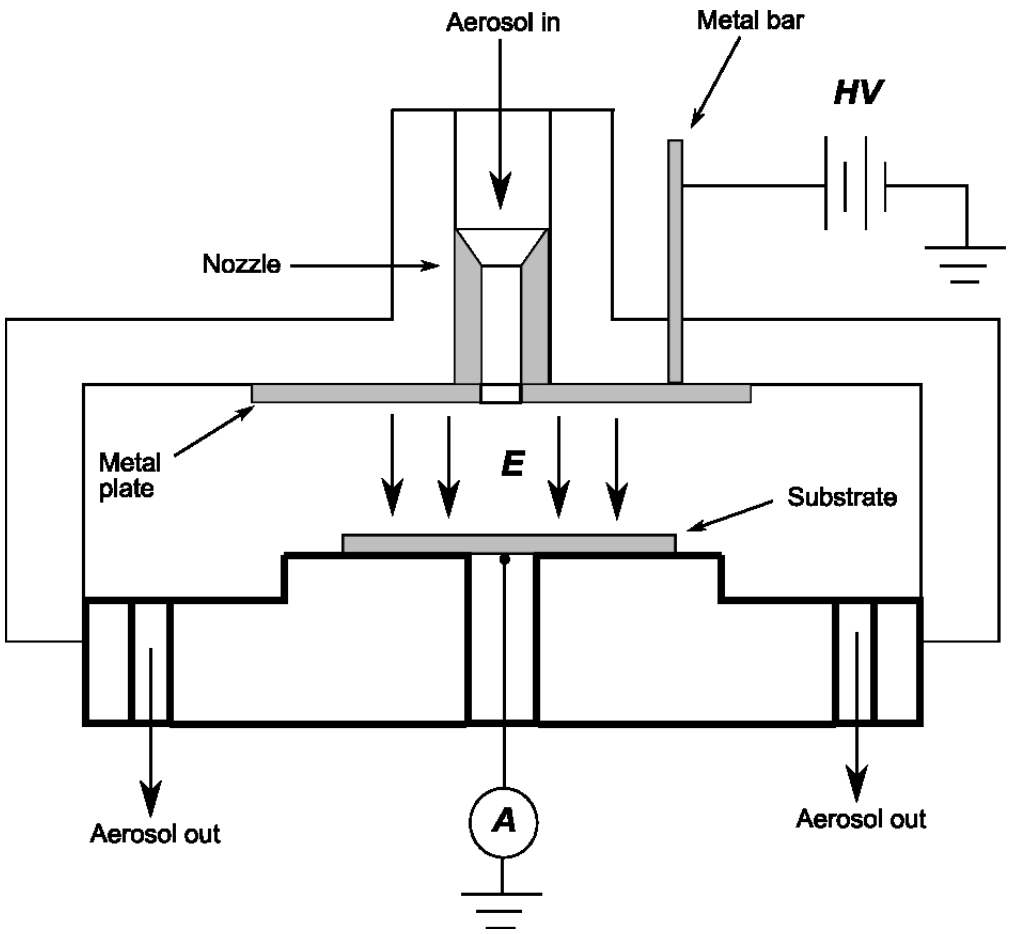

Figure 4.5: Schematic diagram of the electrical precipitator.

The main section of the electrical precipitator is the deposition zone, which actually locates in between the upper metal plate and the bottom metal substrate (8mm in diameter). The distance between metal plate and substrate is about 8mm. The metal plate is connected to a high voltage source by means of a metal bar, while the the substrate is connected to a highly sensitive electrometer. Once a voltage is applied to the metal plate, an electrostatic field will be established within the deposition zone. When charged particles enter this zone, they would experience the electrical force; and when the force exerted upon the particle is large sufficiently, it is able to

overcome the Stokes drag force and drive the particle to deposit on the substrate. The deposited particles will further transfer the carried charges to the substrate, thus the electric current will be generated during the deposition process. The induced current is further measured by a sensitive electrometer. Finally, those un-deposited particles will leave the electrical precipitator through the outlets (marked "aerosol out" in the figure).

Delrin has been used for most components of the precipitator (except the metal plate, bar and substrate) due to its good mechanical strength, hardness and dimensional stability as well as good electrical insulation properties.

4.4 Current signal measurement

Charged particles depositing on the substrate lead to an electrical current. In general, it is not easy to measure this current signal due to two facts: (1) the current is very low, and (2) the influence of the transient induced current. This section focuses on the signal measurement, including the introduction to the device used in the measurement and the analysis of the transient induced current.

4.4.1 Instrument for measuring the signal current

Before determining the measurement device, it is necessary to estimate the approximate magnitude of the signal current to be measured, and this can be accomplished by means of equation (3.54). According to this equation, the signal current is proportional to particle number concentration. As a simple estimation, equation (3.54) suggests that current will reach about 26 femtoamperes under the assumptions that particles are single charged, their number concentration is 10,000/$\mathtt{cm}^3$ and the flow rate is 1l/min. This is certainly rather low current, but it still can be measured by using some high sensitive electrometers.

In the present study, a commercial electrometer Keithley 642 was used to measure the current. Keithley 642 is an electrometer for sensitive measurement of current, voltage, or charge [24]. The device has a measurement range 10aA – 200nA with typical less than 1mV voltage burden. Clearly the measurement range of this electrometer covers the current signal to be measured. Unfortunately, the measurement is influenced by another factor named the transient image current, which will be discussed below.

4.4.2 Transient induced signal currents

The presence of charged particles within an electrical field causes a disturbance in the form of the field. The effect of charged particles in electric fields can be studied by using the images method. In particular, the effect of a charged particle q at a distance z above the surface of a conductor induces an image charge $-q_i$ at a distance below the surface of the conductor. As the charged particle q_i moves with respect to the surface of the conductor, the image charge moves in mirror image. As a sequence, the motion of q_i induces an image current i within the conductor even before the charge reaches the conductor surface.

Under steady or quasi-steady state conditions, where the flux of charged particles onto the conductor surface is constant and continuous, net induced current will be zero. However, in the case of a rapid change in particle flux the induced current may have remarkable impacts upon the measurement results. The analysis below is presented with respect to a single charge q approaching a conducting surface, analogous to a single charged particle approaching the surface of an electrode within the precipitator.

Figure 4.6 shows two flat parallel plates which are separated by a distance h. The charge q is at a location z above the collecting electrode and x from the axial center-line of the electrode. Both the length (x-axis) and width (y-axis) of the collecting electrode are l. Gauss's law gives the charge on a conducting surface A as:

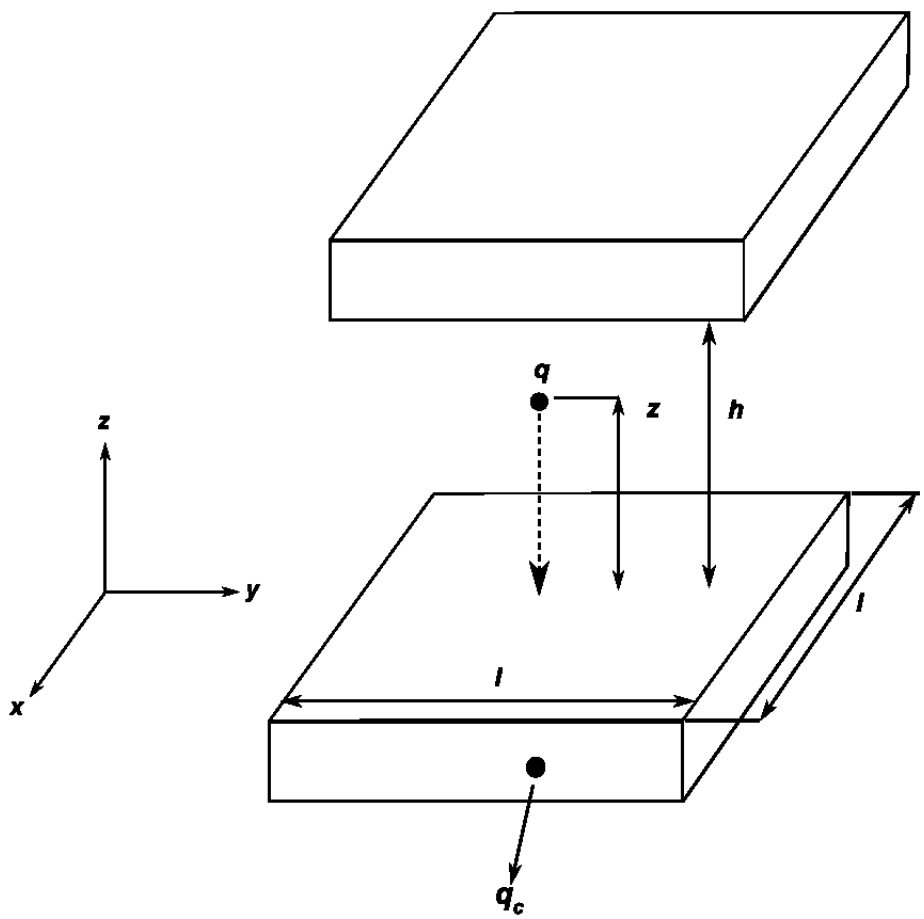

Figure 4.6: Illustration of transient image current.

$$q = \oint \vec{D} \cdot \mathtt{d}A \tag{4.4}$$

where $\vec{D}$ is the electric displacement field vector. For the case of the parallel plate geometry described above, the charge on the signal collecting electrode q_c is given by:

$$q_c = \int_{y=-\frac{l}{2}}^{\frac{l}{2}} \int_{x=-\frac{l}{2}}^{\frac{l}{2}} \epsilon E_z \mathtt{d}x\mathtt{d}y \tag{4.5}$$

where ϵ is the electrical permittivity. In this case, the electric field due to the charge q is expressed by [7]:

$$E_z = \frac{-qz}{4\pi\epsilon\left(x^2+y^2+z^2\right)^{3/2}} \tag{4.6}$$

Substituting of the electric field expression into the signal electrode charge expression yields:

$$q_c = -\frac{q}{\pi} \cdot \left[\sin^{-1}\left(\frac{l^2}{l^2+4z^2}\right)\right] \tag{4.7}$$

From the definition of conservation of electric charge, the current signal is defined as:

$$i_c = -\frac{\mathtt{d}q_c}{\mathtt{d}t} = \frac{4q}{\pi} \cdot \frac{1}{\cos\left(\sin^{-1}\left(\frac{l^2}{l^2+4z^2}\right)\right)} \cdot \frac{z \cdot l^2}{\left(l^2+z^2\right)^2} \cdot \frac{\mathtt{d}z}{\mathtt{d}t} \tag{4.8}$$

It is interesting to note that $\lim_{l\to\infty} i_c = 0$. In other words, as the dimensions of the collecting electrode increase with respect to the separation distance between the particle and the electrode, the induced current decreases.

Figure 4.7 plots the induced current signal predicted by equation (4.8)

as function of time before the particle arrives at the signal electrode, under the assumption that particle velocity is constant, i.e., $\mathtt{d}z/\mathtt{d}t = C$. For convenience, the induced current has been normalized by the conductive current $i_c(z=0)$ produced when the charged particle finally contacts the electrode. Current $i_c(z=0)$ can be calculated as:

$$\begin{aligned} i_c\left(z=0\right) &= \frac{8q}{\pi}\cdot\frac{\mathtt{d}z}{\mathtt{d}t}\cdot\lim_{z\to 0}\frac{1}{\cos\left(\sin^{-1}\left(\frac{l^2}{l^2+4z^2}\right)\right)}\cdot\frac{l^2 z}{\left(l^2+z^2\right)^2} \\ &= \frac{\sqrt{8}q}{\pi}\cdot\frac{\mathtt{d}z}{\mathtt{d}t}\cdot\frac{1}{l} \end{aligned} \tag{4.9}$$

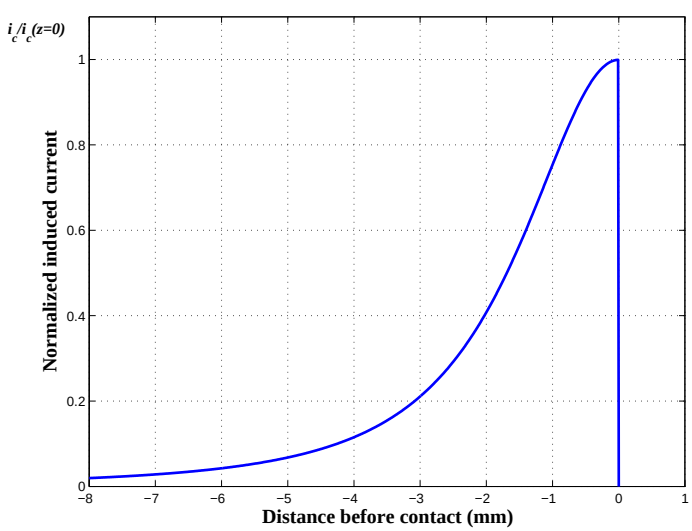

Figure 4.7: Normalized image current induced by a charged particle while approaching the electrode surface.

Figure 4.6 shows that the induced current goes up rapidly as the charged particle approaches the electrode surface. At the point just before the particle reaches the surface, the induced current is equal to the value of the conductive current. The average levels of transient current can be estimated based on

the equation (4.8). Furthermore, a simulation on the current estimation is carried out based on the following assumptions:

- the particle velocity is assumed to be constant, namely $\mathtt{d}z/\mathtt{d}t$ is constant.
- the particles are distributed randomly in space before approaching the substrate,.
- the total transient current of a group particles is considered to be the sum of the contribution of individual particle in the group.
- the time period of the calculation is 1s.

Additionally, the dimension of the electrode l is 8mm, particle velocity is set as 1 m/s. The calculations are carried out for different particle number concentrations, namely $10/\mathtt{cm}^3$, $30/\mathtt{cm}^3$, $100/\mathtt{cm}^3$, $300/\mathtt{cm}^3$, $1000/\mathtt{cm}^3$, $3000/\mathtt{cm}^3$ and $10{,}000/\mathtt{cm}^3$. Figure 4.8 plots the calculated transient image current as the function of time under different particle number concentrations: $10/\mathtt{cm}^3$, $30/\mathtt{cm}^3$ and $100/\mathtt{cm}^3$ and $300/\mathtt{cm}^3$. Figure 4.9 shows the calculated transient current under higher particle number concentrations: $1000/\mathtt{cm}^3$, $3000/\mathtt{cm}^3$ and $10{,}000/\mathtt{cm}^3$.

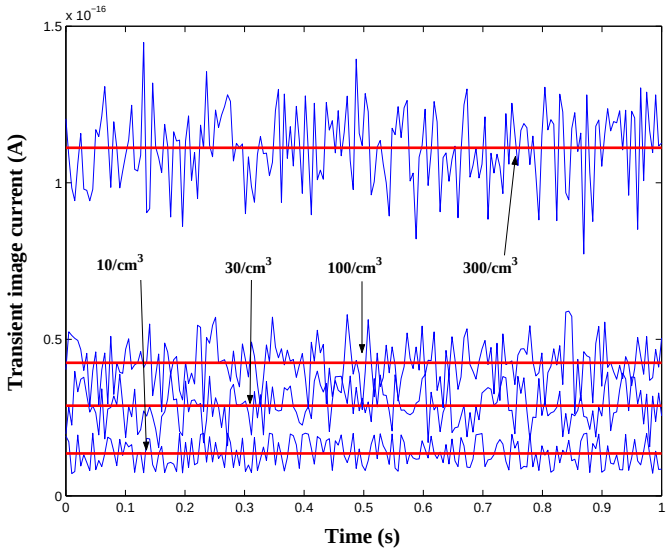

Figure 4.8: Transient image currents for particle number concentrations $10/\mathtt{cm}^3$, $30/\mathtt{cm}^3$, $100/\mathtt{cm}^3$ and $300/\mathtt{cm}^3$.

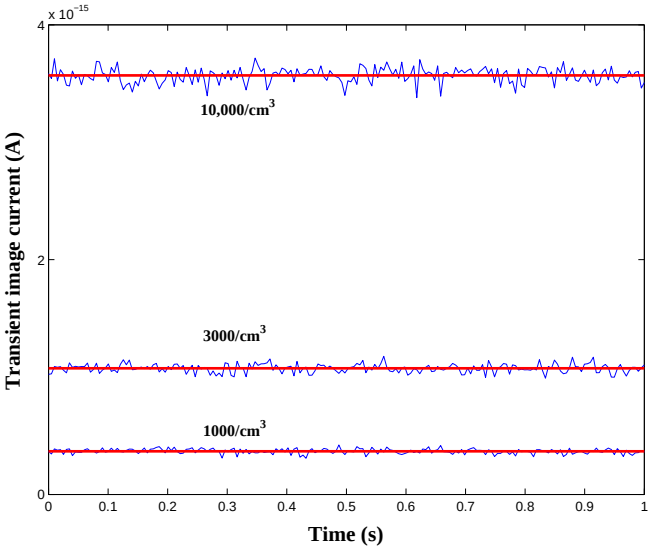

Figure 4.9: Transient image currents for particle number concentrations $1000/\mathtt{cm}^3$, $3000/\mathtt{cm}^3$ and $10{,}000/\mathtt{cm}^3$.

Table 4.2 compares the mean value of the transient current $\bar{i}_c$ in a time period 1s (Figure 4.8 and 4.9), its standard deviation s_c as well as the coefficient of variation CV (a statistical measure of the deviation of a variable from its mean, defined as: $\frac{\texttt{Standard deviation}}{\texttt{Expected return}} = \frac{s_c}{\bar{i}_c}$) for different particle number concentrations.

Table 4.2: $\bar{i}_c$, s_c and CV of the image current under different particle number concentrations.

Particle concentration	$\bar{i}_c$(fA)	s_c(fA)	CV: $\frac{s_c}{\bar{i}_c} \times 100\%$
$10/\texttt{cm}^3$	0.0139	0.00423	30.43
$30/\texttt{cm}^3$	0.02846	0.00604	21.22
$100/\texttt{cm}^3$	0.0421	0.00676	16.05
$300/\texttt{cm}^3$	0.1124	0.0122	10.85
$1000/\texttt{cm}^3$	0.3650	0.0218	5.97
$3000/\texttt{cm}^3$	1.073	0.0379	3.53
$10{,}000/\texttt{cm}^3$	3.572	0.0630	1.76

Figure 4.10 shows CVs as the function of particle number concentrations.

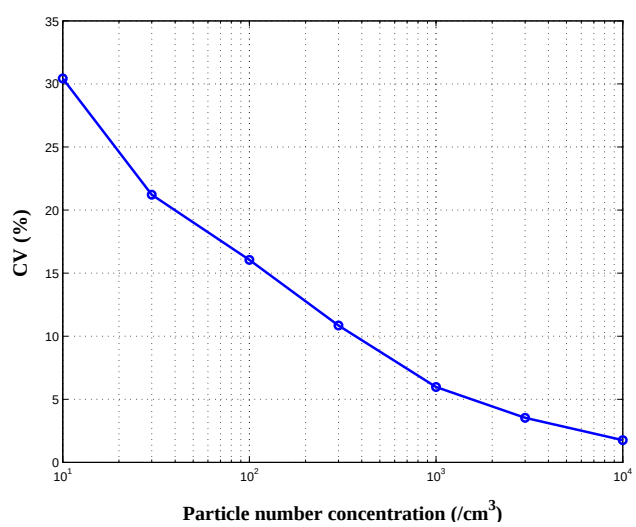

Figure 4.10: CVs at different particle number concentrations.

It can be concluded from above discussions:

- the average transient image current is increasing with the increase of particle number concentrations. For example, average image current at particle number concentration 10,000/$\mathtt{cm}^3$ is almost ten times larger than that of the current at a low number concentration 1000/$\mathtt{cm}^3$. This can be easily explained by the fact that higher particle number concentrations in general mean more charged particles within the same volume, thus can lead to more deposited particles, correspondingly, larger induced current.

- there is an approximate linear relationship between particle number concentration and the average image current when concentration is large sufficiently. For instance, the average image current corresponding to the number concentration 3000/$\mathtt{cm}^3$ is 1.073fA, which is nearly three times of the current 0.365fA, corresponding to the number concentration 1000/$\mathtt{cm}^3$. However, this relationship is no more valid when particle number concentration is very low (e.g., number concentration less than 100/$\mathtt{cm}^3$).

- *CVs* corresponding to low particle number concentrations (e.g. 10/$\mathtt{cm}^3$ or 30/$\mathtt{cm}^3$) are relatively large and vice versa. For example, the CV for particle number concentration 30/$\mathtt{cm}^3$ is more than 20%, while for number concentration 10/$\mathtt{cm}^3$ is near 30%. Larger CV in general means less representative of the obtained results, in other words, the currents obtained under low particle number concentrations have low reliability.

Chapter 5

Experimental results

The preceding chapters have been related to the more conceptual aspects of this work, such as backgrounds, theories and designing. It is already known that the designed prototype consists three major components, namely a corona diffusion charger, an ion precipitator and an electrical precipitator. Each component of the prototype can be characterized by one or more important parameters, in particular, diffusion charger characterized by particle charging efficiency η_c and mean charge n_p, ion precipitator by applied voltage U_c and electrical precipitator by particle deposition efficiency η_d. This chapter will focus on the experiments carried out to obtain these parameters, and it is outlined as follows:

- section 5.1 describes the experiment to measure particle charging efficiency.
- section 5.2 presents the measurement of particle mean charge.
- section 5.3 gives a description on the experiment of measuring particle deposition efficiency.
- section 5.4 describes the method to measure the particle surface area concentration based on the experiment results.

5.1 Measurement of particle charging efficiency

5.1.1 Experimental set-up

The experimental set-up used for measuring particle charging efficiency is schematically shown in Figure 5.1.

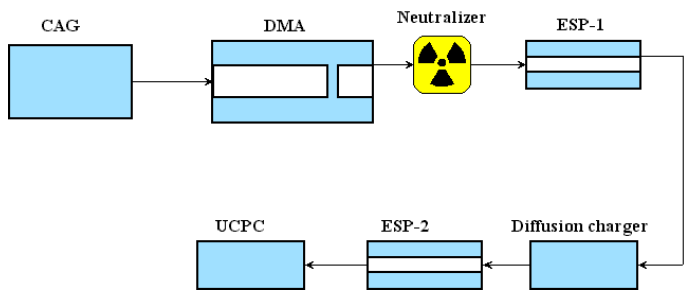

Figure 5.1: Schematic diagram of experimental set-up for measuring particle charging efficiency.

It is seen in the figure, a Combustion Aerosol Generator (CAG) was employed to generate an aerosol, which was further transported to a DMA to obtain electrostatically monodisperse particles. The outgoing particles passed through a Krypton-85 bipolar charge neutralizer and an ESP (ESP-1) to ensure that particles were electrically neutralized before entering the corona diffusion charger. Once leaving the charger, particles would enter the second ESP (ESP-2), which was further connected to an UCPC.

The particle charging efficiency can be defined via following expression:

$$\eta_c = \frac{N_2 - N_3}{N_1} \tag{5.1}$$

where N_1 represents the particle number concentration measured by UCPC while no voltage is applied neither to the diffusion charger nor to the second ESP; N_2 is the number concentration measured when the voltage of the charger is on, but that of the second ESP is off and N_3 is the number concentration measured when both voltages are on. Therefore, by switching the

voltage (applied to the second ESP) on or off, the variation of particle number concentration within the diffusion charger can be obtained, thus particle charging efficiency can be estimated according to expression (5.1).

Generally, particle charging efficiency will be influenced by the following factors:

- particle diameter d_p.
- corona voltage U_c.
- flow rate, including the aerosol flow Q_a and clean air flow Q_c.

In the experiments, the values for corona voltage and flow rate must be chosen carefully. Both low and high corona voltage are not suitable. Low voltage may lead to a situation where ions are insufficiently produced, thus leading to a poor charging efficiency; while high corona voltage may cause corona spark-over phenomena. The corona voltage used in the present experiment is set as $3.76kV$ (about 8mA corona current), the amount of ions produced under this voltage proves to be sufficient to guarantee an acceptable charging efficiency. Two different flow ratios (the ratio of aerosol flow to clean air flow) adopted in the experiment are: aerosol flow 1l/min to clean air flow 0.8l/min as well as aerosol flow 1l/min to clean air flow 1l/min. For the convenience of the following discussion, the ratio of aerosol flow to clean air flow will be denoted as ACR. Thus, two above-mentioned ACRs are 1.25 (1:0.8) and 1 (1:1), respectively. The influences of aerosol flow, clean air flow and particle diameter on charging efficiency are experimentally investigated and the results are presented in section below.

5.1.2 Experimental results

The measured charging efficiencies as a function of particle diameter under two ACRs 1.25 and 1 are plotted in Figures 5.2 and 5.3.

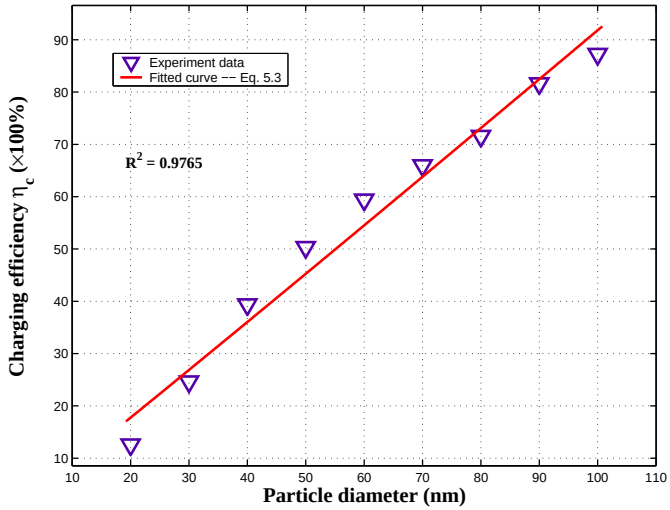

Figure 5.2: Particle charging efficiency measured with ACR 5:4.

Both Figures show that the particle charging efficiencies increase with the growing of particle diameters. This is in agreement with the studies in other references [6, 21, 27, 59]. This conclusion can be explained by the fact that larger particles tend to acquire electron charges more easily, thus charging efficiencies for larger particles appear in consequence higher than that of smaller particles.

Based on the experiment data, the correlation between particle size and charging efficiency can be quantitatively established, and one effective way is to fit the obtained data by means of some proper mathematical models. In the present study, a one-term power model is utilized. In general a one-term power model can be expressed as follows:

$$y = a \cdot x^b \tag{5.2}$$

where a and b are coefficients to be determined. The experiment data (plotted in Figures 5.2 and 5.3) can be fitted by using this model as:

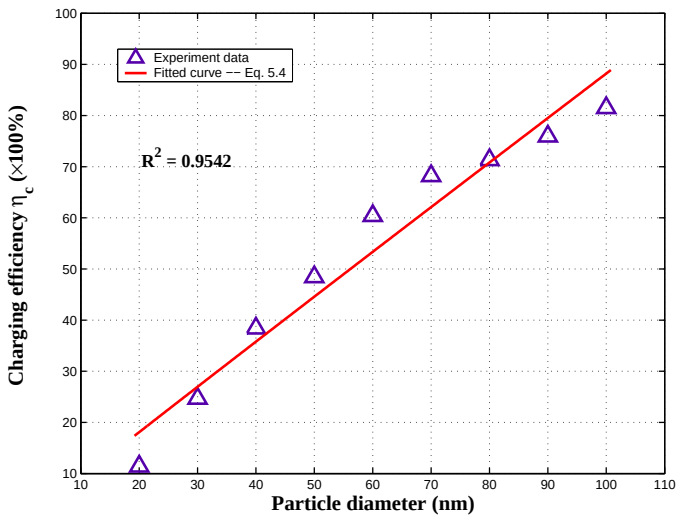

Figure 5.3: Particle charging efficiency measured with ACR 1:1.

$$\eta_c\left(d_p\right) = 0.009704 \cdot d_p^{0.9805} \tag{5.3}$$

and

$$\eta_c\left(d_p\right) = 0.009468 \cdot d_p^{0.9847} \tag{5.4}$$

where particle charging efficiency $\eta_c\left(d_p\right)$ is dimensionless and particle diameter d_p is in nanometer.

It should be pointed out that there may exist other models, for instance the polynomial or the non-parametric model, which are able to give the same results in terms of fitting goodness. Nevertheless, the power model has a least two attractive advantages. First, particle charging efficiency η_c can be expressed by a function of particle diameter d_p in a very concise manner by using this model. Second, if particle mean charge n_p and particle deposition efficiency can also be expressed by the identical model, then a clear connection might be established in-between these three parameters (particle charging efficiency, mean charge and deposition efficiency). The experiments

measuring particle mean charge and deposition efficiency will be discussed in section 5.2 and 5.3.

5.2 Particle mean charge

The particle mean charge is another significant quantity associated with the diffusion charging. As demonstrated by particle diffusion charging theory introduced in section 3.1, the mean charges acquired by particles during diffusion charging depends on several parameters, including the particle diameter d_p, the particle residence time t and the ion concentration n_i in the charging zone. Theoretically, the mean charge obtained by the particles can be estimated by using those kinetic charging models as long as several key parameters above-mentioned (i.e. particle residence time and ion concentration) are available. Unfortunately, it is not easy to measure the ion concentration accurately due to the complexity of flow pattern after the collision of aerosol flow and clean air flow within the diffusion charger. Taken this fact into account, the mean charge of the particles will also be measured by means of experiments.

5.2.1 Experimental set-up

The experimental setup for measuring particle mean charge is illustrated in Figure 5.4.

A CAG was used to produce the required aerosol particles. Then these aerosol particles were passed through a DMA to generate an electrically monodisperse aerosol. The outgoing particles were further passed through a Krypton-85 bipolar charge neutralizer to bring their charges to the Boltzmann equilibrium level. After that the particles were passed through an ESP to remove the excess ions to ensure that they were neutralized before entering the diffusion charger. At this moment, a Scanning Mobility Particle Sizer (SMPS), working on the principle of electrical mobility [26, 56], was used to

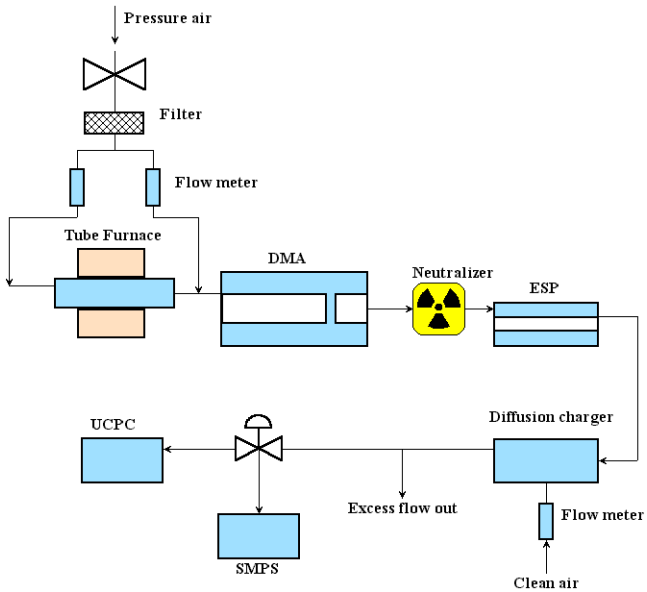

Figure 5.4: Schematic diagram of measuring particle mean charge n_p.

scan the incoming charged particle to obtain its size distribution. Within the SMPS, particles with the correct electrical mobility enter a small gap, which is located near the exit pipe and be collected by an UCPC. As the scanning voltage varies, the particle size changes accordingly. In this way, the information about particle size spectrum can be obtained by varying the scanning voltage in a wide range.

5.2.2 Experimental results

In order to measure mean charge level imposed upon the particle, the following experimental procedures were executed:

1. generate required monodisperse aerosol particles using a DMA.
2. determine the particle charge levels, and acquire particle number concentrations at these charge levels from a SMPS simultaneously.

3. calculates the mean charge acquired on the particles.

4. repeats steps 1 to 3 to obtain mean charges for particles in other sizes.

Above steps could be further demonstrated by an example of measuring the mean charge on 50nm particles. According to step 1, the DMA selected the electrically monodisperse particles 50nm in diameter. Then particles were charged in the diffusion charger. The SMPS would record the data about particle number concentrations and scanning voltages, with their relation being plotted in Figure 5.5.

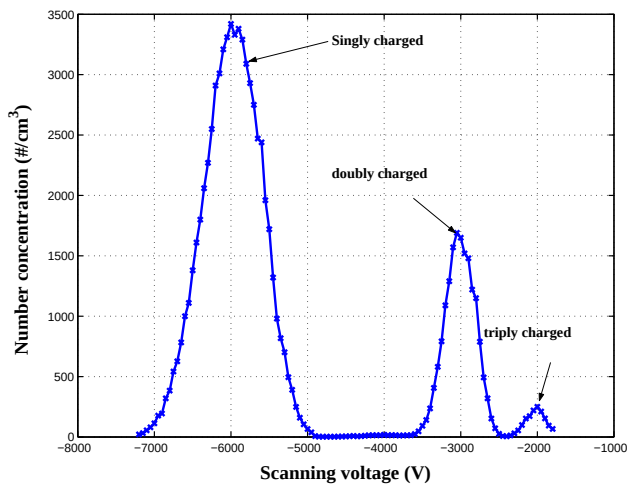

Figure 5.5: Particle number concentration *vs.* scanning voltage for d_p = 50nm.

As can be seen in the Figure, there are three obvious concentration peaks locating at scanning voltage $6kV$, $3kV$ and $2kV$, respectively. The three peaks correspond to the number concentrations of singly, doubly and triply charged particles. Once the particle number concentration is known, particle size and scanning voltages, mean charges acquired on the specified particle can be estimated through the following steps:

1. use a proper model (e.g. a log-norm distribution) to fit the obtained data (particle number concentration *vs.* scanning voltage, shown in Figure 5.5) to acquire parameters needed in step 2.

2. use a suitable model (e.g. Gauss distribution) and the parameters from step 1 to fit the experimental data (particle diameter *vs.* number concentration) to compute the mean charges.

By repeating above steps 1 to 3 for particle in other sizes, a complete spectrum of mean charge acquired on particle can be obtained. Figure 5.6 plots the particle charge distribution with size ranging from 20nm to 100nm at ACR 1.25.

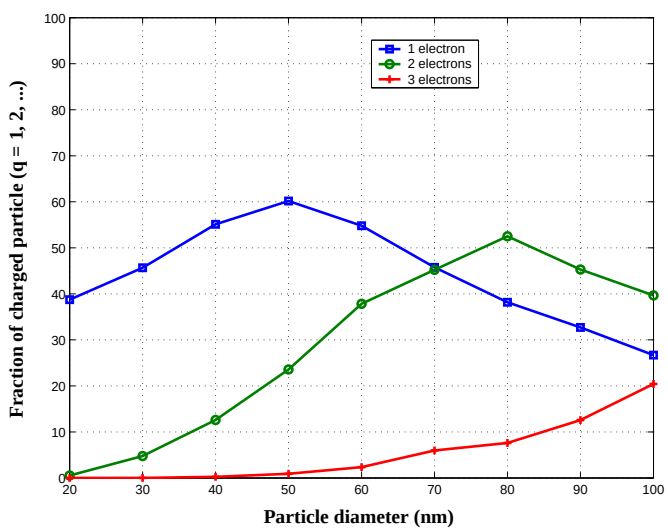

Figure 5.6: Particle charge level *vs.* diameter.

Figures 5.7 and 5.8 plot the calculated average charge acquired as a function of particle size ranging from 20nm to 100nm under ACRs 5:4 and 1:1.

These Figures show that average charges acquired on particles increase with their sizes. For example, particles with diameter less than 50nm obtain less than one electron on average; while particles large than 80nm can acquire

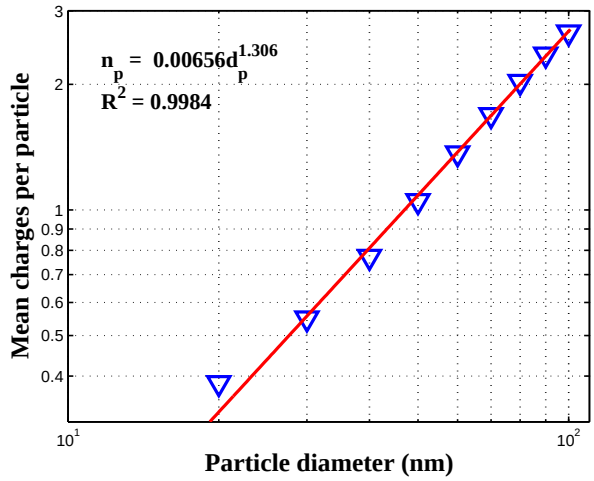

Figure 5.7: Mean charges per particle with ACR 5:4.

more than two electrons. In addition, it is easy to see that there exists an approximate linear relationship between average charges and particle diameter in both double-log plots, and it can be described, by means of a power model, as:

$$n_p = 0.00656 \cdot d_p^{1.306} \tag{5.5}$$

and

$$n_p = 0.007337 \cdot d_p^{1.283} \tag{5.6}$$

where the mean charge on particle n_p is a dimensionless number and particle diameter d_p is in nanometer.

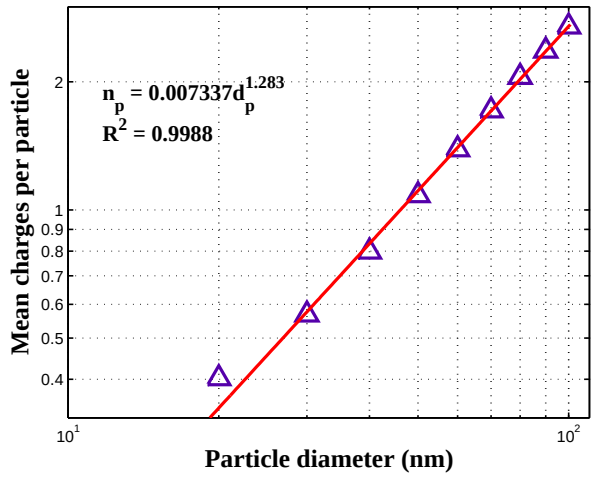

Figure 5.8: Mean charges on particle with ACR 1:1.

5.3 Particle deposition

5.3.1 Experimental set-up

The experiments in this section focus mainly on the measurement of particle deposition efficiency η_d, which is a quantity to describe the fraction of particles actually deposited within the electrical precipitator. The schematic diagram of the experimental set-up is illustrated in Figure 5.9.

As can be seen in the figure, particles leaving the diffusion charger were passed through a low-voltage ion precipitator so that the excess ions were able to be removed. In the present experiment, the applied voltage was set as $2\,V$. According to the calculation in section 4.2, most ions can be deposited within the precipitator, and most charged particles can pass through it smoothly under this voltage. Experiments showed that particle loss under this voltage is less than 1%. After leaving the ion precipitator, particles entered an electrical precipitator where they were precipitated. At the final stage of the experimental set-up, an UCPC was connected to the electrical precipitator in order to measure the particle number concentrations. Based

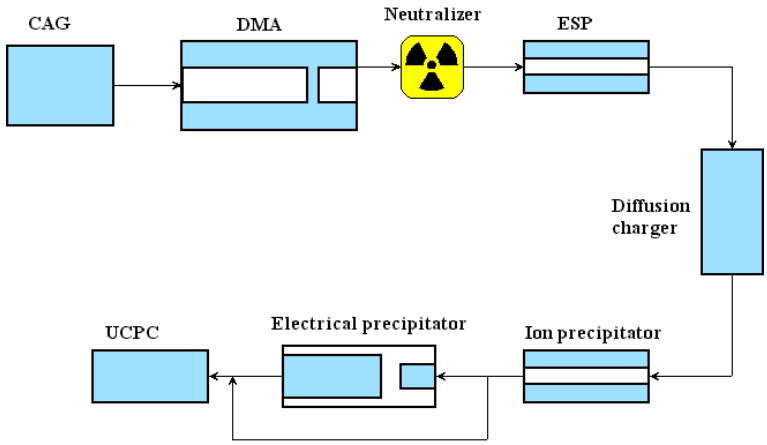

Figure 5.9: Deposition efficiency measurement.

on the equation (3.49) in section 3.4.2, particle deposition efficiencies can be estimated as:

$$\eta_d = \frac{N_1 - N_2}{N_1} \tag{5.7}$$

where N_1 is the particle number concentration measured without the deposition voltage being applied, and N_2 is the number concentration measured with the deposition voltage being applied. Therefore, by switching the applied voltage on or off, the variation of particle number concentration (i.e., $N_1 - N_2$) within the precipitator can be obtained, furthermore the particle deposition efficiency can be estimated by means of above expression.

5.3.2 Experimental results

The particle deposition efficiencies at different deposition voltages and ACRs are measured. The chosen ACRs are still 5:4 (aerosol flow 1 l/min and clean air flow 0.8 l/min) and 1:1 (both of them are 1 l/min). The deposition voltages are in turn $1kV$, $2kV$, $3kV$ and $4kV$, respectively. The deposition efficiencies measured at ACR 5:4 are shown in Figures 5.10–5.13.

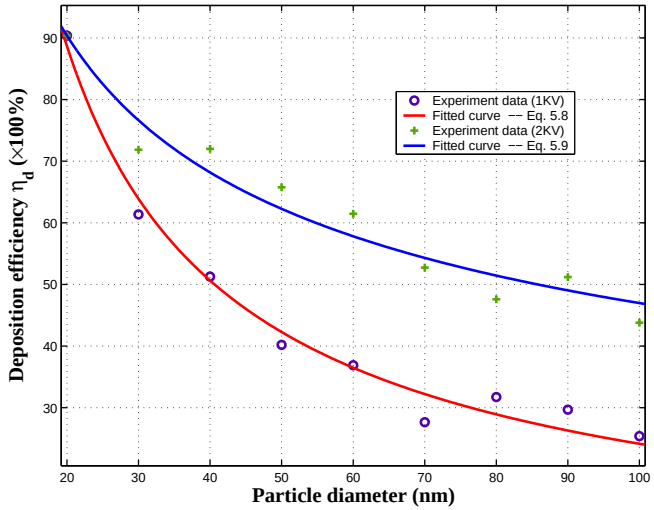

Figure 5.10: Particle deposition efficiency at depositing voltages $1kV$ and $2kV$ with ACR 5:4.

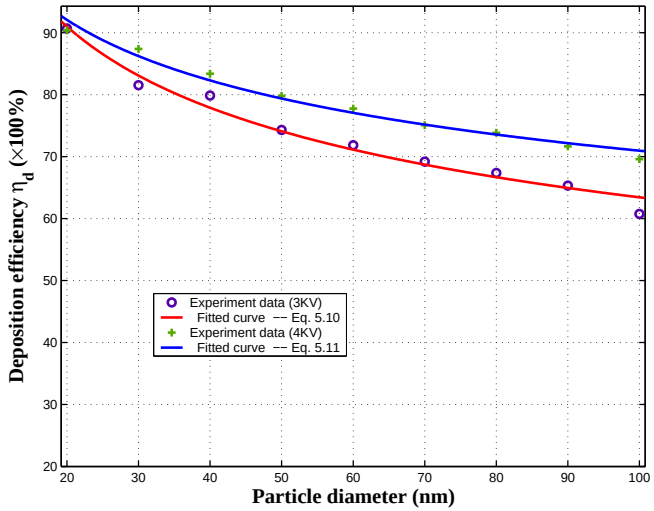

Figure 5.11: Particle deposition efficiency at depositing voltages $3kV$ and $4kV$ with ACR 5:4.

As Figures 5.10 and 5.11 show, particle deposition efficiencies decrease when their sizes increase for the same applied deposition voltage. Meanwhile, deposition efficiencies increase with the elevation of applied deposition

voltages for particles with identical sizes. The reason is that higher voltage will induce stronger electrostatic field, thus larger electrostatic force can exert on the charged particles so as to drive more of them to be deposited.

Once the experimental data is obtained, it is able to establish a quantitative relationship between the particle size and the deposition efficiency. A one-term power model is implemented for the fitting job, which is analogous to dealing with the particle charging efficiency. Based on this model, the relationship between the particle size and the deposition efficiency, shown in Figures 5.10–5.13, can be expressed as follows:

$$\eta_d\left(d_p\right) = 9.983 \cdot d_p^{-0.8082} \tag{5.8}$$

$$\eta_d\left(d_p\right) = 3.054 \cdot d_p^{-0.4065} \tag{5.9}$$

$$\eta_d\left(d_p\right) = 1.781 \cdot d_p^{-0.2242} \tag{5.10}$$

$$\eta_d\left(d_p\right) = 1.495 \cdot d_p^{-0.1619} \tag{5.11}$$

Figures 5.12–5.13 plot the deposition efficiency as a function of particle diameter with ACR 1:1.

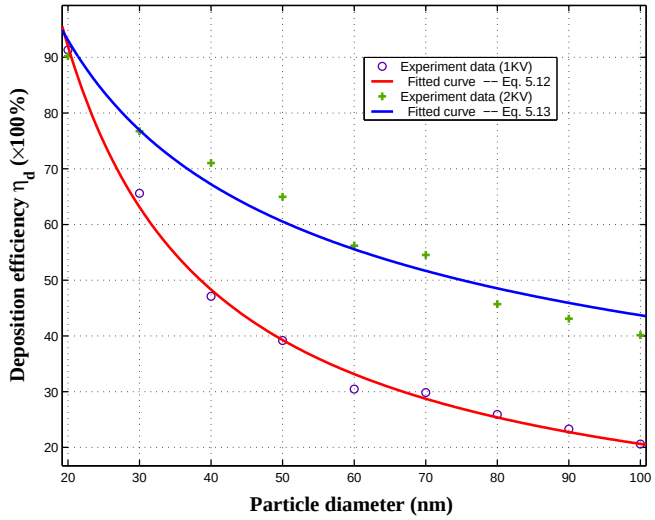

Figure 5.12: Particle deposition efficiency at depositing voltages $1kV$ and $2kV$ with ACR 1:1.

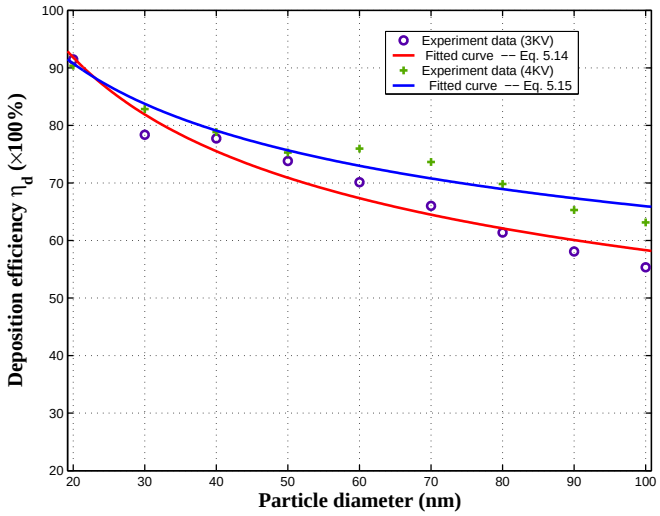

Figure 5.13: Particle deposition efficiency at depositing voltages $3kV$ and $4kV$ with ACR 1:1.

Similarly, the following empirical expressions are obtained to fit the measurement data in Figures 5.12–5.13.

$$\eta_d\left(d_p\right) = 14.88 \cdot d_p^{-0.9292} \tag{5.12}$$

$$\eta_d\left(d_p\right) = 3.802 \cdot d_p^{-0.4697} \tag{5.13}$$

$$\eta_d\left(d_p\right) = 2.138 \cdot d_p^{-0.2821} \tag{5.14}$$

$$\eta_d\left(d_p\right) = 1.645 \cdot d_p^{-0.1985} \tag{5.15}$$

The measured efficiencies with ACR 5:4 are further compared with the calculated efficiency by means of CFD model described in chapter 3. The following Figures compare the measured and calculated deposition efficiencies for the deposition voltages ranging from $1kV$ to $4kV$. The full extent of the error bars in these Figures show the range of two standard deviations of the measured values ($\pm\sigma$).

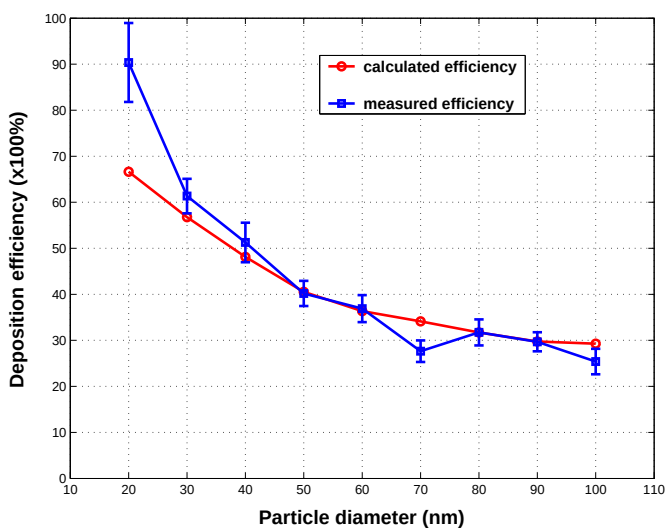

Figure 5.14: Comparison between measured and calculated deposition efficiency at $1kV$ with ACR 5:4.

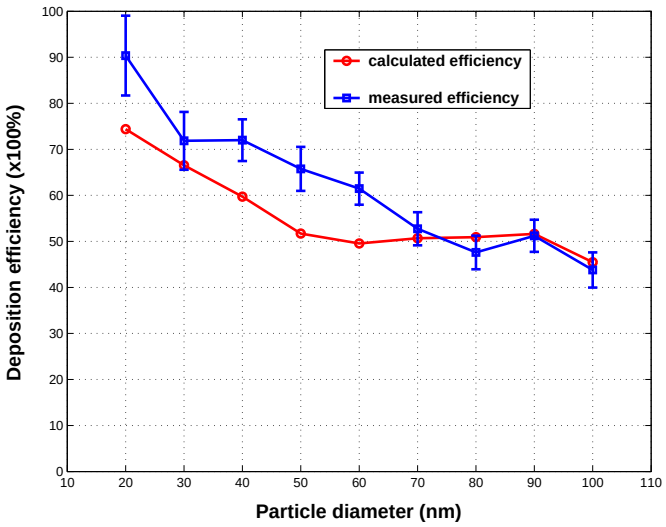

Figure 5.15: Comparison between measured and calculated deposition efficiency at $2kV$ with ACR 5:4.

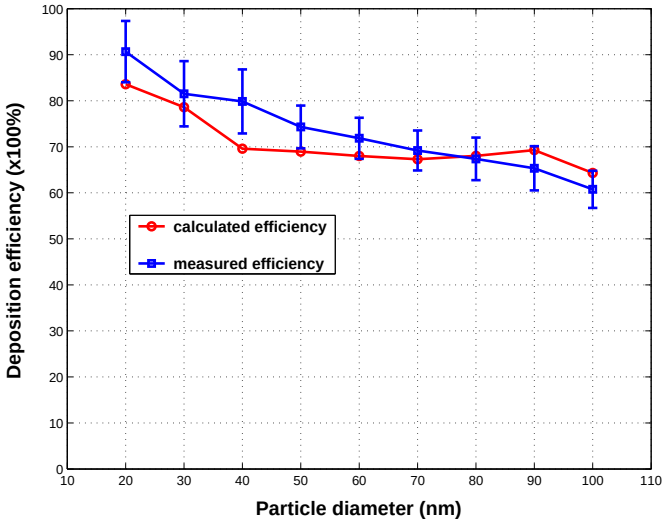

Figure 5.16: Comparison between measured and calculated deposition efficiency at $3kV$ with ACR 5:4.

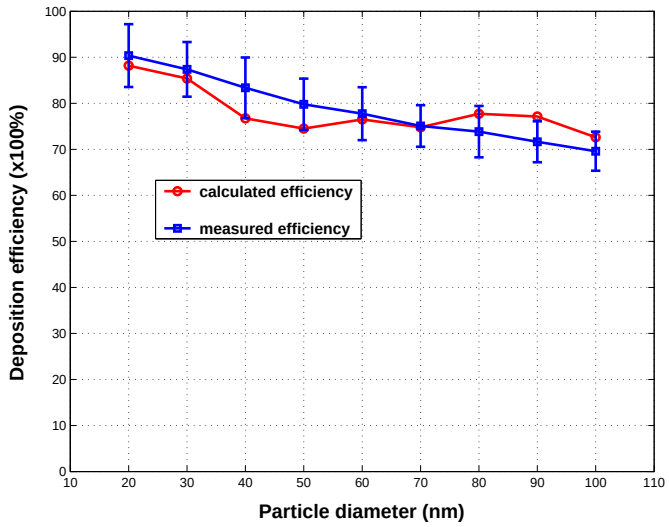

Figure 5.17: Comparison between measured and calculated deposition efficiency at $4kV$ with ACR 5:4.

Following conclusions can be drawn from these figures:

- the calculated deposition efficiency agrees well with the measured efficiency, it basically reflects the variation trend of the measured deposition efficiency.
- the particle deposition efficiency decreases with the increase of particle size for a given deposition voltage. For example, the deposition efficiency at $4kV$ decreases from 90% for particle 20nm in diameter to 70% for particle with 100nm in diameter,
- the particle deposition efficiency increases with the elevating of deposition voltage for particles with identical sizes. For instance, the deposition efficiency increases from 40% at $1kV$ to 80% at $4kV$ for particle 50nm in diameter. This conclusion is in agreement with other references [11, 12].

The experiments also shows that the particles will experience some losses

while passing through the electrical precipitator (Figure 5.9), the diffusion charger and the ion precipitator. The particle losses within the electrical precipitator are mainly caused by diffusion loss mechanism, and can be estimated by means of measuring the particle concentrations at the inlet and the outlet of the electrical precipitator without applying the deposition voltage. The measured particle losses for different ACRs are shown in Figure 5.18.

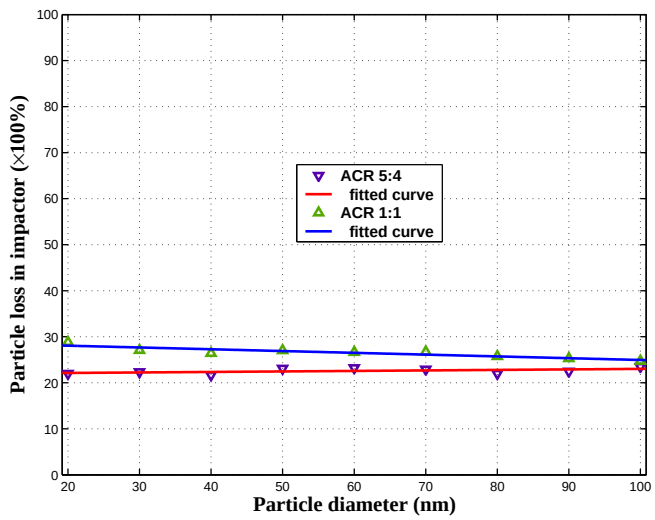

Figure 5.18: Particle losses within the electrical precipitator with ACRs 5:4 and 1:1.

As can be seen in the Figure, particle losses remain almost unchanged as the particle sizes increase. They are about 30% and 23% for ACR 1:1 and 5:4, respectively. Since the lost charged particles do not contribute to the signal current to be measured, the current equation (5.20) should be corrected by multiplying a factor, namely:

$$I = N_0 \cdot \eta_c \cdot n_p \cdot (1 - \eta_l) \cdot \eta_d \cdot \mathsf{e} \cdot Q \tag{5.16}$$

where η_l stands for the particle losses within the electrical precipitator.

5.4 Measuring particle surface area concentration

By combining the obtained empirical formulas to describe particle charging efficiency η_c, particle mean charge n_p and particle deposition efficiency η_d and equation (3.54), it is possible to derive a relationship between the signal current I and the particle diameter d_p. By using this relationship as a starting point, the connection between signal current I and particle surface area S_p can be established due to the relation between S_p and d_p, i.e. $S_p \propto d_p^2$. Clearly, the equation (3.54) is the key and its validity should be verified firstly. The next two subsections present the verification works carried out based on using both monodisperse and polydisperse aerosol.

5.4.1 Verification by means of monodisperse aerosol

A direct way of verifying equation (5.16) is to compare the signal current estimated using this equation with the measured current. The signal current induced by the deposited charged particle can be estimated from equation (3.54) as particle number concentration, ACRs, particle charging efficiency η_c, particle mean charge n_p and particle deposition efficiency η_d are all known.

Figures 5.19-5.22 compare measured and calculated signal currents under the operating conditions: monodisperse aerosol size ranging from 20nm to 100nm, ACR 5:4 and applied deposition voltages U_d ranging from $1kV$ to $4kV$.

Figures 5.23-5.26 compare the measured and calculated currents under the same operating conditions with the only exception that ACR is 1:1.

It can be seen in these Figures that the general agreements between the calculated current and the measured current are reasonable well represented.

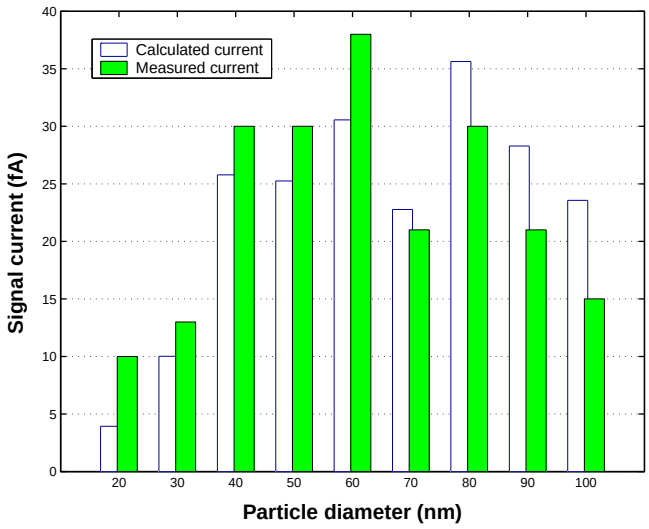

Figure 5.19: Comparison between measured and calculated current (ACR = 5:4, $U_d = 1kV$).

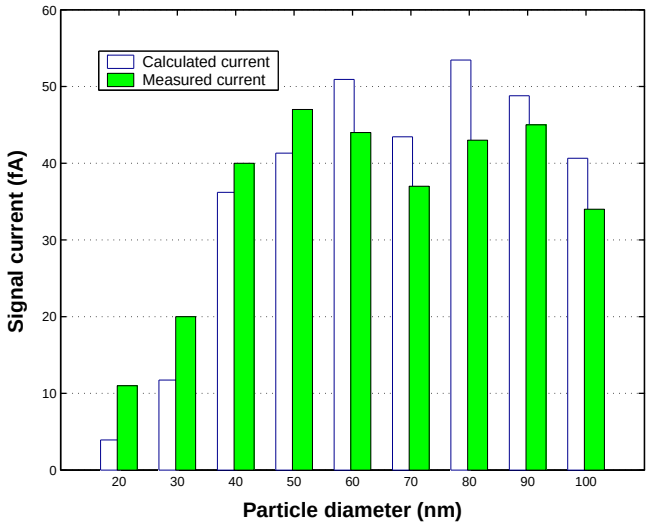

Figure 5.20: Comparison between measured and calculated current (ACR = 5:4, $U_d = 2kV$).

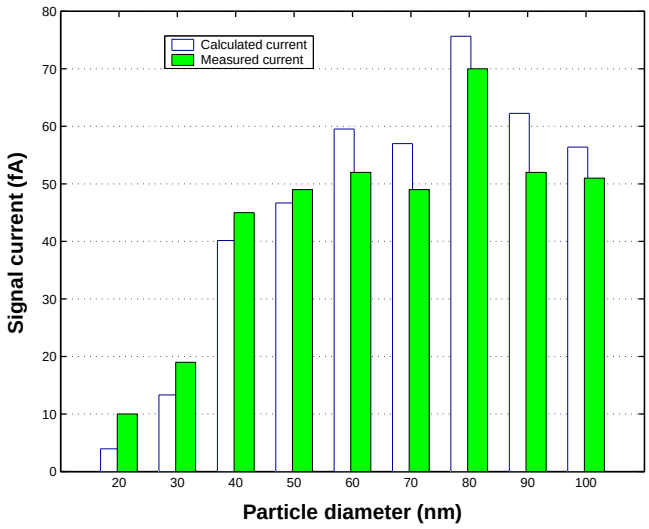

Figure 5.21: Comparison between measured and calculated current (ACR = 5:4, $U_d = 3kV$).

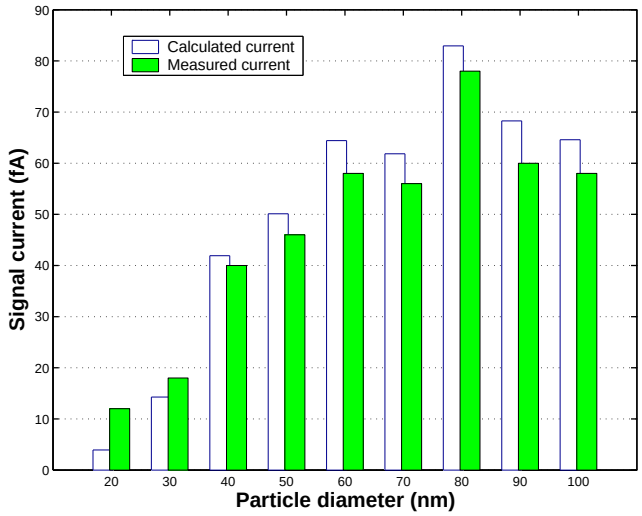

Figure 5.22: Comparison between measured and calculated current (ACR = 5:4, $U_d = 4kV$).

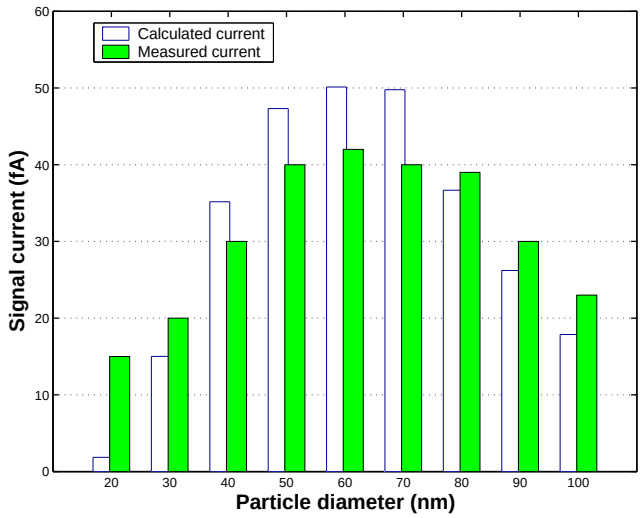

Figure 5.23: Comparison between measured and calculated current (ACR = 1:1, $U_d = 1kV$).

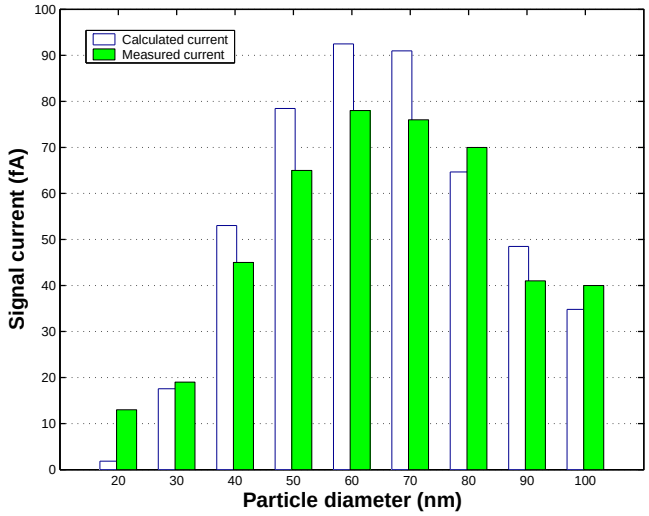

Figure 5.24: Comparison between measured and calculated current (ACR = 1:1, $U_d = 2kV$).

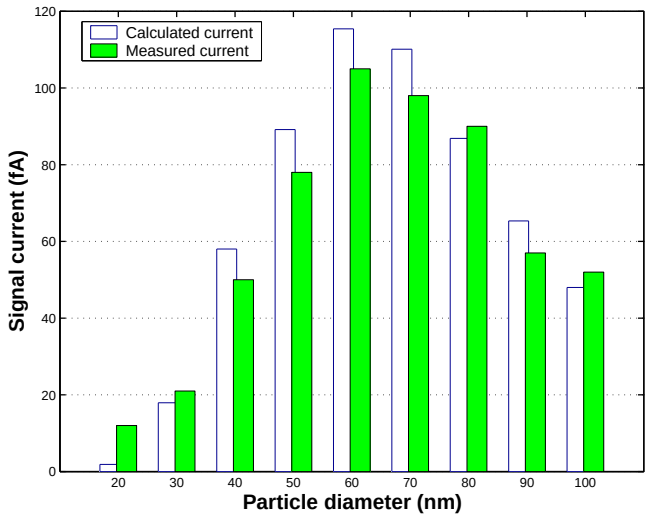

Figure 5.25: Comparison between measured and calculated current (ACR = 1:1, $U_d = 3kV$).

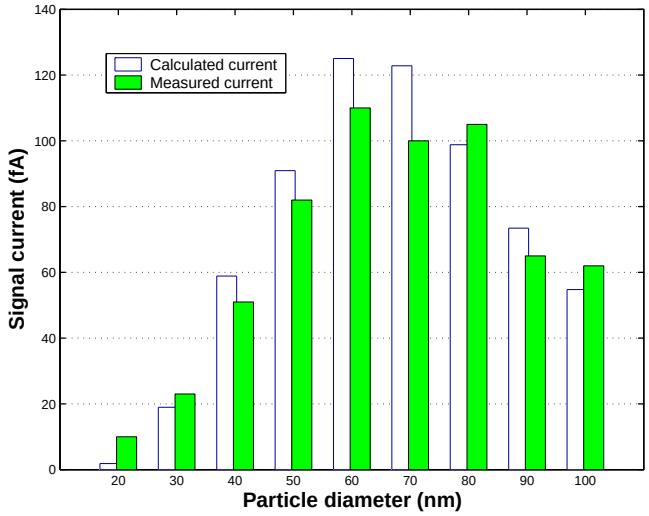

Figure 5.26: Comparison between measured and calculated current (ACR = 1:1, $U_d = 4kV$).

5.4.2 Verification by means of polydisperse aerosol

Equation (3.54) for estimating the signal current in the case of monodisperse aerosol has been verified in the previous subsection. This subsection will further verify the current equation (3.55) in the case of polydisperse aerosol.

The experimental set-up adopted in this case is shown in Figure 5.27.

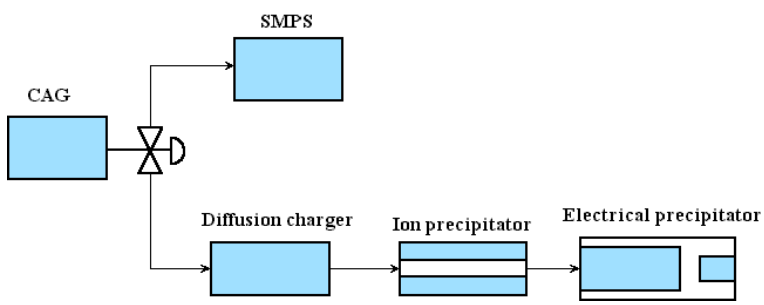

Figure 5.27: Schematic diagram of the verification using polydisperse aerosol.

Table 5.1: Basic parameters of the particle size distributions measured with SMPS.

Aerosol (#)	d_p (nm)	d_g (nm)	σ_g	N (/cm^3)
1	38.19	35.01	1.52	8.50×10^6
2	75.08	60.93	1.86	7.07×10^6
3	119.61	89.02	2.11	4.14×10^6

The polydisperse aerosol was generated using a CAG. Then a three-way valve was employed to divert the aerosol flow and make it either pass through a SMPS or a designed prototype. When polydisperse aerosol passed through the SMPS, its number concentration was measured and recorded, and it was fed into the equation (5.21) to calculate the signal current. When the aerosol passed through the prototype, on the other hand, the induced signal current was measured by a very sensitive electrometer. Thus the measured current was able to be compared with the calculated current. Table 5.1 reports the basic parameters of the particle size distributions measured by using the SMPS, while figure 5.28 plots their number concentration distributions.

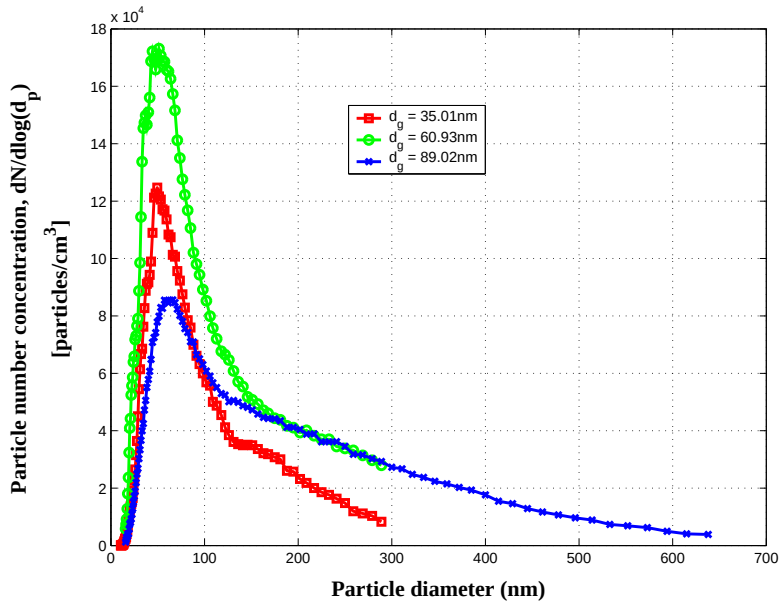

Figure 5.28: Particle number concentrations *vs.* diameters measured with SMPS.

Figures 5.29–5.31 compare the measured and calculated signal currents at different deposition voltages and size distributions. The full extent of the error bars in these Figures show the range of two standard deviations of the measured values ($\pm\sigma$).

Figure 5.32 compares the calculated and the measured current at different particle number concentrations.

It is clear from these figures that the agreement between calculated and measured current signals is quite good in terms of both different particle size distributions as well as number concentrations. By observing these figures, one can conclude that current signals increase with the increase of deposition voltage. This is because the larger voltages cause generally more deposited charged particles, which further lead to a larger induced current. In addition, as demonstrated in Figure 5.32, high particle number concentrations may lead to large signal current due to the fact that more particles have chances to be

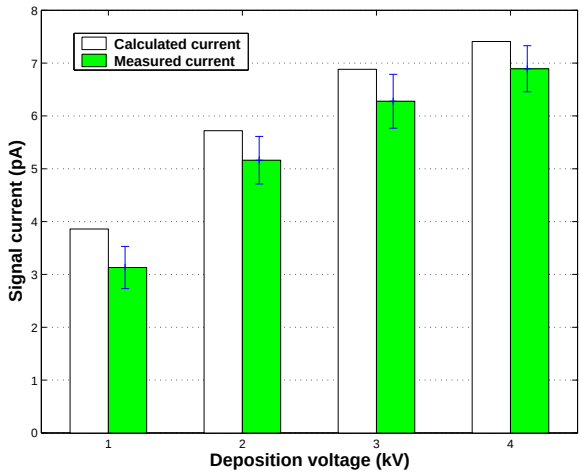

Figure 5.29: Comparison between measured and calculated current (ACR = 1.25, $d_g = 35.01$nm).

deposited in this situation.

5.4.3 Measuring particle surface area concentration

As pointed out at the beginning of this section, equation (3.54) is the key as particle surface area concentration is expected to be inferred from it. This equation indicates that the signal current I is a function of particle charging efficiency η_c, mean charge n_p and deposition efficiency η_d. All these parameters have to be obtained from experiments, and they are described in equations (5.3-5.4), (5.5-5.6) and (5.8-5.15), respectively. It is not difficult to draw the following conclusions from these equations:

- they are exponential functions,
- the powers of the charging efficiency functions and the mean charge functions are positive,
- the powers of the deposition efficiency functions are negative,

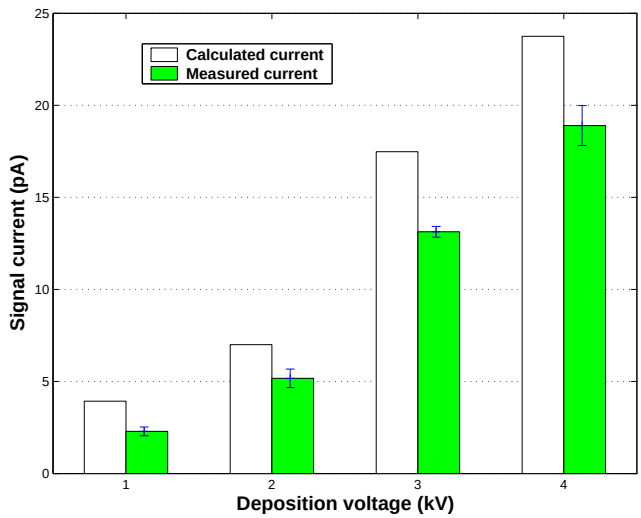

Figure 5.30: Comparison between measured and calculated current (ACR = 1.25, $d_g = 60.93$nm).

- there exists a relationship between the powers of deposition efficiency functions and the applied deposition voltages, that is the low deposition voltage corresponds to large power value (absolute value) and vice versa.

For the convenience of later discussion, above exponential functions are expressed, by using general form, as:

$$\eta_c\left(d_p\right) = \alpha_1 \cdot d_p^{\beta_1} \tag{5.17}$$

$$q_p\left(d_p\right) = \alpha_2 \cdot d_p^{\beta_2} \tag{5.18}$$

$$\eta_d\left(d_p\right) = \alpha_3 \cdot d_p^{\beta_3} \tag{5.19}$$

where α_1, α_2, α_3, β_1, β_2 and β_3 are constants to be determined by means of fitting the experiment data. Substituting above equations into equation

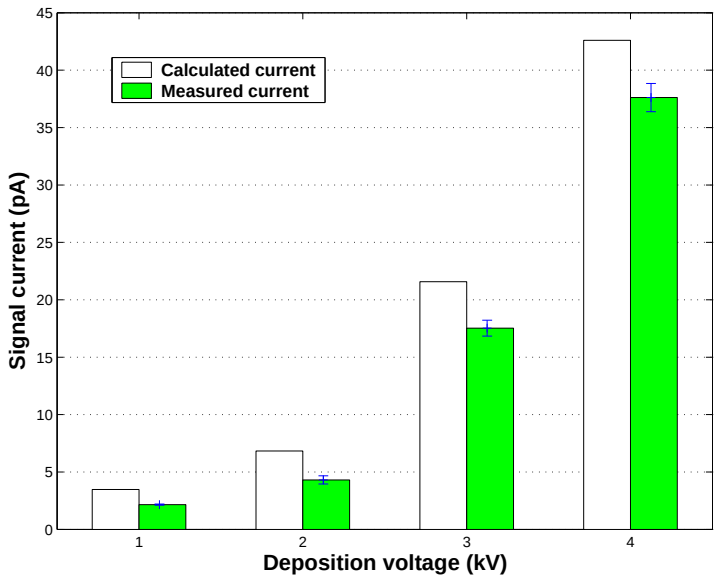

Figure 5.31: Comparison between measured and calculated current (ACR = 1.25, $d_g = 89.02$nm).

(3.54) yields:

$$I = N_0 \cdot \alpha_1 \cdot \alpha_2 \cdot \alpha_3 \cdot d_p^{\beta_1+\beta_2+\beta_3} \cdot \mathtt{e} \cdot Q \propto d_p^{\beta_1+\beta_2+\beta_3} \tag{5.20}$$

since α_1, α_2, α_3, $\mathtt{e}$ and Q are all constants, equation (5.20) actually shows that current I is proportional to an exponential function $d_p^{\beta_1+\beta_2+\beta_3}$ of particle diameter d_p. Of course equation (5.20) is only used to describe the current produced by monodisperse aerosol. In order to deal with polydisperse aerosol, the corresponding equation should be written as:

$$I = \int_{d_{min}}^{d_{max}} \alpha_1 \cdot \alpha_2 \cdot \alpha_3 \cdot d_p^{\beta_1+\beta_2+\beta_3} \cdot \mathtt{e} \cdot Q \cdot \mathtt{d}N \tag{5.21}$$

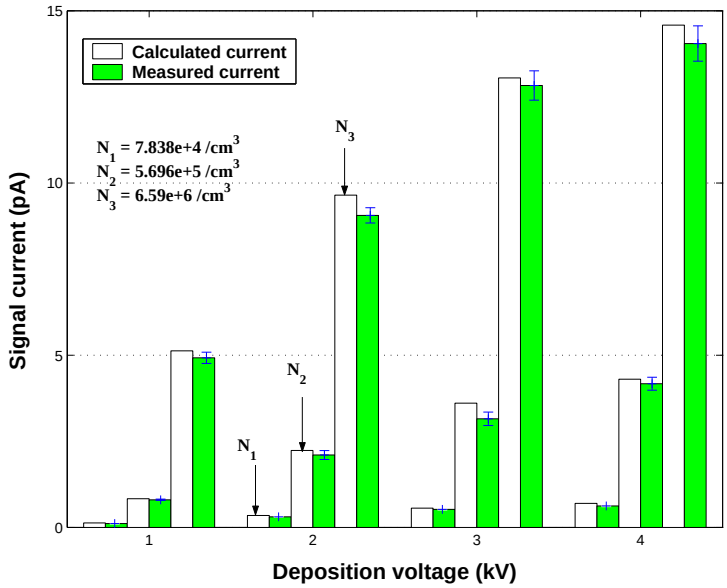

Figure 5.32: Comparisons between measured and calculated currents for different aerosols (parameters listed in Table 5.4).

$$\propto \int_{d_{min}}^{d_{max}} d_p^{\beta_1+\beta_2+\beta_3} \mathrm{d}N \tag{5.22}$$

where d_{min} and d_{max} represent the lower- and upper limit of the interesting particle size interval. Equation (5.21) demonstrates that signal current induced in the case of polydisperse aerosol is proportional to the integration of a specified exponential function of particle diameter over the interesting particle size interval.

Now much attention should be focused on the power $\beta_1 + \beta_2 + \beta_3$ of the particle diameter, since the value determines the geometrical meaning of the function $d_p^{\beta_1+\beta_2+\beta_3}$. Clearly, provided that the sum $\beta_1 + \beta_2 + \beta_3$ is 2, one can promptly see from above equation:

$$\int_{d_{min}}^{d_{max}} d_p^{\beta_1+\beta_2+\beta_3} \mathtt{d}N = \int_{d_{min}}^{d_{max}} d_p^2 \mathtt{d}N \tag{5.23}$$

The right-hand side of this equation times a constant π represents exactly the total particle surface area concentration of the particles with sizes falling within the interval $[d_{min}, d_{max}]$.

With the above idea, the next question is how to adjust these parameters in order to make them satisfy the condition: $\beta_1+\beta_2+\beta_3 = 2$. Before adjusting these parameters, it is necessary to understand their physical meanings:

1. parameters β_1 and β_2 are associated with the diffusion charging process, and their values will be affected by both aerosol flow and clean air flow for a given corona voltage.

2. parameter β_3 is relevant to the particle deposition process, and its value is influenced not only by the flows (aerosol and clean air) but also by the deposition voltage.

Therefore, the values of β_1 and β_2 will remain unchanged, provided that the flow rates do not change. As for β_3, with its value depending on both the flow rate and the applied deposition voltage, β_3 can be changed by either adjusting the flow rate or the deposition voltage. In the practice, it is more easy and convenient to change the deposition voltage while maintaining the flow rate unchanged. The reason is that changing deposition voltage has impacts only on parameter β_3; while altering flow rates will affect not only parameters β_3 but also other two parameters β_1, β_2. Based on this consideration, the strategy of changing exponents β_3 to adjust the sum of $\beta_1 + \beta_2 + \beta_3$ will be adopted in the present experiment. Concretely, it is necessary to know the relation between the deposition voltage and the exponent β_3, and this can be obtained by measuring the deposition efficiencies at different deposition

voltages. Figure 5.33 plots β_3 as a function of deposition voltage at different ACRs.

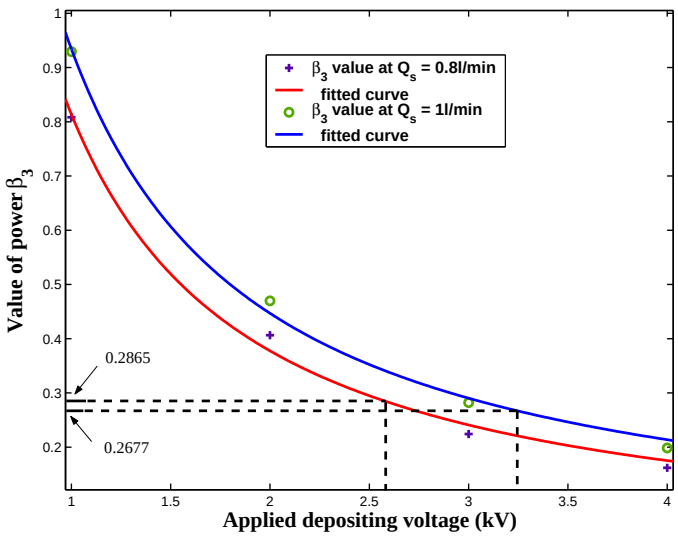

Figure 5.33: Deposition voltage *vs.* exponent β_3.

As can be seen in the Figure, the variable β_3 can be approximately determined from the curve when the applied deposition voltage is given. Below is an example of determining the applied voltage at ACR 5:4. First, it is necessary to know the values of β_1 and β_2, and they can be estimated from equations (5.3) and (5.5) as β_1= 0.9805 and β_2= 1.306. With the values β_1 and β_2, β_3 can be calculated by means of the relation $\beta_3 = 2 - \beta_1 - \beta_2$ as β_3= -0.2865. When β_3 is obtained, the corresponding deposition voltage can be determined from the blue curve shown in Figure 5.33. Table 5.2 reports calculated deposition voltages U_d with respect to β_3.

Table 5.2: Calculated deposition voltages.

ACR	β_1	β_2	β_3	$U_d(kV)$
1.25	0.9805	1.306	-0.2865	2.72
1	0.9847	1.283	-0.2677	3.24

It is easy to see from Table 5.2 that the sum $\beta_1+\beta_2+\beta_3$ at two ACRs can be 2 by setting the deposition voltage as $2.72kV$ and $3.24kV$, respectively. When $\beta_1+\beta_2+\beta_3$ takes the value 2, the current equation (5.21) can be written as:

$$I = \int_{d_{min}}^{d_{max}} \alpha_1 \cdot \alpha_2 \cdot \alpha_3 \cdot d_p^2 \cdot \mathsf{e} \cdot Q \cdot \eta_l \cdot \mathsf{d}N \tag{5.24}$$

which can be further rearranged as:

$$\int_{d_{min}}^{d_{max}} \pi d_p^2 \mathsf{d}N = \frac{\pi}{\alpha_1\alpha_2\alpha_3} \cdot \frac{I}{\eta_l \mathsf{e} Q} \tag{5.25}$$

The left hand side of above equation is exactly the total surface area concentration S_p of particles falling within the size interval $[d_{min},\ d_{max}]$. Thus S_p can be expressed by:

$$S_p = \frac{\pi}{\alpha_1\alpha_2\alpha_3} \cdot \frac{I}{\eta_l \mathsf{e} Q} \tag{5.26}$$

At this moment, the surface area concentration can be estimated by measuring the signal current at those deposition voltages U_d. Below is an instruction on how to estimate particle surface area concentration. First, it is necessary to determine the value of voltage U_d due to the previous discussion. Table 5.2 shows that U_d is $2.72kV$, and the corresponding β_3 is -0.2865 at ACR 5:4. Then, the coefficient α_3 at this voltage U_d must be estimated, and it can be obtained from Figure 5.34, which plots the α_3 as a function of the deposition voltage.

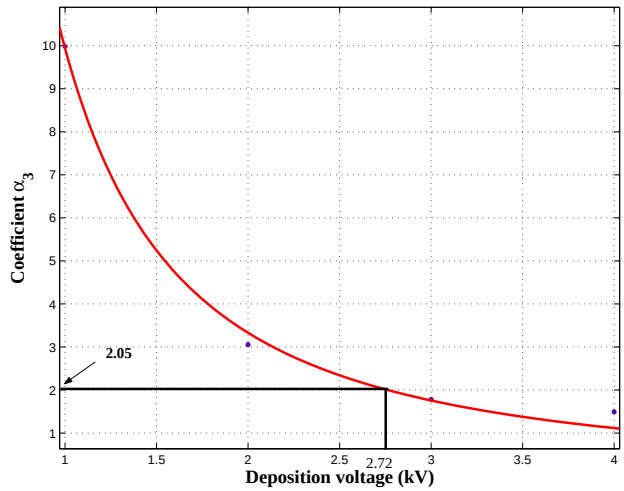

Figure 5.34: Deposition voltage *vs.* coefficient α_3.

When the signal current I, the values α_3 and β_3 are known, the particle surface area concentration can be promptly calculated by means of equation (5.26). Table 5.3 reports the calculated surface area concentrations under different particle size distributions, with the basic parameters being listed in Table 5.4.

Table 5.3: Calculated particle surface area concentrations.

Aerosol (#)	Measured current (pA)	Particle surface area concentration ($\mu\mathtt{m}^2/\mathtt{cm}^3$)
1	0.455±5.39%	4.534×10^3±5.39%
2	2.930±6.20%	2.921×10^4±6.20%
3	11.240±3.31%	1.124×10^5±3.31%

Table 5.4: Parameters of the particle size distribution obtained from SMPS.

Aerosol (#)	d_p (nm)	d_g (nm)	σ_g (nm)	N ($/\mathtt{cm}^3$)
1	104.27	77.55	2.04	7.839×10^4
2	94.34	68.35	2.08	5.696×10^5
3	68.34	60.22	1.65	6.596×10^6

Figure (5.35) shows the particle number concentration distribution for $N_i = 6.59 \times 10^6/\mathtt{cm}^3$.

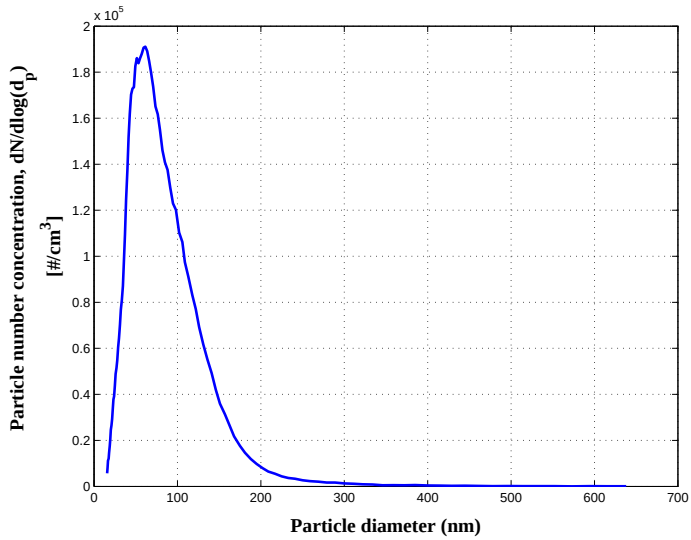

Figure 5.35: Particle number concentration distribution for $N_i = 6.59 \times 10^6/\mathtt{cm}^3$.

With the known particle size distribution, the particle surface area concentration can be expressed as:

$$S_p = \sum_{i=1}^{M} N(i) \cdot \pi d_{pi}^2 \tag{5.27}$$

where M is the total number of particle size intervals, $N(i)$ is the mean particle number concentration in ith size interval, and d_{pi} is the average particle diameter in ith interval.

Figure (5.36) shows the relationship between the surface area concentration and the measured signal current. It is easy to draw a conclusion from the figure that there exists a linear relationship between the measured signal current and the surface area concentration (as the slope of the curve is 0.997). In addition, the signal current scales with the surface area concentration, and

this is exactly the goal of the design.

Figure (5.37) compares the particle surface area concentrations predicted from the measured current and the surface area concentration calculated from the obtained particle size distributions under the same operating conditions. As shown in the figure, they agree with each other very well. On the whole, the surface area concentrations inferred from the particle size distributions are slightly larger than that of calculated from the measured current. The general discrepancy between them is between 10% and 12% for different particle size distributions.

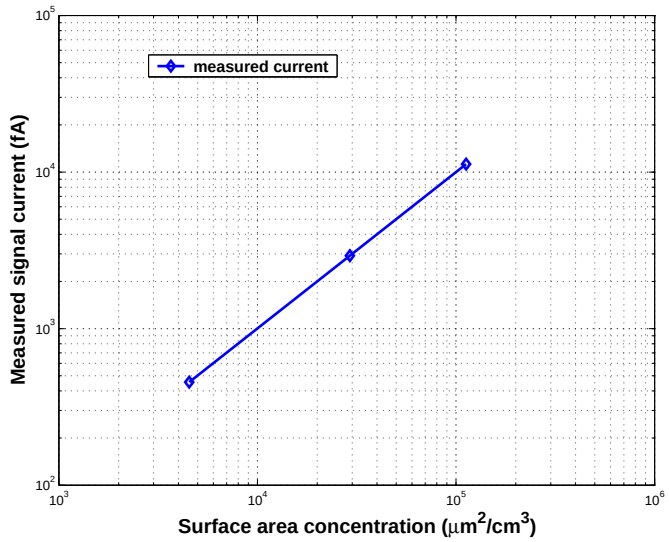

Figure 5.36: Surface area concentration *vs.* measured signal current.

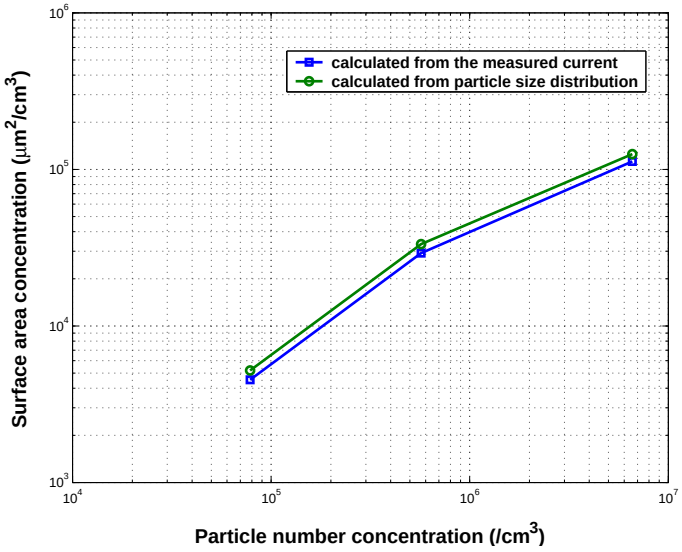

Figure 5.37: Comparison of surface area concentrations calculated from the measured current and the particle size distributions (parameters cf. Table 5.4).

Chapter 6

Conclusions

A new method for measuring surface area concentration of ultrafine particles has been proposed and verified in this dissertation. This measurement method involves a three-step operational process: corona diffusion charging, ion precipitation and charged particle deposition. First, particle charging is accomplished by corona diffusion charging, which will impose the incoming aerosol particles with a specified known charge distribution. Once the aerosol particles are charged, they pass through an ion precipitator to remove the excess ions. Then the charged particles are deposited by means of an electrostatic field established within a precipitator. Finally the signal current induced by the charged particles in the deposition process is measured by a highly sensitive electrometer to infer the particle surface area concentration.

To verify the proposed method, an experiment prototype, including a corona diffusion charger, an ion precipitator and an electrical precipitator, was designed and built. Each part of the prototype is characterized by one or more operating parameters. For example, two major operating parameters pertaining to the diffusion charger are the corona voltage and the ACR. Corona voltage have impacts on amounts of generated ions, and a corona voltage 3.76kV (corresponding to 8mA corona current) is employed in the present experiments; while ACR exerts influence on particle residence time

in the charging zone. Two different ACRs used in the present experiments are 5:4 (aerosol flow 1l/min *vs.* clean air flow 0.8l/min) and 1:1 (aerosol flow 1l/min *vs.* clean air flow 1l/min), respectively. The most important parameter associated with the ion precipitator is the precipitating voltage. A $2V$ low voltage is applied to the ion precipitator based on the theoretic calculation. This voltage will ensure that almost all ions can be deposited and most charged particles can pass through the ion precipitator smoothly. As for the electrical precipitator, the deposition voltage is the most significant operating parameter and four deposition voltages $1kV$, $2kV$, $3kV$ and $4kV$ are applied in the experiment.

The experiments carried out presently focused on measuring the particle charging efficiency, the particle mean charge as well as the particle deposition efficiency, with the goal to find a relationship between these parameters and particle diameters. The empirical expressions for describing these parameters are obtained by means of fitting techniques based on the experiment data. In our work, the one term power model proved to be able to give a satisfied results in terms of fitting goodness, and play the role of a bridge to link the signal current and the particle diameter. Starting from these empirical formulas, it is not difficult to establish the relationship between the signal current and the particle surface area concentration. The experiment results show that the power $(\beta_1 + \beta_2 + \beta_3)$ of particle diameter can shift to 2 by adjusting the value of β_3 to a specified value, and the latter can be realized by altering the deposition voltages. For instance, the analysis in chapter 5 show that the required β_3 can be obtained by changing the deposition voltage to $2.72kV$ for ACR 1.25, then the total particle surface area concentration can be inferred from the signal current measured at this voltage.

It should be pointed out that, although above empirical expressions were obtained by using particles with sizes ranging from 20nm to 100nm, they proved to be still valid for particles larger than 100nm. As shown in section 5.4.2, these formulas were utilized in the estimation of the signal current of

polydisperse aerosol particles (Table 5.1) without correction, and the calculated signal current is still in good agreement with the measured signal current. However, the agreement between the estimated current and the measured current for small particles (e.g. 20nm in diameter) is not so good, and the measured currents are in most cases larger than calculated currents (Figures 5.19-5.26). One possible reason is that the mean charge on particle calculated based on the empirical formula is less than the actual charge (Figure 5.7 and 5.8). However, more studies are needed to find a more convincing explanation to this problem.

Bibliography

[1] G. Abmadi and A. Li. Dispersion and deposition of spherical particles from point sources in a turbulent channel flow. *Aerosol Sci. Tech.*, 16:209–226, 1992.

[2] P. J. Anderson, D. J. Wilson, and A. Hirsch. *Respiratory tract deposition of ultrafine particles in subject with obstructive or restrictive lung disease*, volume 97. 1990.

[3] George K. Batchelor. An introduction to fluid dynamics. *Cambridge University Press*, 2000.

[4] A brief introduction to ESP. http://www.eas.asu.edu/ holbert/wise/electrost.

[5] B. Brunekreef, N. A. Janssen, J. de Hartog, H. Harssema, M. Knape, and P. van Vliet. Air pollustion from truck traffic and lung function in children living near motorways. *Epidemiology*, 8:298–303, 1997.

[6] P. Büscher. Entwicklung und Modellierung eines unipolaren Diffusions- und Feldaufladers für Partikel in Aerosolen. *Dissertation Universität-GH-Duisburg*, 1995.

[7] J. Crowley. Fundamentals of applied electrostatics. *John Wiley and Sons, New York*, 1986.

[8] E. Cunningham. On the velocity of steady fall of spherical particles through fluid medium. *Proc. R. Soc.*, A 83:357–365, 1910.

[9] J. J. De Hartog, P. H. Van Vliet, B. Brunekreef, M. C. Knape, N. A. Janssen, and H. Harssema. Relationship between air pollution due to traffic, decreased lung function and airway symptoms in children. *Ned Tijdschr Geneeskd*, 141:1814–1818, 1997.

[10] M. Dennekamp, S. Howarth, C. A. Dick, J. W. Cherrie, K. Donaldson K, and A. Seaton. Ultrafine particles and nitrogen oxides generated by gas and electric cooking. *Occup Environ Med.*, 58(511-516), 2001.

[11] H. Dixkens, C. Strezeletz, F. Stratmann, and H. Fissan. Particle transport in an inhomogeneous electrostatic field under laminar flow conditions. *J. Aerosol Sci.*, 24:139–140, 1993.

[12] J. Dixkens and H. Fissan. Development of an electrostatic precipitator for off-line particle analysis. *Aerosol Sci. Tech.*, 30:438–453, 1999.

[13] K. Donaldson, X. Y. Li, and W. MacNee. Ultrafine particle mediated lung injury. *J. Aerosol Sci.*, 29:533–560, 1998.

[14] K. Donaldson, V. Stone, A. Clouter, L. Renwick, and W. MacNee. Ultrafine particles. *Occup Environ Med.*, 58:211–216, 2001.

[15] K. Donaldson, V. Stone, P. S. Gilmour, D. M. Brown, and W. MacNee. Ultrafine particles: mechanisms of lung injury. *Phil Trans R. SOC. London*, A. 358:2741–2829, 2000.

[16] Peters et. al. Association between mortality and air pollution in europa. *Enviro. Healt*, 108(4):283–287, 2000.

[17] R. C. Flagen. Aerosol measurement: Principles, techniques, and applications. *New York: John Wiley and Sons*, 2001.

[18] H. W. Gaggeler, U. Baltensperger, M. Emmenegger, D. T. Jost, A. Schmidt-Ott, P. Haller, and M. Hoffmann. The epiphaniometer, a new device for continuous aerosol monitoring. *J. Aerosol Sci*, 20:557–564, 1989.

[19] J. H. Goo and J. W. Lee. Stochastic simulation of particle charging and collection characteristics for a wire-plate electrostatic precipitator of short length. *J. Aerosol Sci.*, 28(5):875–893, 1997.

[20] J. Harrison, P. Brower, M. D. Attfield, C. B. Doak, M. J. Keane, and W. E. Wallace. Surface composition of respirable silica particles in a set of us anthracite and bituminous coal mine dusts. *J. Aerosol Sci.*, 28:689–696, 1997.

[21] A. Hernandez-Sierra, F.J. Alguacil, and M. Alonso. Unipolar charging of nanoparticle aerosol particles in a corona ionizer. *Journal of Aerosol Science*, 34:733–745, 2003.

[22] W. C. Hinds. Aerosol technology. *John Wiley and Sons, New York, USA*, 1982.

[23] Fluent Inc. Fluent 5.5 user guide. 1997.

[24] Keithley Inc. Internet website: http://www.keithley.com.

[25] White H. J. Particle charging in electrostatic precipitation. *AIEE Trans.*, 70(II):1186–1191, 1951.

[26] E. O. Knutson and K. T. Whitby. Aerosol classification by electric mobility: Apparatus, theory, and applications. *J. Aerosol Sci.*, 6:443–451, 1975.

[27] F. E. Kruis and H. Fissan. Nanoparticle charging in a twin hewitt charger. *J. Nanoparticle Res.*, 3:39–50, 2001.

[28] P. A. Lawless. Particle charging bounds, symmetry relations and an analytic charging rate model for the continuum regime. *J. Aerosol Sci.*, 27:191–215, 1996.

[29] P. J. Lioy, T. Wainman, J. Zhang, and S. Goldsmith. Typical household vacuum cleaners: the collection efficiency and emissions characteristics for fine particles. *J Air Waste Manag Assoc.*, 49:200–206, 1999.

[30] C. P. Mao. Fluid mechanics. *Shanghai Jiaotong University Press*, 1995.

[31] A. D. Maynard and R. L. Maynard. A derived association between ambient aerosol surface area and excess mortality using historic time series data. *Atmospheric Environment*, 33:309–321, 2002.

[32] A. Mizuno. Review of particle charging research. proceedings of the first international conference on electrostatic precipitation, monterey 1981. *Air Pollution Control Association*, pages 304–325, 1982.

[33] M. Neuberger. Cancer in men from fibrous and non fibrous mineral particles. *J. Aerosol Sci.*, 20:1349–1351, 1989.

[34] G. Oberdorster. Toxicology of ultrafine particles: In vivo studies. *Phil. Trans. R. Society, London*, A. 358:2719–2740, 2000.

[35] G. Oberdorster, R. M. Gelein, J. Ferin, and B. Weiss. Association of particulate air-pollution and acute mortality - involvement of ultrafine particles. *Inhalation Toxicology*, 7:111–124, 1995.

[36] B. Ostro and L. Chestnut. Assessing the health benefits of reducing particulate matter air pollution in the united states. *Environ Res*, 76:94–106, 1998.

[37] H. Ounis, G. Ahmadi, and J. B. McLaughlin. Brownian diffusion of submicrometer particles in the viscous sublayer. *J. Colloid Interface Sci.*, 143(1):266–277, 1991.

[38] S. N. Pandis, U. Baltensperger, J. K. Wolfenbarger, and J. H. Seinfeld. Inversion of aerosol data from the epiphaniometer. *J. Aerosol Sci*, 22:417–428, 1991.

[39] D. Pearce and T. Crowards. Particulate matter and human health in the united kingdom. *Energy Policy*, 24:609–620, 1996.

[40] F. W. J. Peek. Dielectric phenomena in high voltage engineering. *McGraw-Hill*, 1929.

[41] P. Penttinen, K. L. Timonen, P. Tiittanen, A. Mirme, J. Ruuskanen, and J. Pekkanen. Ultrafine particles in urban air and respiratory health among adult asthmatics. *European Respiratory Journal*, 109:319–323, 2001.

[42] A. Perters, D. W. Dockery, J. Heinrich, and H. E. Wichmann. Short-term effects of particulate air pollution on respiratory morbidity in asthmatic children. *European Respiratory Journal*, 10:872–879, 1997.

[43] C. A. Pope, D. W. Dockery, J. D. Spengler, and M. E. Rainzenne. Respiratory health and PM10 pollution – a daily time series analysis. *American Reiew of Respiratory Disease*, 144:668–674, 1991.

[44] J. Postendorfer, G. Robig, and A. Ahmed. Experimental determination of the attachment coefficients of atoms and ions on monodisperse aerosols. *J. Aerosol Sci.*, 10:21, 1979.

[45] S. N. Rogak, U. Baltensperger, and R. C. Flagan. Measurement of mass transfer to agglomerate aerosols. *Aerosol Sci. Tech.*, 14:447–458, 1991.

[46] K. E. Rosendahl. Health effects and social costs of particulate pollution - a case study for oslo. *Environmental Modeling and Assessment*, 3:47–62, 1998.

[47] D. Rosenfeld. Supression of rain and snow by urban and industrail air pollution. *Science*, 287:1793–1796, 2000.

[48] A. Schmidt-Ott and Th. Kauffeldt. Assessment of particulate air pollution by new sensor concepts. *VDI BERICHTE*, No. 1443:517–528, 1999.

[49] A. Schmidt-Ott and Z. D. Ristovski. Measurement of airborne particles. *Indoor Environment, ed. by L. Morawska and T. Salthamer, Wiley-VCH, Weinheim*, pages 56–81, 2003.

[50] H. Steiner, D. Windelberg, and B. Georgi. Aerosol generating during cutting of various material with plasma, laser and consumable electrode. *J. Aerosol Sci.*, 19:1381–1384, 1988.

[51] V. L. Streeler. Fluid mechanics. *McGraw-Hill*, 1979.

[52] V. Timbrell, P. Paakko, T. Ashcroft, L. O. Meurmann, and K. B. Shilkin. Similarities in the fibrogenicity of asbestos fibres and other mineral particles retained in human lungs. *Proceedings of the Seventh International Pneumoconioses Conference, Part 1, DHHS (NIOSH) Publication No. 90-108*, pages 182–189, 1990. Pittsburgh.

[53] M. J. Utell and M. W. Frampton. Acute health effects of ambient air pollution: the ultrafine particle hypothesis. *J Aerosol Med.*, 13:355–359, 2000.

[54] P. van Vliet, M. Knape, N. Janssen, H. Harssema, and B. Brunekreef. Motor vehicle exhaust and chronic respiratory symptoms in children living near freeways. *Environmental Research*, 74:116–121, 1997.

[55] L. A. Viehland and E. A. Mason. Transport properties of gaseous ions over a wide energy range, iv. *At. Data Nuc. Data Tab.*, 60:37–95, 1995.

[56] S. C. Wang and R. C. Flagan. Scanning electrical mobility spectrometer. *Aerosol Sci. Tech.*, 13:230–240, 1990.

[57] H. J. White. Particle charging in electrostatic precipitation. *AIEE Trans.*, 70(II):1186–1191, 1951.

[58] H. J. White. Industrial electrostatic precipitation. *Addison-Wesley, Reading MA.*, 1963.

[59] A. Wiedensohler. Die dipolare Diffusionsaufladung von Partikeln in chemisch traegen Reinstgasen. *Dissertation Universitaet-GH-Duisburg*, 1989.

[60] W. E. Wilson. Use of the electrical aerosol detector as an indicator for the total particle surface area deposited in the lung. *Proceedings of 2004 AEWMA, paper #37*, 2004.

[61] Renliang Xu. Particle characterization: Light scattering methods. *Kluwer Academic Publishers*, 2000.

Appendix A

A brief introduction to UDF

User Defined Functions (UDFs) are codes written in C or Fortran that allow the user to customize Fluent to his/her problem. According to Fluent, UDFs can be used for a variety of applications, some of which are listed below:

- Customization of boundary conditions, material property definitions, surface and volume reaction rates, sources terms in Fluent transport equations, source terms in user defined scalers transport equations, diffusivity functions, etc.
- Adjustment of computed values on a once-per-iteration basis.
- Initialization of a solution.
- Asynchronous execution of a UDF
- Post-processing enhancement
- Enhancement of existing FLUENT models (e.g., discrete phase model, multiphase mixture model, discrete ordinates radiation model).
- Moving grid problems.

To use a UDF, the function needs to be written in C using a text editor with extension *.c. UDFs are defined using the "Define macros" provided by Fluent. These macros are function declarations specified by Fluent. Define macros are split into five categories, general, model specific, multiphase, dynamic mesh, and DPM. In this project we are only concerned with the model specific Define macros which are used to set parameters. When the code is written, it needs to be either interpreted or compiled for use in Fluent. The UDFs are compiled in both ways but with different method. Interpreted UDFs are compiled during iteration. Compiled UDFs are first built and then loaded in a library ahead of time. Once this is accomplished, the name of the function becomes an option for the inputs where it can be implemented. UDFs can be used as boundary conditions, source terms and in various other locations. In present study UDFs are used to impose gas velocity at the boundary, and electrical force as well as Brownian force to particles.

Appendix B

UDF for predicting particle deposition efficiency

The following source codes written in the frame of UDF were used to calculate particle trajectories within the electrical precipitator. The codes are commented. Note that two arrays, e1 and e2, are utilized to store the values of electric field strength within the electrical precipitator. Those values are derived from QuickField directly. Each row of the arrays has four values. The first and second value represent the particle coordinate in z-axis and r-axis, while the third and fourth value stand for the magnitudes of electric field strength in z-axis and r-axis at this location. In this way, electric field strength in arbitrary location within the precipitator can be found quickly by locating the coordinates.

The electrical force as well as Brownian force have been defined in macro DEFINE_DPM_BODY_FORCE (particle_electrical_force, p, i), where structure p contains all the information about the particle being studied, for example, particle locations, velocities, mass, temperature, and so on. Index i is a indicator used to distinguish different directions. i takes three values 0, 1 and 2. For the source codes below, i=0 and i=1 represent z-axis and r-axis, respectively.

The macro DEFINE_DPM_SCALAR_UPDATE (positionxy, cell, thread, initialize, p) updates current particle coordinates and velocities, while DEFINE_PROFILE (inlet_x_velocity, thread, index) defines the profile of particle velocity at the inlet of the electrical precipitator.

```
#include "udf.h"
#include "dpm.h"
#include "random.h"
#define xv_init 0.884
#define r 0.001
#define Q 1*1.601e-19
//-------------------------------------------
static real bol = 1.38e-23 ; // Boltzmann constant
static real mu = 1.789e-05 ; // kinematic viscosity
static real rho = 1.225 ; // air density
static real lbda = 66e-09 ; // mean free path of gas molecules
//-------------------------------------------
real x , y ;
real gx, gy ;
//-------------------------------------------
float sx = 0.0002, sy = 0.00005; // space of x and y direction
float sx1 = 0.0002, sy1 = 0.0002;
int n1 = 31 , m1 = 20; //
int n2 = 41, m2 = 36 ;
int j, k;
float e1[][4] ={{0.000000, 0.000000, 0.000000, 2856.540000},
{0.000000, 0.000050, 0.000000, 7411.130000},
{0.000000, 0.000100, 0.000000, 11965.700000},
{0.000000, 0.000150, 0.000000, 16520.300000},
{0.000000, 0.000200, 0.000000, 21074.900000},
{0.000000, 0.000250, 0.000000, 25629.500000},
```

```
{0.000000, 0.000300, 0.000000, 30184.100000},
{0.000000, 0.000350, -120.466000, 33978.300000},
{0.000000, 0.000400, -481.863000, 36252.000000},
{0.000000, 0.000450, -843.260000, 38525.600000},
{0.000200, 0.000850, -13477.300000, 67707.600000},
............
{0.006000, 0.000650, 254881.000000, -302648.000000},
{0.006000, 0.000700, 279169.000000, -305786.000000},
{0.006000, 0.000750, 303456.000000, -308924.000000},
{0.006000, 0.000800, 327743.000000, -312062.000000},
{0.006000, 0.000850, 352031.000000, -315200.000000},
{0.006000, 0.000900, 376318.000000, -318338.000000},
{0.006000, 0.000950, 400605.000000, -321475.000000}};
float e2[][4] =
{{0.006000, 0.000000, 131091.000000, -9778.400000},
{0.006000, 0.000200, 151463.000000, -123161.000000},
{0.006000, 0.000400, 171835.000000, -236543.000000},
{0.006000, 0.000600, 230595.000000, -299510.000000},
{0.006000, 0.000800, 327745.000000, -312061.000000},
{0.006000, 0.001000, 424894.000000, -324613.000000},
{0.006000, 0.001200, 481709.000000, -194768.000000},
{0.006000, 0.001400, 538524.000000, -64922.500000},
............
{0.014000, 0.005600, 497573.000000, -0.002507},
{0.014000, 0.005800, 497629.000000, -0.002507},
{0.014000, 0.006000, 497684.000000, -0.001941},
{0.014000, 0.006200, 497719.000000, -0.001606},
{0.014000, 0.006400, 497755.000000, -0.001606},
{0.014000, 0.006600, 497779.000000, -0.899040},
{0.014000, 0.006800, 497793.000000, -2.695690},
```

```
{0.014000, 0.007000, 497807.000000, -4.491810}};
DEFINE_RW_FILE(reader, fp)
{
// reading data of electric field from available file
/*if ((fp = fopen("c:\\Deposition\\w.txt", "r"))==NULL)
{ printf("File cannot be opened");
exit(1);
}
for (j = 0; j < 620; j++)
{
for (k = 0; k < 4; k++)
{
fscanf(fp, "%f", &e1[j][k]);
}
}
fclose(fp);*/
//reading data from second file
/*fp = fopen("C:\\Deposition\\w1.txt", "r");
for (j = 0; j < 1476 ; j++)
{
for (k = 0; k < 4; k++)
{
fscanf(fp, "%f", &e2[j][k]);
}
}
fclose(fp);*/
}
DEFINE_DPM_SCALAR_UPDATE(positionxy, cell, thread, initialize, p)
{
x = p->state.pos[0] ;
```

```
y = p->state.pos[1] ;
gx = C_U(cell, thread);
gy = C_V(cell, thread);
}
DEFINE_DPM_BODY_FORCE(particle_electrical_force, p, i)
{
real bforce;
real S0, S1;
real Ex, Ey, Cc;
real tau; // relaxation time
int row, col;
//-----------------------------------
Cc = 1 + 2*lbda*(1.257 + 0.4*exp(-0.55*P_DIAM(p)/lbda))/(P_DIAM(p)) ;
//spectral intensity
S0 = 216*mu*bol*rho*P_T(p)/(pow(M_PI,2)*pow(P_DIAM(p),5)*...
pow(P_RHO(p),2)*Cc);
tau = P_RHO(p)*P_DIAM(p)*P_DIAM(p)/(18*mu) ;
//S1 = pow((M_PI*S0/tau), 0.5)*P_MASS(p);
S1 = 0;
if (x < 0.006)
{
row = floor(x/sx);
col = floor(y/sy);
Ex = (e1[row*m1+col][2] + e1[row*m1+col+1][2] + e1[row*m1+m1+col][2] +...
+e1[row*m1+m1+col+1][2])/4;
Ey = (e1[row*m1+col][3] + e1[row*m1+col+1][3] + e1[row*m1+m1+col][3] +...
+e1[row*m1+m1+col+1][3])/4;
if (i == 0)
{ // set_random_seed(rand());
bforce = 3*M_PI*mu*P_DIAM(p)*(gx - P_VEL(p)[0])/Cc + Q*Ex +...
```

```
+gauss_random()*S1; }
else
{ // set_random_seed(rand());
bforce = 3*M_PI*mu*P_DIAM(p)*(gy - P_VEL(p)[1])/Cc + Q*Ey +...
+gauss_random()*S1 ; }
}
else if (x >= 0.006)
{
row = floor((x-0.006)/sx1);
col = floor(y/sy1);
Ex = (e2[row*m2+col][2] + e2[row*m2+col+1][2] + e2[(row+1)*m2+col][2]+...
+e2[(row+1)*m2+col+1][2])/4;
Ey = (e2[row*m2+col][3] + e2[row*m2+col+1][3] + e2[(row+1)*m2+col][3]+...
+e2[(row+1)*m2+col+1][3])/4;
if (i == 0)
{
bforce = 3*M_PI*mu*P_DIAM(p)*(gx - P_VEL(p)[0])/Cc + Q*Ex +...
+gauss_random()*S1;
}
else
{
bforce = 3*M_PI*mu*P_DIAM(p)*(gy - P_VEL(p)[1])/Cc + Q*Ey +...
+gauss_random()*S1;
}
}
return (bforce/P_MASS(p));
}
DEFINE_PROFILE(inlet_x_velocity, thread, index)
{
real x[ND_ND];
```

```
real yc;
face_t f;
begin_f_loop(f, thread)
{
F_CENTROID(x, f, thread);
yc = x[1] ;
F_PROFILE(f, thread, index) = xv_init*(1-(yc*yc)/(r*r));
}
end_f_loop(f, thread);
}
```

Appendix C

Assemble drawing of the corona diffusion charger

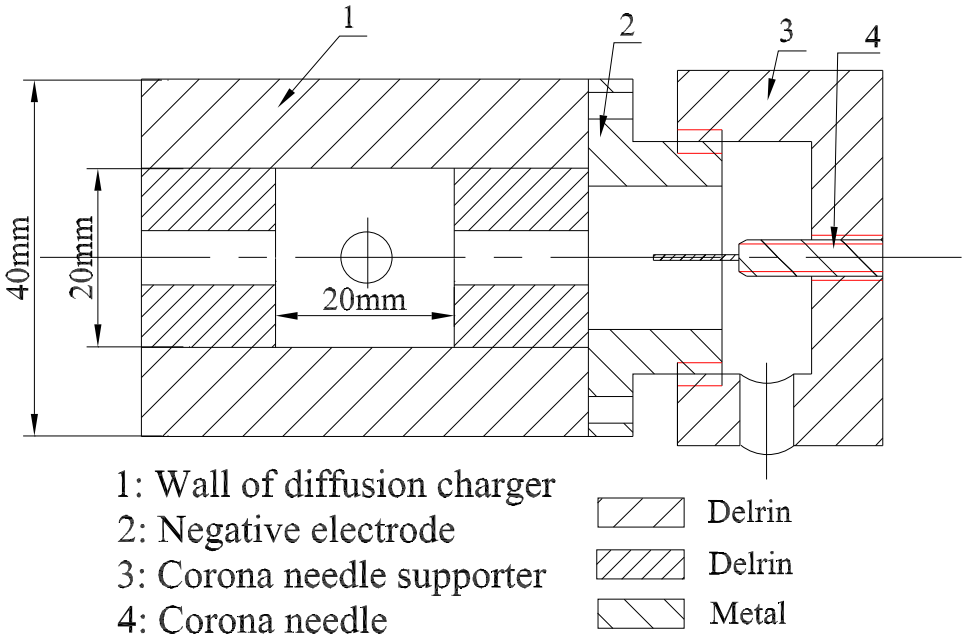

Appendix D

Assemble drawing of the electrical precipitator